Volume 96, Number 2, March–April 1991
Journal of Research of the National Institute of Standards and Technology

Contents

Articles

Conference Reports

Volume 96, Number 2, March–April 1991
Journal of Research of the National Institute of Standards and Technology

News Briefs

Volume 96, Number 2, March–April 1991
Journal of Research of the National Institute of Standards and Technology

Volume 96, Number 2, March–April 1991
Journal of Research of the National Institute of Standards and Technology

[J. Res. Natl. Inst. Stand. Technol. 96, 143 (1991)]

Linearity of a Silicon Photodiode at 30 MHz and Its Effect on Heterodyne Measurements

Volume 96 | Number 2 | March–April 1991

Alan L. Migdall and Carsten Winnewisser[1]

National Institute of Standards and Technology,
Gaithersburg, MD 20899

The effect of optical irradiance on the linearity of a Si photodiode was studied. These results are compared for light modulated at 30 MHz and at dc as the optical irradiance was varied over a 9 decade range. We discuss how these results affect the use of this detector as a heterodyne receiver. As the optical irradiance varied from 10^{-2} to 10^{+3} mW/cm^2, while maintaining constant total power, the photocurrent was constant to about 1%, but as the power density increased further, the photocurrent increased about 13%. At the highest densities that we could achieve, about 6×10^7 mW/cm^2, there was only slight evidence of the onset of saturation. These results are of importance in our work to use optical heterodyne detection to measure filter transmittances over a wide dynamic range. The results provide guidelines for achieving maximum accuracy when using this particular diode as an optical heterodyne receiver.

Key words: heterodyne; high frequency; irradiance; linearity; photodiode; saturation.

Accepted: February 11, 1991

1. Introduction

Recently [1,2] we showed how optical heterodyne detection, as proposed by Snyder [3], can be used to measure filter transmittances over a very wide dynamic range and to tie optical transmittance to rf attenuation standards in an absolute way. The accuracy of that technique depends on the linearity of the heterodyne receiver at the heterodyne frequency, 30 MHz in our case. We measured the linearity of the heterodyne receiver, a Si photodiode, used in those filter transmittance measurements as the optical power density was varied over 9 decades. These results are used to define the useful range of operating conditions of that detector for our heterodyne application. These results are compared to previous high-frequency linearity measurements of a different detector by Young and Lawton [4].

[1] Current address: University of Freiburg, Freiburg, Germany.

2. Experiment

To determine how detector responsivity varies with optical irradiance, the detector photocurrent was recorded as the detector moved through the focus of a laser beam. Since the total power on the detector was constant, any change in the photocurrent indicates a variation in detector response with optical irradiance. This method was used to measure both the 30 MHz and dc responsivities. This technique depends on good uniformity of response over the detector surface. The nonuniformity was found to be less than 1%, which was significantly smaller than the irradiance dependent variations of responsivity that were of interest.

Our source of light with a 30 MHz modulation was the output beam of the Mach-Zender interferometer used for our heterodyne measurements of filter transmittance described in reference [1]. That setup used a He-Ne laser at 632.8 nm as the light

source for the interferometer. The interferometer contained an acousto-optic modulator (AOM) in each of the two optical paths to shift the frequency of each of the light beams. The AOMs were operated with different drive frequencies to produce a 30 MHz frequency difference between the two light beams. These two beams were recombined at the output of the interferometer producing an optical beam modulated at the 30 MHz difference frequency. We used this modulated output beam as our source and focused it using a 25 mm focal length achromatic lens.

A beam profiler was used to measure the spatial profile of the output beam from which the peak power density was calculated. The beam profiler, a Photon, Inc.[2] model 1180-14, works by scanning a 50 μm slit across a Si photodiode. This device reads out the beam diameter at a selected fraction of the maximum signal level. This system works well for half maximum beam diameters of at least twice the 50 μm slit size. To determine the actual diameters of beams smaller than this, we recorded the apparent beam diameters at 25% and 75% of the peak level. The difference between these two diameters was used to determine the true 50% beam diameter. The functional dependence of the measured 25%-75% diameter difference on the actual 50% diameter was calculated in a straight-forward manner assuming a gaussian beam shape. This method is a sensitive means of determining the size of very small beams.

We verified the beam diameter measurement technique and the quality of the beam itself by determining the diameter of the beam as a function of position along the beam. The data were found to be well modeled by a gaussian beam with a 3.4 μm 50% diameter at the waist. We used the beam diameters in only one dimension, even though the beam was somewhat elliptical in cross section (about 25% difference in horizontal and vertical diameters). The error introduced into the irradiance calculations by this simplification was small compared to the 9 decade range of the measurements.

The optical heterodyne detector was a windowless EG&G FND100 PIN type Si photodiode reverse biased with 61.7 V through a 435 Ω resistor (see fig. 1). The voltage drop across the resistor of −0.2 V was always very much smaller than the drop across the diode so the diode bias remained nearly unchanged. This insured that our detection circuit did not contribute to any nonlinearity. The 30 MHz signal was ac coupled to the input of a transimpendence amplifier. The bias resistor was made as large as practically possible relative to the capacitor impedence to reduce the shunt to ground of the ac signal. The magnitude of the 30 MHz signal was measured with 0.001 dB resolution using a modified signal and attenuation calibrator [2].

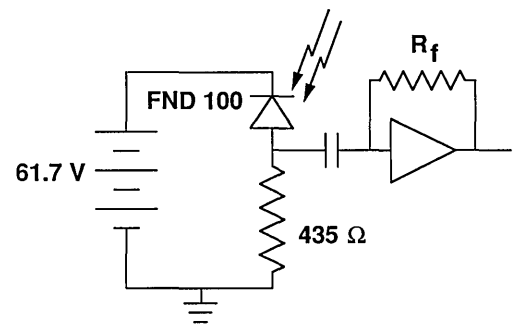

Figure 1. Detector circuit.

The dc photocurrent was determined by measuring the voltage drop across the 435 Ω resistor. To estimate the absolute internal quantum efficiency of this photodiode at dc and for low optical irradiance, we compared its response at 632.8 nm to a laser power meter that we calibrated against a 99.6 ± 0.1% efficient multi-reflection Si photodiode "trap" device [5]. Also required for this estimate was the reflectivity of the FND100, which we measured to be 16%. The internal quantum efficiency of the diode at dc was found to be 0.87 ± 0.01.

3. Results

To determine the FND100 detector response, the 30 MHz signal was recorded as the detector was moved through the focus. The single maximum in the output signal was the reference point that allowed us to match up the positions of the detector to the positions at which the beam diameter was measured. Figure 2a shows the relative response of the detector to a 30 MHz signal as a function of the optical irradiance of the peak of the spatial distribution at the detector surface. Four different data sets are shown. The points indicated

[2] Certain commercial equipment, instruments, or materials are identified in this paper to specify adequately the experimental procedure. Such identification does not imply recommendation or endorsement by the National Institute of Standards and Technology), nor does it imply that the materials or equipment identified are necessarily the best available for the purpose.

the diamonds were taken at full laser power. The other sets were taken with attenuators in the laser beam to allow the range of peak irradiances to be extended. The four data sets were shifted vertically to produce a continuous curve and the flat region of the combined curve was chosen arbitrarily as a response of 1. That flat region is where the detector response is linear. The response changed by less than 1% up to an irradiance level of 10^3 mW/cm^2. Above this level the detector exhibits an increasing responsivity, or supralinearity, of up to 12%. At the highest irradiance, above 10^6 mW/cm^2, there is some indication of the onset of saturation.

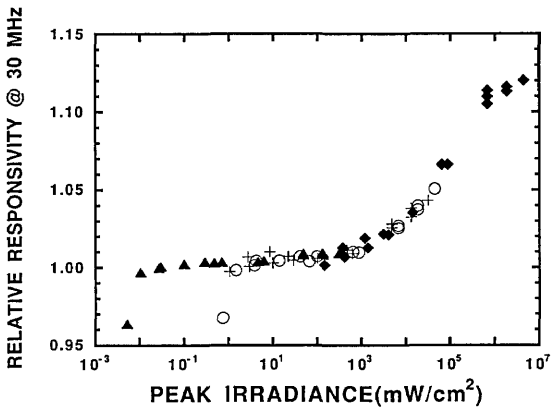

Figure 2a. Relative detector response at 30 MHz versus peak optical irradiance on the detector. The different symbols indicate data taken at different total optical powers. The different data sets were shifted to produce a continuous curve. The response in the flat region was arbitrarily chosen to be 1. The two low points were due to overfilling the detector.

For comparison purposes, we also measured the responsivity of the detector versus irradiance at dc. Figure 2b shows the relative response of the diode at dc as a function of the peak optical irradiance at the detector surface. Three different data sets are shown. The triangles and diamonds indicate distinct data sets taken at different total optical powers. The circles indicate a data set taken later to check the repeatability of the measurement. The sensitivity of our dc voltmeter did not allow us to follow the responsivity curve to irradiances as low as those reached with the 30 MHz data but we were able to take enough data to observe the linear region. As before, the response in the flat region was chosen arbitrarily to be 1. Both the dc and 30 MHz responsivities show the same irradiance threshold for the onset of nonlinearity and approximately the same rate of increase above the threshold.

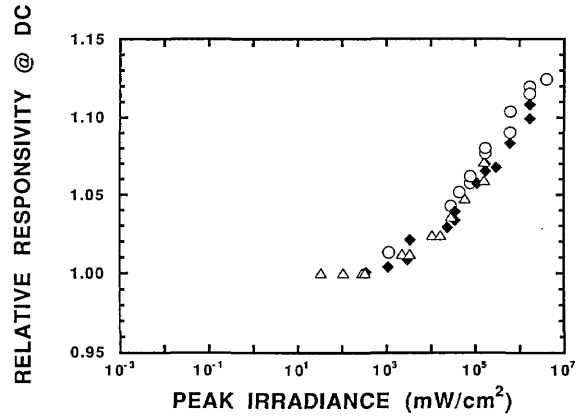

Figure 2b. Relative detector response at dc versus peak optical irradiance on the detector. The response in the flat region was arbitrarily chosen to be 1. The triangles and diamonds indicate distinct data sets taken at different total optical powers. The circles indicate a data set taken at a later time to check the repeatability.

Since no internal gain is expected, the largest the internal quantum efficiency of our photodiode can be is 1. As a result the low-irradiance dc quantum efficiency of 0.87 can rise by at most 15%. The total measured increase of the dc responsivity is 12.5%, nearly the same as for the 30 MHz data. This level of increase is nearly equal to the maximum allowable increase.

4. Conclusions

For the FND 100 diode used in our heterodyne measurements, the dependences of the 30 MHz and dc responsivities on irradiance were nearly the same. The detector was linear at irradiance levels below 10^3 mW/cm^2. At irradiance levels above 10^3 mW/cm^2 the response increased by up to 13%. This brought the internal quantum efficiency to nearly 100% as determined by the absolute measurement of the low-irradiance internal dc quantum efficiency.

This level of increase in responsivity can be explained by the saturation of loss mechanisms such as recombination at trap sites [6]. Impurities within the diode act as trap sites where photogenerated charge carriers can be caught long enough to recombine. This reduces the quantum efficiency to

less than 1. As the optical irradiance and thus the carrier concentration increases, the trap sites fill up. This reduced loss has the effect of increasing the quantum efficiency up toward a maximum level of 1, although other saturation mechanisms may become important before that limit is reached. The quantum efficiency increased nearly to 1 with only a hint of responsivity saturation at the highest irradiances that we could achieve.

The results here are in contrast to the work of Young et al. that compared the dc and 600 MHz responsivities of a HP 5082-4220 PIN type diode. They saw no evidence of supralinearity in either the dc or high-frequency responsivities. They also found differences between the two responsivities that our FND 100 diode did not exhibit.

As a result of these measurements, we have found that our detector/amplifier package can be used to make linear measurements of an optical heterodyne signal as long as the irradiance is less than 10^3 mW/cm^2. Even at irradiances larger than this, the optical heterodyne measurements can still be made linear, as long as the local oscillator beam remains constant and is significantly more powerful than the signal beam. If this is the case, the responsivity remains nearly constant, because as the signal beam irradiance changes, the total irradiance does not vary much. With these easy to achieve conditions, our heterodyne receiver is linear and can be used in high-accuracy applications.

5. References

[1] Migdall, A. L., Roop B., Zheng, Y. C., Hardis, J. E. and Gu Jun xia, Appl. Opt. **29**, 5136 (1990).
[2] Migdall, A. L., Roop, B. and Gu Jun xia, Measuring Filter Transmittance Using Heterodyne Detection, submitted to Metrologia.
[3] Snyder, J. J., Appl. Opt. **27**, 4465 (1988).
[4] Young, M. and Lawton, R. A., Appl. Opt. **17**, 1103 (1978).
[5] Cromer, C., A new spectral response calibration method using a silicon photodiade trap detector, to be published in Proc. Measurement Science Conf., Jan. 31, 1991. Devices similar to the one used here are described in two papers in SPIE Vol. 1109, Optical Radiation Measurements II, Palmer, James M. Ed., 27–28 March 1989—Houston, J. M. and Zalewski, E. F., Photodetector Spectral Response Based on 100% Quantum Efficient Detectors, pp. 268–277 and Fox, N. P. and Martin, J. E., A Further Intercomparison of Two Cryogenic Radiometers, pp. 227–235.
[6] Schaefer, A. R., Zalewski, E. F., and Geist, J., Appl. Opt. **22**, 1232 (1983).

About the authors: Alan L. Migdall is a physicist in the Radiometric Physics Division of the NIST Physics Laboratory. Carsten Winnewisser is a student at the University of Freiburg, Freiburg, Germany and was a Guest Researcher at NIST.

Volume 96, Number 2, March–April 1991
Journal of Research of the National Institute of Standards and Technology

[J. Res. Natl. Inst. Stand. Technol. 96, 147 (1991)]

Use of the Electrostatic Classification Method to Size 0.1 μm SRM Particles—A Feasibility Study

Volume 96 Number 2 March–April 1991

Patrick D. Kinney and David Y. H. Pui

University of Minnesota, Minneapolis, MN 55455

and

George W. Mulholland and Nelson P. Bryner

National Institute of Standards and Technology, Gaithersburg, MD 20899

The use of the electrostatic classification method for sizing monodisperse 0.1 μm polystyrene latex (PSL) spheres has been investigated experimentally. The objective was to determine the feasibility of using electrostatic classification as a standard method of particle sizing in the development of a 0.1 μm particle diameter Standard Reference Material (SRM). The mean particle diameter was calculated from a measurement of the mean electrical mobility of the PSL spheres as an aerosol using an electrostatic classifier. The performance of the classifier was investigated by measuring its transfer function, conducting a sensitivity analysis to verify the governing theoretical relationships, measuring the repeatability of particle sizing, and sizing NIST SRM 1691, 0.269 μm and NIST SRM 1690, 0.895 μm particles. Investigations of the aerosol generator's performance focused on the effect of impurities in the particle-suspending liquid on the resulting particle diameter.

The uncertainty in particle diameter determined by electrical mobility measurements is found to be −3.3% to +3.0%. The major sources of uncertainty include the flow measurement, the slip correction, and a dependence of particle size on the aerosol flow rate. It was found that the classifier could be calibrated to indicate the correct size to within 0.1% for both SRM particle sizes if the defined classification length is decreased by 1.9%.

Key words: aerosol generator; atomizers; condensation nuclei counters; electrical mobility; particle size; polystyrene latex spheres.

Accepted: November 20, 1990

1. Introduction

This study assesses the accuracy of electrostatic classification for measuring the diameter of 0.1 μm polystyrene latex (PSL) spheres produced as an aerosol by atomizing a suspension of PSL spheres in water. The PSL spheres used in this study were produced by emulsion polymerization by Dow Chemical Company[1] and the nominal size as measured at Dow by transmission electron microscopy is 0.109 μm. This study is motivated by the need to develop an accurate 0.1 μm particle size standard. This size standard is important for improving particle sizing accuracy by electron microscopy, light scattering, and by other methods. A particle diameter of 0.1 μm is in the size range of combustion generated particles, contamination particles of concern in the semiconductor industry, air pollutant particulates, viruses, and various manufactured particulates such as carbon black and fumed silica.

The electrostatic classifier is a widely used instrument in aerosol research for both particle sizing and

[1] Certain commercial equipment, instruments, or materials are identified in this paper to specify adequately the experimental procedure. Such identification does not imply recommendation or endorsement by the National Institute of Standards and Technology, nor does it imply that the materials or equipment identified are necessarily the best available for the purpose.

for generation of monodisperse aerosols over the size range 0.005 to 1.0 μm. The basic physical principle of the classifier is that the velocity of a charged spherical particle in an electric field is directly related to the diameter of the particle. A charged aerosol enters near the outer circumference of the classifier and particles with a narrow range in electrical mobility exit through a slit in the center electrode. The mobility distribution is determined by measuring the number concentration exiting the slit as a function of the electrode voltage.

The theory of the classifier operation and its performance have been extensively studied [1-7]. In regard to sizing PSL spheres with the classifier, Kousaka et al. [8], compared measurements of PSL spheres made with the electrostatic classifier to measurements made with a sedimentation method, and a balance method using a Millikan type cell. The three measurements were found to agree within a few percent for 0.2 to 1 μm particles, but measurements were not conducted for particles smaller than 0.2 μm in diameter.

The determination of the accuracy of a measurement method requires that all the physical variables entering into the particle size equation be accurately known. The two key physical variables for the electrostatic classifier are the volumetric flow rate and the electrode voltage. The procedure used at NIST for these two calibrations is described in section 3.2.1. An important element in assessing the accuracy of an instrument is the verification that the instrument behaves according to the governing equation. The verification procedure outlined in section 3.2.3 included comparison with the theory [1] and the use of two classifiers in tandem [9]. Further verification of the classifier performance is contained in section 3.2.4, where the measured and predicted sensitivity of the classifier peak voltage to a change in the flow volume and the operating pressure are compared. Another way the accuracy of the classifier was established was by measuring two primary calibration standards for particle size: 0.269 μm (NIST SRM 1691) and 0.895 μm (NIST SRM 1690). The results of this comparison are contained in section 3.2.6.

The method for generating the PSL sphere aerosol involved atomizing a suspension of PSL spheres dispersed in water. The non-volatile impurities in PSL sphere suspension result in a residue thickness on the PSL sphere. Significant effort was involved in minimizing the droplet size produced by the atomizer system, section 3.3.1, and in quantifying the amount of impurity in the dilution water, section 3.3.2, and in the original, undiluted suspension, section 3.3.3.

In section 4, the Discussion section, a comparison is made between the results of this study and two other studies [10,11] that focused on the accurate measurement of the same batch of Dow 0.109 μm PSL spheres.

2. Experimental Apparatus

Figure 1 shows a schematic diagram of the instrumentation used in this study. The major components are the atomizer, the electrostatic classifier, and the condensation nucleus counter. A PSL aerosol is produced by atomizing a suspension of PSL spheres in water. After conditioning, the particles are passed through the electrostatic classifier. By monitoring the number concentration with the nucleus counter versus the mobility setting of the classifier, the mean electrical mobility of the particles is determined. The mean size is then determined from the particle size dependence of the electrical mobility. A more detailed description of each instrument follows.

2.1 Aerosol Generation

The PSL spheres are aerosolized with an atomizer, shown in figure 2, consisting of a 15 psig air jet impinging on the end of a liquid feed tube. The opposite end of the feed tube is submerged in a suspension of PSL spheres in water. The vacuum produced by the air jet draws the particle suspension through the capillary tube and into the air jet. The jet atomizes the PSL particle suspension producing an aerosol of droplets. Some of the droplets produced contain PSL spheres while other droplets are "empty." The droplets evaporate as they flow through a diffusion drier and are diluted with clean, dry air. Droplets containing PSL spheres evaporate to form a PSL sphere with a slight surface residue. Droplets which do not contain a PSL sphere evaporate and form a small residue particle consisting of nonvolatile impurities present in the original particle suspension liquid. Thus, the resulting aerosol consists of potentially dirty PSL spheres and small impurity particles.

When a droplet containing a PSL sphere evaporates, any non-volatile impurities in the liquid remain to form a thin layer of residue on the particle surface. The residue formed on the surface has a finite thickness and produces a systematic error in the measurement of particle diameter. To reduce the concentration of impurities in the particle suspension, de-ionized/filtered water was used to

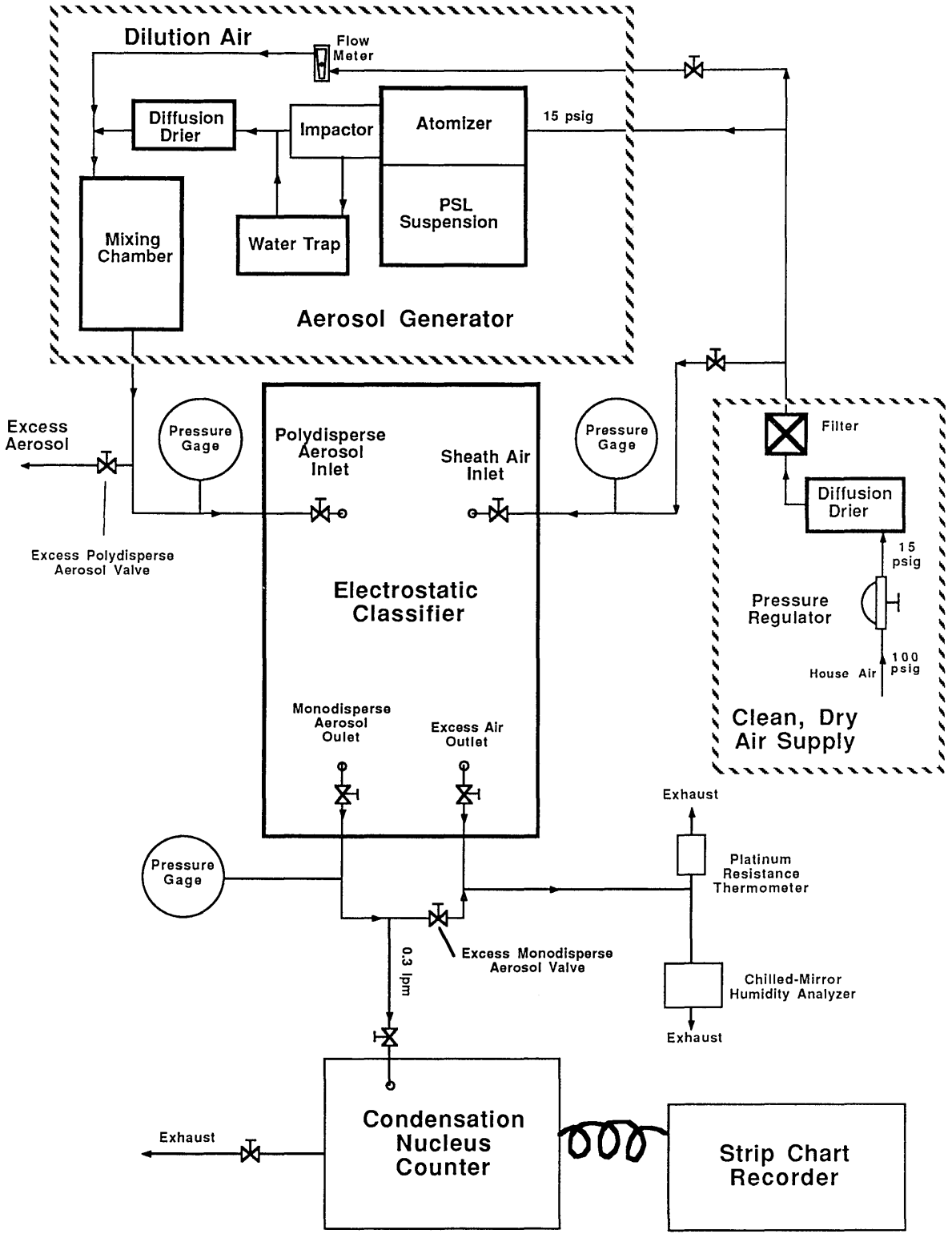

Figure 1. Apparatus for particle sizing with the electrostatic classifier.

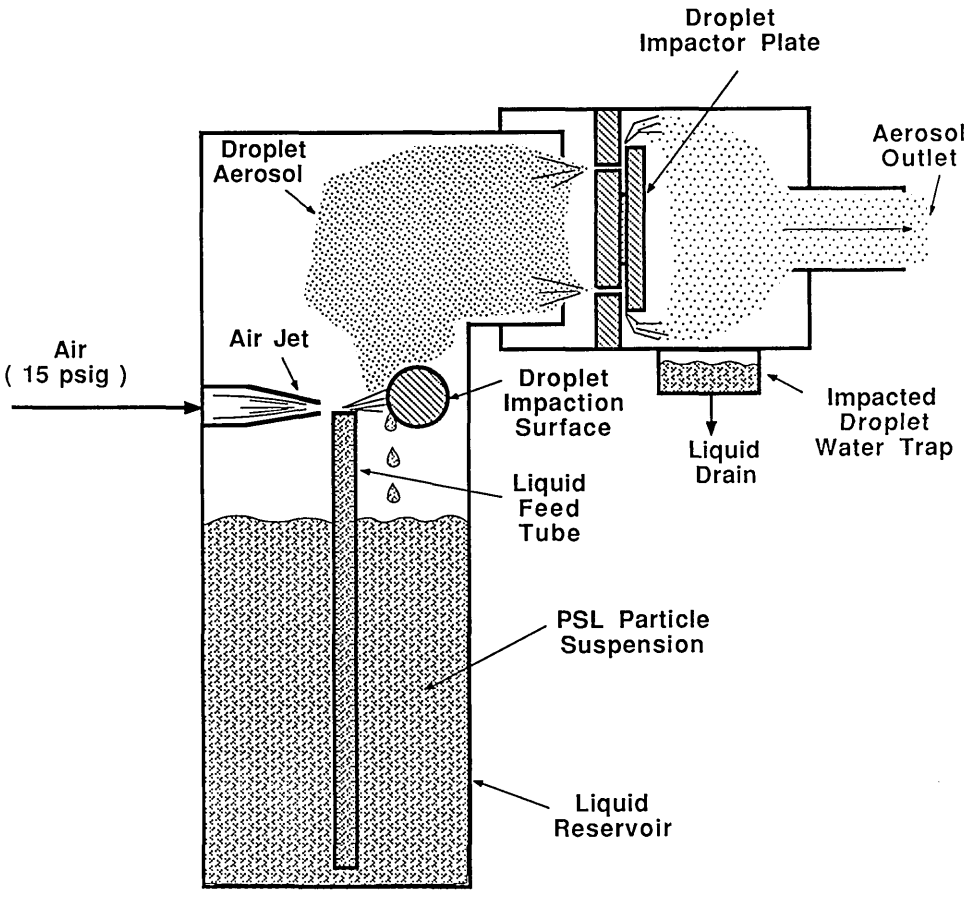

Figure 2. Atomizer with droplet impactor.

suspend the PSL spheres. The larger droplets evaporate leaving a larger impurity residue on the particle surface. To minimize this effect, an impactor with a cut point of about 0.5 μm was placed at the outlet of the atomizer. The effect of impurity concentration on the size of 0.1 μm PSL spheres has been experimentally investigated in this study.

2.2 The Electrostatic Classifier

The electrostatic classifier used in this project is a commercially available instrument (TSI, Inc., Model 3071). Figure 3 shows a schematic diagram of the instrument. The classifying region is bounded by a stainless steel outer cylinder with an inner diameter of 3.916 cm, and a coaxial, stainless steel center rod with an diameter of 1.874 cm. The center rod is connected to a variable (0 to −11,000 V) negative dc power supply, and the outer cylinder is grounded. By varying the center rod voltage, the electric field in the annular region can be varied from 0 to about 11,000 V/cm.

Clean sheath air, after passing through a fine-mesh flow straightening screen at the top of the classifier, flows axially through the annular region along the center rod. A smaller, polydisperse aerosol flow enters through an axisymmetric opening along the outer cylinder. The clean air flow forces the aerosol to flow downward in a thin layer on the outer wall of the classifying region. It is essential that these two streams merge smoothly without mixing. Near the bottom of the classifying region, a slit on the center rod extracts a fraction of the air flow consisting of near-monodisperse (single sized) aerosol particles. The remainder of the air flow exits through the end of the annular region as excess air. The length of the classifying region (44.44 cm) is defined as the axial distance from the aerosol entrance to the aerosol exit at the slit in the center rod.

Before entering the classifying region, the particles are sent through a charge neutralizer. The neutralization occurs through interaction with bi-polar gaseous ions (positive and negative ions)

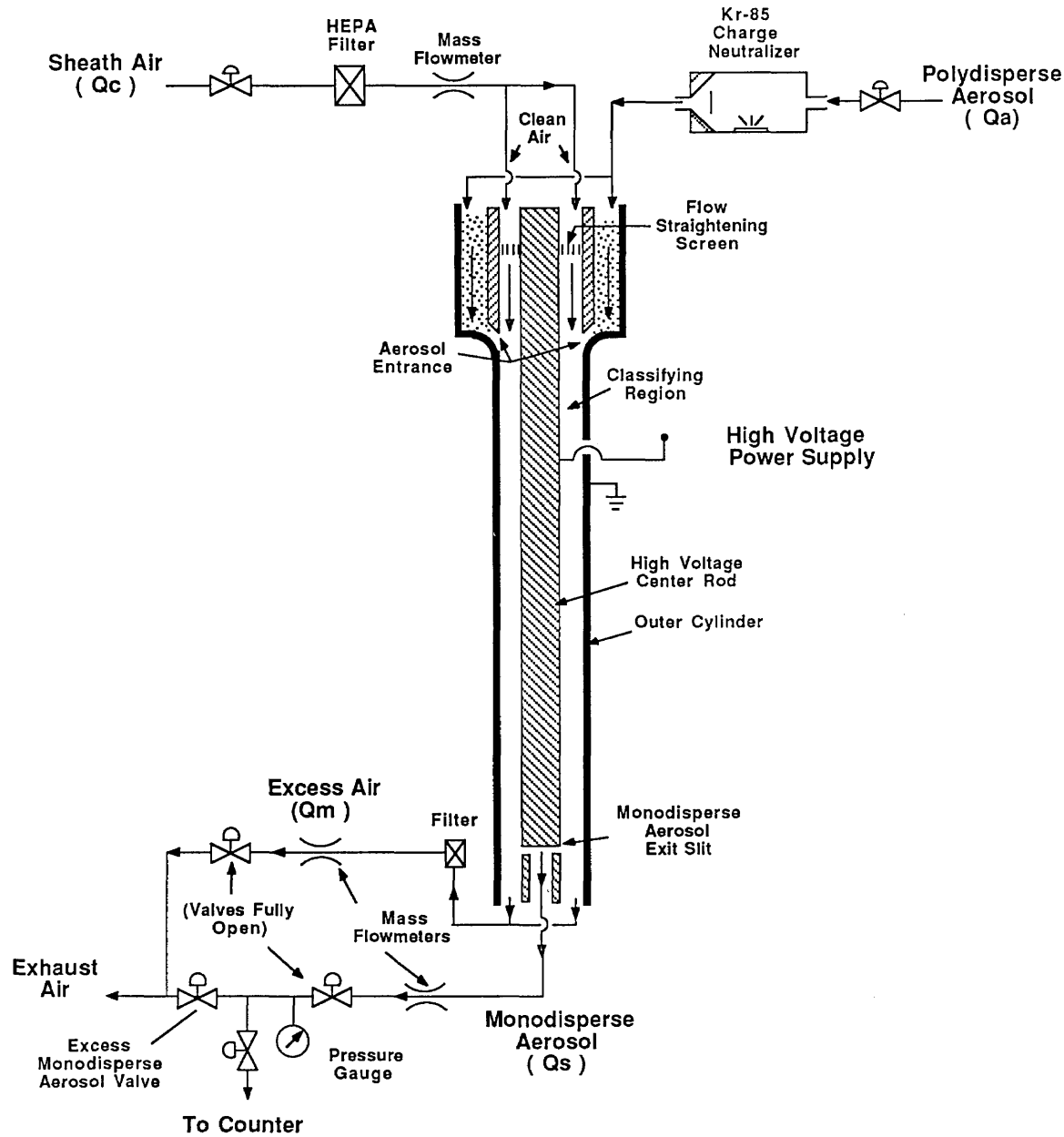

Figure 3. Electrostatic classifier.

produced by radioactive Kr-85. The ions impart a bi-polar charge distribution on the aerosol particles. For particles with diameters around 0.1 μm, about 24% of the particles carry a single positive elementary charge and about 4% carry a double positive charge [12].

When the particles enter the classifying region, they are carried axially down the classifying region with the sheath air flow, and the particles carrying a positive charge move radially towards the center rod under the influence of the electric field. Negatively charged particles deposit on the inner surface of the outer cylinder. Within the classifying region, a particle rapidly reaches a steady radial velocity through equilibrium between the electric field force, and the opposing Stokes drag force. The radial velocity of the particle in the electric field is determined by the particle's electrical mobility, defined as the velocity a particle attains under the influence of a unit electric field.

The electrical mobility, Z_p, of a singly-charged particle can be derived by equating the electric field force, F_ϵ, with the Stokes drag force, F_d:

Stokes Drag Force: $$F_d = \frac{3\pi \mu V D_p}{C(D_p)}$$

Electric Field Force: $$F_\epsilon = \epsilon E$$

Electrical Mobility: $$Z_p = \frac{V}{E} = \frac{\epsilon C(D_p)}{3\pi \mu D_p} \quad (1)$$

Where

V = radial component of particle velocity
E = electric field strength
ϵ = elementary unit of charge
$C(D_p)$ = slip correction
μ = air viscosity
D_p = particle diameter.

As seen from eq (1), small particles have high electrical mobilities, and thus move with high radial velocities toward the center rod and deposit on its surface. Larger particles, with lower electric mobilities, are swept further down the classifying region before depositing on the center rod. Still larger particles are swept out the bottom of the classifier with the excess air. The monodisperse output of the classifier is extracted through a small slit on the center rod shown in figure 3. Only particles with electric mobilities within a narrow range have trajectories which bring them to the entrance of the slit. Particles reaching the entrance of the slit are removed from the classifying region by the air flow entering the slit. In this way the classifier extracts a narrow size range of particles from the broader size range of particles entering the classifying region.

2.2.1 The Transfer Function Knutson and Whitby [1] developed a theory for the classifier based on integrating the particle trajectory equations. The major result of their theory is an equation for the transfer function, Ω, which is defined as the probability an aerosol particle that enters the analyzer will leave via the sampling flow given that the particle has a mobility Z_p. A brief summary of their analysis is presented below.

Let r and z denote the radial and axial coordinates, respectively, within the mobility analyzer with z increasing in the direction of the main airflow. Let $u_r(r,z)$ and $u_z(r,z)$ be the radial and axial components of the airflow velocity. Similarly, let $E_r(r,z)$ and $E_z(r,z)$ be the components of the electric field. Neglecting particle inertia and Brownian motion, one obtains the following two first order differential equations for the particle path:

$$dr/dt = u_r + Z_p E_r, \quad (2)$$

$$dz/dt = u_z + Z_p E_z. \quad (3)$$

To demonstrate the conjugate nature of the flow field and the electric field, Knutson and Whitby transformed to new coordinates, ψ, the stream function, and ϕ, the electric flux function.

$$\psi(r,z) = \int^{r,z} [ru_r dz - ru_z dr], \quad (4)$$

$$\phi(r,z) = \int^{r,z} [rE_r dz - rE_z dr]. \quad (5)$$

They then demonstrate that the total differential of $\psi + Z_p\phi$ is zero leading to the following significant result:

$$\psi = -Z_p\phi + \text{constant}. \quad (6)$$

Quoting Knutson and Whitby [1] "The particle moves in such a way that the ratio of the number of streamlines crossed to the number of electric field lines crossed is always equal to the particle electric mobility, Z_p."

The advantage of this method of analysis is that the stream function is closely related to the volumetric flow rate, which is an experimentally controlled variable. Representative streamlines are indicated in figure 4 and the corresponding flow variable is indicated below:

$2\pi(\psi_2 - \psi_1)$ = aerosol inlet volume flow rate, Q_a
$2\pi(\psi_4 - \psi_2)$ = inlet sheath air volume flow rate, Q_c
$2\pi(\psi_4 - \psi_3)$ = monodisperse aerosol volumetric flow rate, Q_s
$2\pi(\psi_3 - \psi_1)$ = outlet excess air volume flow rate, Q_m.

With the initial condition $\psi = \psi_{in}$ at $\phi = \phi_{in}$, eq (6) for the particle path becomes:

$$\psi = \psi_{in} - Z_p(\phi - \phi_{in}). \quad (7)$$

At $\phi = \phi_{out}$, ψ has the value ψ^*, given by:

$$\psi^* = \psi_{in} - Z_p\Delta\phi, \quad (8)$$

where $\Delta\phi = \phi_{out} - \phi_{in}$. The electric field is vanishingly small in the aerosol entrance and at the exit slip so that ϕ is a constant ϕ_{in} throughout the entrance and ϕ_{out} throughout the exit slit.

The transfer function, Ω, is the probability that the particle will leave via the sampling slit, which can happen only if

$$\psi_3 < \psi^* < \psi_4. \tag{9}$$

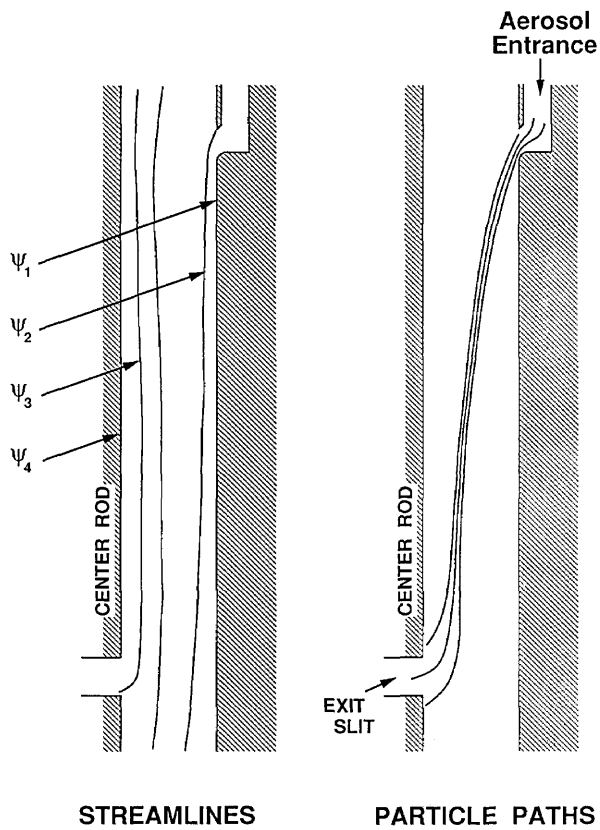

Figure 4. Schematic representation of mobility analyzer streamlines and particle paths.

The probability, Ω, is therefore equal to the fraction of the interval $(\psi_1 - Z_p\Delta\phi,\ \psi_2 - Z_p\Delta\phi)$ which is intercepted by the interval (ψ_3, ψ_4). The results of carrying out such an analysis, which is tedious but straightforward, are presented in figure 5.

There are several important features of the transfer function apparent from figure 5. If the aerosol inlet flow and the monodisperse sampling flow are equal, $Q_a = Q_s$, the transfer function has a triangular shape with a sharp peak corresponding to a probability Ω of 1. This is the best condition for obtaining accurate particle size.

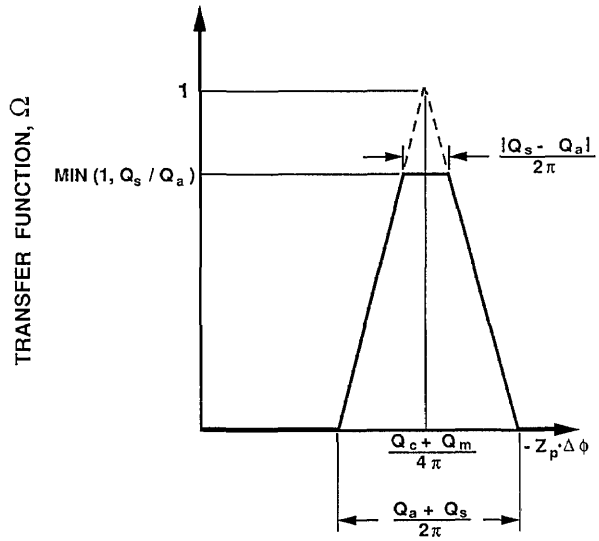

Figure 5. The mobility analyzer transfer function. The dashed curve corresponds to $Q_s = Q_a$.

For unequal flow rate, the transfer function has a trapezoidal shape. The origin of the top of the trapezoid can be understood intuitively from the following example. Suppose the inlet aerosol flow is less than the monodisperse sampling flow. Then there will be a range of voltages for the center rod for which all the inlet aerosol with mobility Z_p will be sampled by the monodisperse outlet. This implies that the transfer function is unity for a range of voltages thus leading to a flat top rather than a triangular shaped peak.

The actual measurements of mobility are made versus the voltage setting of the center rod. The relationship between $\Delta\phi$ and the voltage V can be obtained using eq (5) and the expression for the radial and axial components of the electric field:

$$E_z = 0,\ E_r = V/[r\ln(r_2/r_1)]. \tag{10}$$

Performing the integration yield the following result:

$$\Delta\phi = VL/\ln(r_2/r_1). \tag{11}$$

The three features of figure 5 of greatest importance to the measurement of particle size are the centroid of the transfer function, and the upper and lower widths of the transfer function. Expressing the results in terms of the mobility, Z_p, Knutson and Whitby [1] obtained the following expression for the centroid of the mobility band.

$$Z_p = \frac{Q_c + Q_m}{4\pi VL} \ln(r_2/r_1). \tag{12}$$

The range of the electrical mobility, ΔZ_p, of particles exiting through the slit is given as:

$$\Delta Z_p = \frac{(Q_a + Q_s)}{2\pi VL} \ln(r_2/r_1) . \quad (13)$$

The range in ΔZ_p corresponding to the upper portion of the trapezoid in figure 5, which we denote as ΔZ_p^* is given by

$$\Delta Z_p^* = \frac{|Q_s + Q_a|}{2\pi VL} \ln(r_2/r_1) . \quad (14)$$

where

Z_p = particle electrical mobility
ΔZ_p = electrical mobility width at base
ΔZ_p^* = electrical mobility width of plateau region
V = voltage on the center rod
L = length from aerosol inlet to exit slit
r_2 = radius of the outer cylinder (inside surface)
r_1 = radius of the center rod.

Several assumptions were made in the development of these equations. The flow field is assumed to be laminar, axisymmetric, and incompressible; the electric field is assumed uniform, neglecting field distortions at the aerosol entrance and the sampling exit slit; particle inertia and Brownian motion are neglected; and the influence of space and image charges are assumed negligible.

2.2.2 Measurement of the Electrical Mobility Distribution By varying the voltage on the inner rod of the classifier, and measuring the concentration of the aerosol exiting through the monodisperse aerosol outlet, the distribution of the inlet aerosol's electrical mobility can be measured. The resolution of this measurement can be controlled, as seen in eqs (12) and (13), by decreasing the ratio of aerosol flow rate to sheath flow rate. Using eq (1), the electrical mobility distribution can be converted to the size distribution of the inlet aerosol.

The classifier is instrumented with an adjustable voltage power supply and three mass flowmeters which control the sheath air, excess air, and monodisperse aerosol flow rates. The flowmeters operate by measuring the current needed to maintain a constant-temperature hot-wire element in the air flow and are sensitive to the mass of air passing the sensing element.

The calibration of a mass-sensing flowmeter can take the form of either an actual mass flow rate curve ([grams of air]/second vs meter voltage) or a volumetric flow rate curve ([liters of air]/second at T,P vs meter voltage) where T and P are the air temperature and pressure during calibration. As seen in eqs (12) and (13), measurements made with the classifier depend on volumetric flow rates. Since the classifier measures the flow rates using mass-sensing flowmeters, a correction must be made if the temperature and pressure of the air in the classifier differ from the temperature and pressure of the air used for the flowmeter calibration.

If the flowmeters are calibrated using dry air, the correction to the calibration for dry air can be obtained from the ideal gas equation, and is as follows:

$$Q_{vol} = Q_{cal} \cdot \frac{T_{actual}}{T_{cal}} \cdot \frac{P_{cal}}{P_{actual}} \quad (15)$$

where

Q_{vol} = volumetric flow rate
Q_{cal} = calibrated volumetric flow rate at T_{cal},P_{cal}
T_{cal} = calibration temperature
P_{cal} = calibration pressure
T_{actual} = actual temperature inside classifier
P_{actual} = actual pressure inside classifier.

The correction to the flowmeter calibration for wet air is slightly different, and is described in section 3.2.2.

During operation of the classifier, the pressure, temperature and relative humidity of the air inside the classifier were measured, and the volumetric flow rate was calculated using eq (15). The temperature and relative humidity of the air inside the classifier were found by measuring the conditions of the air passing through the excess air line. The temperature was measured using a platinum resistance thermometer, and the relative humidity was measured using a chilled-mirror humidity analyzer.

The pressure inside the classifier was about 3.5×10^3 Pa (36 cm H_2O) above ambient for 333 cm^3/s (20 L/min) sheath air flow. To minimize the gage pressure in the classifier, the excess air and monodisperse aerosol valves were left fully open, and flows were adjusted with the excess monodisperse aerosol valve (see fig. 3). The elevated pressure inside the classifier is required to exhaust the sheath flow through the flow straightening header at the bottom of the classifying region. The pressure inside the classifier is monitored by measuring the pressure in the monodisperse aerosol outlet line, and applying a slight correction, 150 Pa (1.5 cm H_2O) for a 33.3 cm^3/s (2 L/min) aerosol flow, to account for the pressure drop from the interior of the classifier to the pressure tap on the monodisperse outlet.

2.3 The Condensation Nucleus Counter

Figure 6 shows a schematic diagram of the condensation nucleus counter (CNC) (TSI, Inc., Model 3020). The instrument samples aerosol at a flow rate of 5 cm^3/s and indicates the number concentration of the aerosol. The counting efficiency is nearly 100% for particles from about 0.02 to at least 0.1 μm [13].

The aerosol entering the counter passes through a chamber containing nearly saturated butyl alcohol vapor. The aerosol-alcohol vapor mixture is then passed through a cooled condensing tube causing the alcohol vapor to condense onto the particles. The condensing alcohol causes the particles to grow to a size easily detected with an optical counter at the exit of the condensing tube. In the optical particle counter, the particles pass through a focused light beam and scatter light onto a photodetector. In the single particle counting mode, used for lower particle concentrations, counting of individual pulses from the photodetector provides particle concentration. In the concentration mode, used for high particle concentrations, the analog level of the photodetector is calibrated to provide particle concentration. In general, since the single particle counting mode does not require calibration, its concentration measurements are

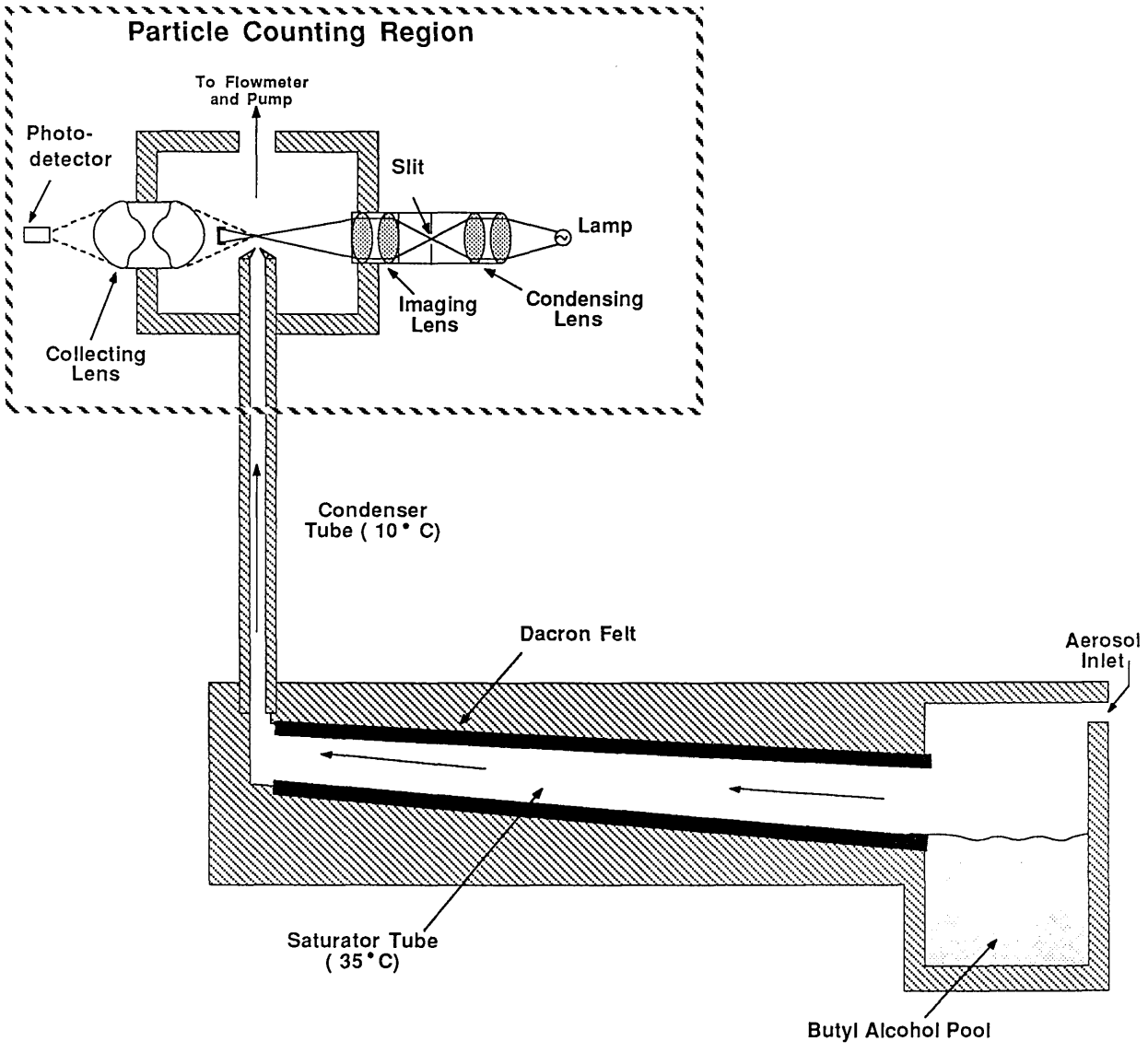

Figure 6. Condensation nucleus counter.

considered more accurate. For sizing PSL spheres, the concentration was kept low enough to use the single particle counting mode. The PSL particle concentrations downstream of the classifier were maintained by adjusting the concentration of the PSL suspension used in the atomizer.

3. Experimental Methods and Results

Following a general description of PSL particle sizing with the classifier, the measurement methods for defining the accuracy of particle size measurements by the electrical mobility classifier are presented. This section includes a detailed uncertainty analysis of the classifier performance and an analysis of the effect of non-volatile impurities on the PSL sphere size as an aerosol.

3.1 Procedure for Sizing Particles with the Electrostatic Classifier

Sizing the PSL spheres with the electrostatic classifier is a relatively fast process. A suspension of particles is prepared, the PSL-particle aerosol is generated, the classifier is used to measure the voltage corresponding to the mean electrical mobility of the PSL spheres, and a straight forward data reduction process provides a measurement of the mean particle diameter. From start to finish, the sizing process takes about 15 min. The liquid suspension of PSL spheres was prepared by diluting a concentrated suspension with deionized-filtered water. The concentrated suspension of the 0.1 μm PSL spheres consisted of about 10% by weight PSL spheres suspended in water. The Standard Reference Material particles, 0.3 and 0.9 μm, were supplied in a suspension of 0.5% by weight PSL spheres in water. The nominal dilutions and particle concentrations of the PSL suspensions used in the atomizer are as follows:

Particle diameter	Drops of concentrated PSL suspension	dilution volume	concentration #/ml
0.1 μm	3 of 10% by weight	250 ml	6×10^{10}
0.3 μm	3 of 0.5% by weight	25 ml	2×10^{9}
0.9 μm	10 of 0.5% by weight	25 ml	2×10^{8}

While the 0.3 μm and 0.9 μm particle concentrations in the liquid suspension were lower than the 0.1 μm particle concentration, the monodisperse aerosol concentrations were similar. The lower liquid concentrations of the 0.3 μm and 0.9 μm particles is offset by atomizing the suspensions without the impactor. The atomizer produces more particle-carrying droplets without the impactor.

Following a warm-up period to allow the classifier flowmeters to stabilize, the aerosol was generated and passed through the classifier. During normal operation, the sheath and excess air flow rates were kept equal, resulting in equal polydisperse and monodisperse aerosol flow rates. To minimize the internal pressure of the classifier, the excess air and monodisperse aerosol valves were operated in a fully open position. The sheath air flow rate was set by iterating with the two valves upstream of the sheath air inlet, shown in figure 1, until the pressure between the valves was about 1.60×10^{4} Pa (160 cm water) while maintaining the desired flow rate. The pressure upstream of the sheath air inlet was maintained at 1.60×10^{4} Pa to match the conditions existing during flowmeter calibration. The excess polydisperse aerosol valve and the excess monodisperse aerosol valve were iteratively adjusted to provide the correct excess air and monodisperse aerosol flow rates. The flow rates used for sizing the 0.1 μm particles were nominally 333 cm^3/s (20 L/min) sheath air flows, and 33.3 cm^3/s (2 L/min) aerosol flows. For sizing the 0.3 μm particles, the flow rates were nominally 167 cm^3/s (10 L/min) sheath flows, and 16.7 cm^3/s (1 L/min) aerosol flows. The 0.9 μm particles were sized using nominally 50 cm^3/s (3 L/min) sheath, and 5 cm^3/s (0.3 L/min) aerosol flow rates. Other flow rates were used to investigate the effect of flow rate on size measurements.

Once the flow rates in the classifier were established, the center rod voltage was varied to find the peak in the mobility distribution as measured by the condensation nucleus counter. The concentration was then monitored for several minutes to insure a constant aerosol concentration. The fluctuations in the particle concentration were consistent with a Poisson distribution of number concentration; that is, the coefficient of variation, CV, defined as the ratio of the standard deviation in the number concentration to the average number concentration, was in agreement with the predicted CV for a Poisson distribution.

$$CV = \frac{1}{\sqrt{N}}$$

where

CV = coefficient of variation for a Poisson distribution
N = average aerosol number concentration.

The concentration recorded for a given voltage setting was obtained by monitoring several consecutive concentration readings (one reading every 3 s) and then estimating the average concentration. When the concentration fluctuations were obviously larger than statistically predicted, the measurement was discarded and efforts were made to stabilize the concentration. Gradual concentration changes over the course of measuring the mobility distribution resulted in slight sizing uncertainties and are included in the estimate of particle diameter measurement uncertainty.

After the aerosol concentration stabilized, the voltage on the center rod of the classifier was adjusted symmetrically about the peak concentration voltage. The concentration was recorded for each voltage setting. A typical concentration-voltage curve is shown in figure 7. The quantity of primary interest in this study is the peak voltage which is the voltage corresponding to the peak in the concentration-voltage curve. The peak voltage is computed as the concentration weighted average as follows:

$$V_{ave} = \frac{\Sigma V_i N_i}{\Sigma N_i} \tag{16}$$

where

V_{ave} = peak voltage
V_i = measurement voltages
N_i = concentration corresponding to V_i.

Once the representative voltage of the peak is found, the particle diameter can be calculated using eqs (1) and (12). Since the particle slip correction is dependent on particle diameter, it is necessary to iterate with eq (12) to determine the diameter. A simple iteration routine is used for this purpose.

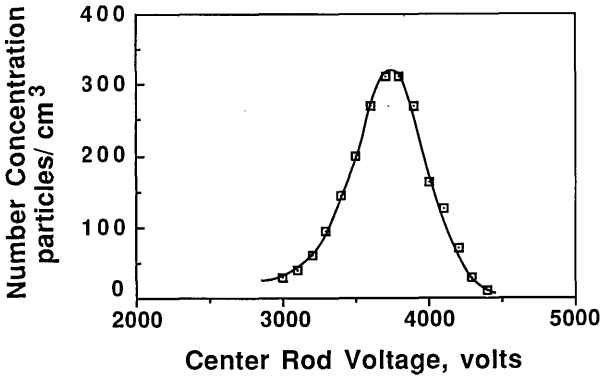

Figure 7. Number concentration vs center rod voltage for 0.1 μm PSL spheres.

The calculation of particle diameter from eqs (1) and (12), requires accurate values for the viscosity of air, μ, and the particle slip correction, C. The slip correction used in the diameter calculations is based on Allen and Raabe's [14] measurements for PSL spheres using an improved Millikan apparatus:

$$C = 1 + Kn\left[1.142 + 0.558\exp\left(\frac{-0.999}{Kn}\right)\right] \tag{17}$$

where

C = particle slip correction
Kn = Knudsen number

$Kn = \frac{2\lambda}{D_p}$, where D_p is the particle diameter
λ = mean free path of air.

Pressure and temperature corrections were made to the mean free path (λ) [15]:

$$\lambda = \lambda_0\left(\frac{T}{T_0}\right)\left(\frac{P_0}{P}\right)\left(\frac{1+\frac{110.4}{T_0}}{1+\frac{110.4}{T}}\right) \tag{18}$$

where

λ_0 = 0.0673 μm, for air at T_0, P_0
T_0 = reference temperature, 296.15 K
P_0 = reference pressure, 1.01×10^5 Pa (760 mm Hg)
T = air temperature, Kelvin
P = air pressure inside the classifier.

The coefficient of viscosity of air was calculated as [15]:

$$\mu = \mu_{23°C}\left(\frac{T}{296.15}\right)^{1.5}\left(\frac{286.15+110.4}{T+110.4}\right) \tag{19}$$

where

$\mu_{23°C} = 1.93245 \times 10^{-4} P$.

3.2 Verification of Correct Classifier Performance

To ensure correct operation of the electrostatic classifier, calibrations were performed and performance tests were conducted. The voltage and flow meters were calibrated, the effect of humidity on volumetric flow rate was measured, the transfer function of the classifier was measured and compared to the theoretically predicted transfer function. A sensitivity analysis was performed to verify the theoretical relationships describing the classifier's dependence on the operating pressure and the flow rate. The repeatability of size measurements was checked and the classifier measurements were tested with Standard Reference Material particles.

3.2.1 Calibration of the Flowmeters and Voltage Meter

Voltage Meter Calibration

The center rod voltage meter was calibrated with a precision voltage meter capable of reading voltages up to 10,000 V. The accuracy of the calibrating meter is estimated as ±0.2%. The calibration was accomplished by connecting the calibrating voltage meter to the lead from the power supply. The center rod voltage meter was calibrated from 1000 to 9,000 V. The calibration indicated that the center rod voltage meter was indicating voltages higher than were actually present by about 2% at 4,000 and 3% at 9,000 V. For sizing 0.1 μm particles using 333 cm^3/s sheath air, a 2% error in voltage at the nominal voltage peak of 3,800 V corresponds to a 1% error in particle diameter. For sizing 0.3 μm particles using sheath air at about 167 cm^3/s, a 3% error in voltage at a nominal voltage peak of 8,000 V corresponds to a 2% error in diameter.

Flowmeter Calibration

Calibrations of the mass flowmeters used to control sheath air flow, excess air flow, and monodisperse air flow were performed to improve the accuracy of the size measurement. The calibrations were performed at the NIST flow calibration facility using the "piston prover" apparatus, maintained as the primary standard for calibration of gas flow meters. The apparatus consists of a volume displacement device incorporating a mercury-sealed piston inside of a glass cylinder. For calibration of a flow meter, dry gas is passed through the meter and into the calibration cylinder. The piston is displaced through an accurately defined volume in an accurately measured time. A bypass valve allows re-routing of the gas stream so the piston may be returned to its original configuration between each calibration run. Measurements of temperature and pressure are recorded so that the mass flow rate can be determined.

In order to eliminate changes in the flowfield experienced by the flowmeters, the calibrations were conducted without removing the flowmeters from the classifier. The configuration of the classifier allowed simultaneous calibration of either the sheath air meter and the excess air meter, or the sheath air meter and the monodisperse aerosol meter. To calibrate the sheath air meter and the excess air meter, the monodisperse aerosol outlet valve was closed and the polydisperse aerosol inlet was plugged. To calibrate the sheath air meter and the monodisperse aerosol meter, the polydisperse aerosol inlet was left plugged, the excess air valve was closed, and the monodisperse aerosol valve was left fully open.

The calibrations were performed with the classifier valves in their normal configuration (excess air and monodisperse aerosol valves fully open). The valve on the sheath air inlet was adjusted to provide an upstream air pressure of about 1.60×10^4 Pa, and this pressure was maintained during normal operation of the classifier.

During calibration, the flow rate was approximately selected using the manufacturer's original calibration. The meter readings were recorded, and the flow rate was measured using the "piston-prover" calibration apparatus described above. The flow rates chosen for calibration of the flowmeters were nominally 333, 167, and 50 cm^3/s for the sheath air and excess air flow rates. These flow rates were chosen to maximize the flow accuracy for sizing 0.1 μm, 0.3 μm SRM, and 0.9 μm SRM particles, respectively. For the monodisperse aerosol flow meter, the calibration flow rates ranged from 33.3 to 4.2 cm^3/s. The flow meters were calibrated at additional flow rates in the vicinity of the nominal values listed above.

Each calibration point was repeated five times on two consecutive days, and a partial calibration was conducted 1 week later to check for meter drift. The accuracy which is normally quoted by the NIST calibration facility is on the order of ±0.25%, with 99% confidence. As will be discussed later, the estimate of uncertainty in the flowmeters used during operation of the classifier is conservatively estimated to be ±1% due to additional uncertainties in the meter setting and

the temperature and pressure which are used to convert the mass flow rate to the volumetric flow rate [eq (15)]. The calibration conducted a week after the initial calibration did not indicate a significant drift for the higher flow rate calibrations (maximum shifts for sheath and excess air: 0.05% at 33.3 cm^3/s 0.14% at 167 cm^3/s, and .01% at 333 cm^3/s). Drift associated with the monodisperse aerosol meter using lower flow rates was slightly higher, with the maximum shift between the three calibration days of about 0.5% for flow rate settings of nominally 33.3, 16.7, and 4.2 cm^3/s.

The manufacturer's calibration for the sheath air meter indicated lower flow rates by about 5% at nominally 333 cm^3/s and 3% at nominally 167 cm^3/s compared to the NIST flow rate calibration. The manufacturer's calibration for the excess air meter was found to be 8% lower at nominally 333 cm^3/s and 7% lower at nominally 167 cm^3/s. For sizing 0.1 μm particles, an error in the sheath air of 5% at 333 cm^3/s corresponds to a diameter error of about 3%. It should be noted that although the electrostatic classifier was not used until initiation of this project in 1988, the calibration is dated 7/83. Also, the larger uncertainties seen in the excess air meter may be due to the uncertainty in the meter setting caused by a significant amount of rapid fluctuation in the meter reading.

3.2.2 Effect of Humidity on the Volumetric Flow Rate Since the molecular weight of a water molecule is less than the molecular weight of air, for a given mass flow rate, the equivalent volumetric flow rate of wet air should be higher than the volumetric flow rate of dry air. Water vapor, produced by the atomizer, leads to high humidities of the air exiting the atomizer. While the drying tube and dilution of the atomizer aerosol with dry air reduces the humidity of aerosol entering the classifier, the resulting air humidity is still higher than the humidity of the air used during flowmeter calibration. The air used for sheath air is sent through a diffusion dryer providing relative humidities on the order of 5%. The relative humidity of the aerosol at the classifier inlet can be high if low dilution air is used. The flow rate from the atomizer without dilution is 83.3 cm^3/s, and a typical dilution air flow is about 80 cm^3/s. When the atomizer was used with the impactor, the relative humidity of the aerosol at the inlet to the classifier was measured to be around 25% and about 7% at the excess air outlet.

For wet air, the volumetric flow rate correction made to the flowmeter calibration is slightly different from the correction made for dry air. Assuming flowmeter calibrations are conducted with dry air, the volumetric flow rate correction for wet air, derived based on ideal gas considerations, is as follows [compare to eq (15)]:

$$Q_{vol} = Q_{cal} \cdot \frac{T_{actual}}{T_{cal}} \cdot \frac{P_{cal}}{P_{air} + P_{H_2O} \frac{M_{H_2O}}{M_{air}}} \qquad (20)$$

Q_{vol} = volumetric flow rate of wet air
Q_{cal} = calibrated volumetric flow rate at T_{cal},P_{cal}
P_{air} = partial pressure of air
P_{H_2O} = partial pressure of water vapor
M_{H_2O} = molecular weight of water
M_{air} = molecular weight of air.

The effect of relative humidity on volumetric flow rate predicted by eq (20) is summarized below:

R.H. (%)	Q_{vol} with R.H. correction / Q_{vol} no R.H. correction	
0	1.000	
10	1.001	(0.1%)
20	1.002	(0.2%)
50	1.006	(0.6%)
70	1.009	(0.9%)
100	1.012	(1.2%)

Typical relative humidities of the excess air measured when sizing 0.1 μm particles were 5-15%. The relative humidities existing when sizing the 0.3 and 0.9 μm SRM particles were higher (when the atomizer is used without the impactor, more water vapor is produced). The humidities were not measured in these cases; however, an upperbound humidity of 25% is estimated based on 100% humidity of the inlet aerosol and a factor of 10 dilution by the dry sheath air. Particle diameter measurements made without correcting the flow rate for relative humidity will result in an increase in the measured diameter by a magnitude approximately half the flow volume ratios shown above.

The effect of humidity on the volumetric flow rate was experimentally investigated using a gas-test meter. Maintaining a given voltage on the mass flowmeter, the volumetric flow rates were measured with different air humidities. It was found that changing the humidity from 5% to 60% for fixed mass flow rate increased the volumetric flow rate by less than 0.5%, which was at the resolution limit of the flow measurement. This finding is consistent with eq (20), but the measurement resolution is inadequate to provide a quantitative test of the

equation. In any event for the 0.1 μm PSL spheres with a humidity of 5-15%, the predicted humidity correction to the volumetric flow rate is less than 0.2%.

3.2.3 Testing the Transfer Function To determine whether the classifier is operating correctly, its performance can be judged by comparing the theoretical and experimental output of the classifier when classifying a monodisperse aerosol. Figure 8a shows a plot of concentration vs center rod voltage for 0.269 μm PSL under the condition of equal aerosol flow rates. Also shown on the curve is the theoretical voltage-concentration curve plotted about the peak concentration voltage, which was obtained from figure 5 and eq (11) with $Q_c = Q_m = 167$ cm³/s and $Q_a = Q_s = 17$ cm³/s. While Figure 8a indicates approximately correct behavior, the slight uncertainty in the peak concentration causes uncertainty in the placement of the theoretical transfer function. This uncertainty is the result of the rounding effect at the peak caused by slightly unequal aerosol flow rates. A better comparison is obtained if the aerosol flow rates are not equal. The flow rate of the aerosol entering the classifier was reduced by a factor of two, $Q_a = 8.5$ cm³/s, while the sheath flow was increased by 8.5 cm³/s so $Q_c = 175$ cm³/s (fig. 8b). The data in figure 8b allows definite placement of the theoretical

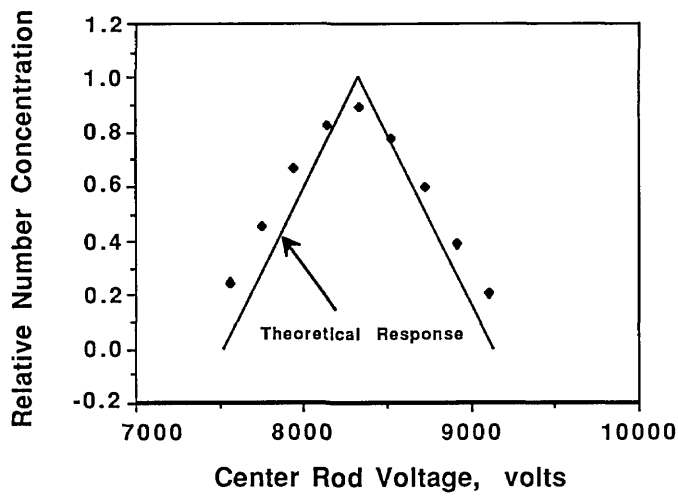

Figure 8a. Comparison of experimental and theoretical response of the classifier for 0.269 μm particles using equal aerosol flow rates.

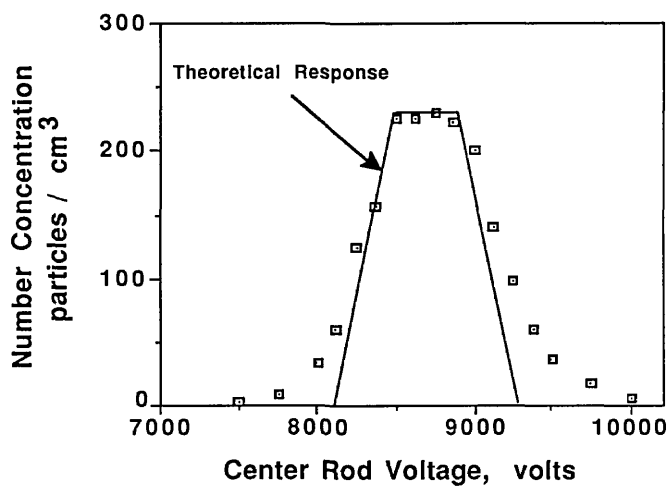

Figure 8b. Comparison of experimental and theoretical response of the classifier for 0.269 μm particles using different aerosol flow rates.

transfer function and indicates correct classifier output. Slight differences between the theoretical transfer function and the experimental transfer function are due in part to the fact that the PSL is not perfectly monodisperse.

A second method to check for correct performance of the classifier was developed by Rader and McMurry [9] and involves the use of two classifiers in series. Such a configuration is called a TDMA (Tandem Differential Mobility Analyzer). In this method, a polydisperse aerosol is sent through the first classifier to produce a test aerosol for the second classifier. The voltage on the first classifier is held constant while the voltage on the second classifier is varied to trace the distribution of the test aerosol. The concentration-voltage data of the second classifier is then compared to the TDMA theory using a computer algorithm which estimates the ratio of sheath to aerosol flow rates by fitting the theoretical relationships to the voltage-concentration data. Agreement between the actual flow ratio and the fitted flow ratio is an indication that the classifiers are operating correctly. This method was used to test the performance of the NIST classifier using a second classifier of the same type and model to complete the TDMA system. The second classifier was provided by the University of Minnesota Particle Technology Lab. The results of the TDMA test indicated the classifier was operating correctly. (For a sheath to aerosol flow ratio of 10.0, the algorithm indicated a ratio of 9.8 with the NIST classifier used as the second classifier in the TDMA system, and a ratio of 10.0 with the NIST classifier used as the first classifier in the TDMA system.)

A third test of the classifier's performance is to compare the experimental peak concentration at the output of the second classifier ($N_{2\,out}$) to the concentration at the input to the second classifier (N_{in}). From the triangular shape of the inlet mobility distribution function (see fig. 5) and from a similar triangular shape for the sampling efficiency of the second classifier, Kousaka et al. [7] derived the following relationship between $N_{2\,out}$ and N_{in} for the case where the voltage of the second DMA is set equal to the first:

$$\underset{\text{(theoretical)}}{N_{2\,out}} = \left(\frac{2}{3}\right) N_{in}. \tag{21}$$

The following experimental results indicate again that the classifier performs as predicted:

$N_{2\,out}$	N_{in}	$\underset{\text{(theoretical)}}{N_{2\,out}} = \left(\frac{2}{3}\right)N_{in}$	$\frac{N_{2\,out}}{N_{2\,out}\ \text{(theoretical)}}$
335	540	360	0.93
445	730	486	0.92

The 7% to 8% difference between the actual and theoretical downstream concentrations is due to particle wall losses within the second DMA and to slight differences between the actual and theoretical transfer functions.

3.2.4 Sensitivity Analysis To investigate the equations governing the size measurement of the PSL spheres, the operating conditions of the classifier were varied slightly and then the PSL spheres were sized. If the equations governing particle size measurement are correct, the measured particle diameter should remain the same regardless of which operating conditions are used.

The experimental method was straightforward. The variables which lend themselves to variation are flow rate and operating pressure. The flow rate affects the relationship between the center rod voltage and the particle electrical mobility [eq (12)], and the pressure effects the volumetric flow rate [eq (15)] and the particle slip correction [eq (17)] through its effect on the mean-free path of air [eq (18)]. The measurement consisted of first sizing 0.1 μm PSL using nominally 333 cm^3/s sheath flow and excess flow rates, and a normal operating pressure of approximately 3.5×10^3 Pa above ambient. The particle diameter measured with these operating conditions was compared to the diameter measured when the flow rate or pressure were changed. Equivalently, the governing equations can be used to predict the change in the peak voltage which should result when a different flow rate or pressure is used for the measurement. The predicted peak voltage can be compared to the experimentally measured peak voltage.

Operating Pressure Variation

The measurement using different operating pressures was done by restricting the excess air valve so that the pressure inside the classifier increased from the normal operating pressure of 3.5×10^3 Pa above ambient to about 1.27×10^4 Pa above ambient. The increase in pressure results in a decrease in the volumetric flow rates [eq (15)], and a decrease in the particle slip correction factor [eq (17)]. The governing equations [eqs (1) and (12)

together with the expression for the slip correction] predict that the increase in pressure should result in a decrease in the peak voltage of about 3%, which was within 0.2% of the measured decrease in the peak voltage, 3780 to 3685 V. The particle size measured with a pressure of 1.27×10^4 Pa was within 0.1% of the size measured using the normal pressure of 3.5×10^3 Pa. The agreement between the two measurements of particle diameter and the agreement between the predicted and measured change in the peak voltage indicate that the pressure variable is incorporated correctly into the governing equations of the particle measurement.

Sheath Flow Variation

The sheath flow rate was decreased from 333 to 300 cm^3/s while keeping the excess air flow rate at 333 cm^3/s. To maintain a flow balance, the polydisperse aerosol flow rate was operated at 66 cm^3/s, while the monodisperse aerosol flow rate was operated at 33 cm^3/s. In this case, the governing equations predict a decrease in the peak voltage of about 6% which was within 0.6% of the measured change in peak voltage, 4240 to 4000 V. The difference between the particle size measured using the normal operating conditions and the varied-flow rate conditions was less than 0.3%. This difference is probably caused by a dependence of measured particle diameter on the aerosol flow rate, which is discussed below.

Aerosol Flow Variation

Particle sizing was also conducted using different aerosol flow rates. In this case, the theory predicts a change in the mobility width of the monodisperse aerosol outlet particles [eq (13)], but does not predict a change in the mean electrical mobility or measured particle diameter. A high aerosol flow rate corresponds to a wide electrical mobility range of the particles sampled through the slit in the center rod. A low aerosol flow rate corresponds to a narrow electrical mobility range of the monodisperse aerosol outlet particles.

To study the effect of the aerosol flow rate on particle size, the sheath flow and excess flow rates were kept constant and equal while the two aerosol flow rates were varied in tandem. Figures 9 and 10 show the effect of aerosol flow rate on the voltage-concentration curve for 0.269 μm and 0.1 μm PSL spheres. The sheath flow and excess flow rates were 167 cm^3/s for the 0.269 μm particles and 333 cm^3/s for the 0.1 μm particles. Figures 9 and 10 show the distribution plotted with both actual concentration and normalized concentration. Plotting normalized concentration allows direct comparison of the peak voltage. For the 0.1 μm distribution, the particle diameter increases about 1% as the aerosol flow rate was decreased from 33.3 to 5.0 cm^3/s. The voltage peak was determined by averaging the concentration-voltage data, using eq (16), for concentrations greater than 0.6 N_{max}. For the 0.269 μm PSL spheres, an increase in diameter of about 1% was also found for decreasing aerosol flow rates.

The reason for this increase in particle size is not presently known. The slight sizing dependence on aerosol flow rate is negligible for typical applications of the electrostatic classifier. This effect apparently has not been reported in the literature. For this work, the increase in measured diameter for decreasing aerosol flow rates is included as an uncertainty in the measured diameter.

3.2.5 Sizing Repeatability The 0.1 μm PSL size measurement was repeated eight times on one day and six times about a week later. The 14 measurements are shown in table 1. The sheath flow and excess flow rates used for these measurements were 340 and 330 cm^3/s for the first and second days, respectively, while aerosol flow rates were nominally 33 cm^3/s. The coefficient of variation (*CV*) of the 14 measurements is 0.2%. The size measurements for runs 1-3 on day 1 are thought to have been affected by a gradually changing inlet concentration. If runs 1-3 on day 1 are discarded, the *CV* of the measurements is 0.1%.

3.2.6 Measurement of Standard Reference Material Particles As a test of the sizing accuracy of the classifier, Standard Reference Material particles (NIST SRM 1691 at 0.269 ± .007 μm, and NIST SRM 1690 at 0.895 ± .008 μm) were sized. The resulting size measurements are shown in table 2. The measurements were made immediately following the flowmeter calibration and include the voltage calibration. The 0.269 μm SRM particles were measured using sheath flow and excess flow rates of 167 cm^3/s and aerosol flow rates of 17 cm^3/s. The 0.895 μm SRM particles were measured using sheath flow and excess flow rates of 41.7 cm^3/s and aerosol flow rates of nominally 5 cm^3/s. The 0.269 μm SRM particles, measured for the SRM report using electron microscopy, were measured with the classifier to have a mean diameter of 0.273 μm, which is 1.6% larger than the SRM reported diameter. The uncertainty in the diameter of the 0.269 μm particles is 2.6%. The 0.895 μm SRM particles, measured for the SRM report using a light scattering technique, were measured with the classifier to have a mean diameter of 0.910 μm, which is 1.7% larger than the SRM reported diameter. The uncertainty in the diameter of the 0.895 μm particles is ±0.9%.

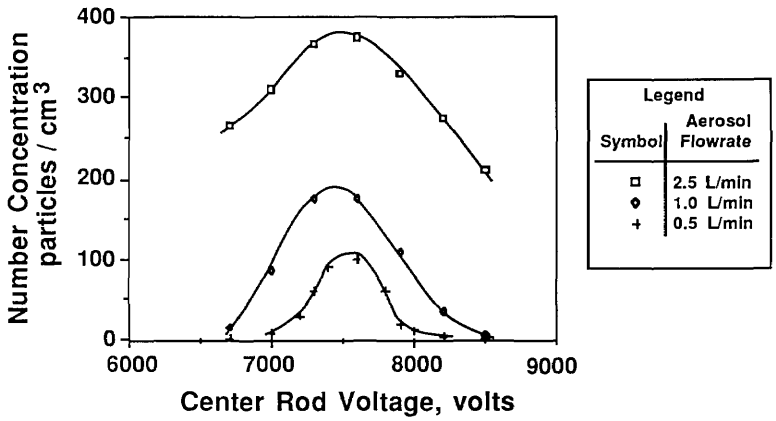

Figure 9a. Voltage vs experimental concentration for 0.269 μm particles for three different aerosol flow rates.

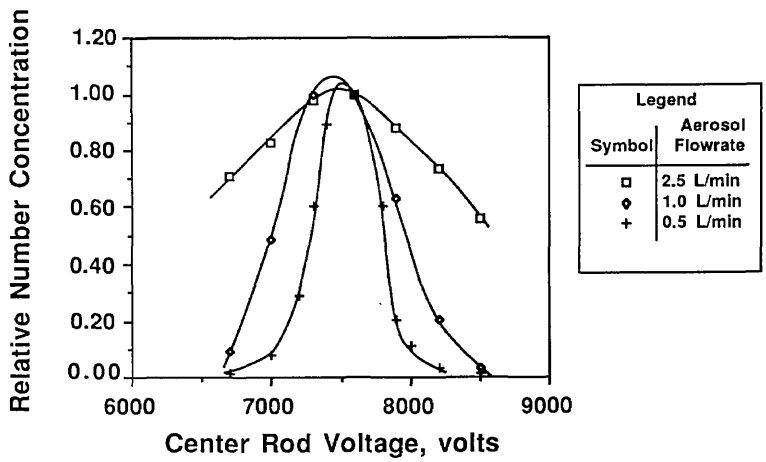

Figure 9b. Voltage vs relative concentration for 0.269 μm particles for three different aerosol flow rates.

While both measurements are larger than the SRM reported diameters by a similar percentage, the measurement of the 0.269 μm particles lies within the uncertainty quoted for the SRM measurement, but the measurement of the 0.895 μm SRM particles is outside of the error band quoted for the SRM measurement. It should be noted that the measurement of the 0.895 μm SRM particles was conducted using significantly different flow conditions (41.7 cm^3/s) than those used for the 0.1 and 0.269 μm SRM particles (333 and 167 cm^3/s sheath flows, respectively). The 0.895 μm particle measurement can be repeated using higher sheath flows by measuring multiply charged particles. This method is described below in section 3.2.7.

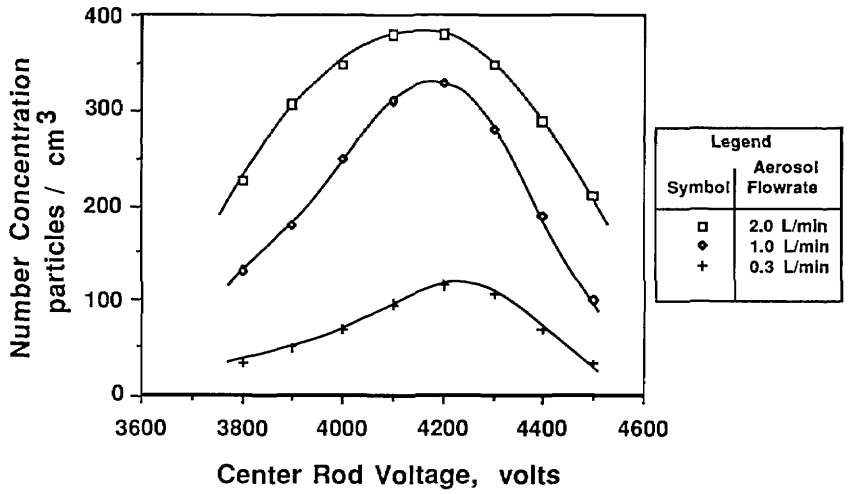

Figure 10a. Voltage vs experimental concentration for 0.1 μm particles for three different aerosol flow rates.

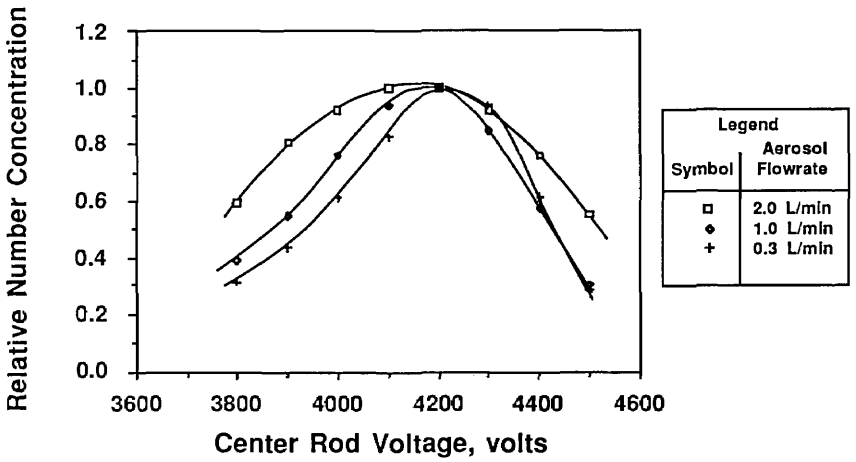

Figure 10b. Voltage vs relative concentration for 0.1 μm particles for three different aerosol flow rates.

3.2.7 Calibration of the Electrostatic Classifier Using Standard Reference Material Particles One possible explanation for the difference between the electrical mobility results for particle size and the certified particle size is an error in the definition of the length of the classifier. Recall that the length dimension is used in eq (12) to calculate the particle electrical mobility from which the particle size is calculated using eq (1). At present, the length is defined as the distance from the midpoint of the monodisperse aerosol exit slit to the midpoint of the aerosol inlet (see fig. 3). This choice of length

Table 1. Repeatability of 0.1 μm particle diameter measurements

Day 1 (May 27)		Day 2 (June 1)	
Run number	Measured diameter μm	Run number	Measured diameter μm
1	0.1073	1	0.1070
2	0.1072	2	0.1067
3	0.1074	3	0.1069
4	0.1070	4	0.1067
5	0.1069	5	0.1068
6	0.1069	6	0.1068
7	0.1070		
8	0.1068		
$\overline{D}$	= 0.1071 μm	$\overline{D}$	= 0.1068μm
σ_{n-1}	= 0.0002 μm (0.2%)	σ_{n-1}	= 0.0001 μm (0.1%)

Combined Analysis

$\overline{D}$ = 0.1069 μm

σ_{n-1} = 0.0002 μm (0.2%)

Table 2. Summary of measurements of 0.3 and 0.9 μm Standard Reference Material particles

Standard Reference Material 1691—0.3 μm particles	
Measured diameter —	0.2731 μm
	0.2731
	0.2736
	0.2731
	0.2734
$\overline{D}$ =	0.2733 μm
σ_{n-1} =	+ 0.0002 μm (0.1%)
D_c [a] =	0.269 ± 0.007 μm (±2.6%)
$\overline{D} - D_c$ =	+ 0.0043 μm(1.6%)

Standard Reference Material 1690—0.9 μm particles	
Measured diameter —	0.9103 μm
	0.9075
	0.9132
$\overline{D}$ =	0.9103 μm
σ_{n-1} =	0.003 μm (0.3%)
D_c [b] =	0.895 ± 0.008 μm (±0.9%)
$\overline{D} - D_c$ =	+ 0.015 μm (1.7%)

[a] Certified diameter for NIST Standard Reference Material 1691.
[b] Certified diameter for NIST Standard Reference Material 1690.

is consistent with the analysis by Knutson and Whitby [1] assuming axisymmetric and laminar flow and a uniform electric field in the axial direction. These conditions will be violated to some extent at the aerosol entrance and exit to the classifying column. These effects might be incorporated in eq (12) as a corrected length of the classifier. If the length used in the calculations is taken as 1.9% shorter than the presently defined length, (44.44 cm changed to 43.60 cm), the classifier measurements of both SRM particle sizes agree within 0.1% with the SRM reported diameters. The length dimension was measured in this study to be 44.37 cm which is in close agreement with the 44.44 cm measurement reported by the manufacturer. While the length can be adjusted so the classifier indicates the correct size for both SRM particle sizes, the required change in length may be too large to claim that the measurement differences are due to an error in the length definition.

Adjusting the length definition as suggested above is one method of calibrating the electrostatic classifier for measurement of the 0.1 μm particles. A more rigorous approach for calibrating the classifier, which is suggested for future consideration, is to measure the 0.269 and 0.895 μm SRM particles using the same sheath and aerosol flow rates as used for the measurement of 0.1 μm particles. The calibration technique involves measuring the electrical mobility of multiply charged 0.269 and 0.895 μm SRM particles. Since a multiply charged particle has a higher electrical mobility than a singly charged particle, a higher flow rate can be used in the classifier to measure the mean particle mobility and particle diameter. By measuring the multiply charged SRM particles with the same flow conditions as the 0.1 μm particles, a calibration factor (such as changing the length definition) can be included in the governing equations which forces the SRM particle measurements to be in agreement with the reported diameters. This method of calibration is thought to be more rigorous since all the particles are measured with the same flow conditions.

3.3 Investigating the Effect of Impurities

As was discussed in section 2.1, impurities in the water used to suspend the PSL spheres produce a layer of residue on the surface of particles after the PSL-carrying atomizer droplets evaporate. This residue results in a systematic error in particle diameter measurements since it increases the apparent particle diameter. The impurities in the PSL particle suspension come from impurities existing in the water used to dilute the concentrated PSL particle suspension and from the impurities in the liquid used in the concentrated PSL particle suspension. To estimate the thickness of the impurity residue on the PSL sphere, it is necessary to know the impurity concentration in the PSL particle suspension and the diameter of the particle-carrying droplet. Assuming all of the non-volatile impurity forms a uniform residue shell around the particle, the following relationship between the thickness of the residue on the particle and the impurity concentration, particle diameter, and droplet diameter is obtained:

$$t = \frac{C(D_d)^3}{3(D_p)^2} \tag{22}$$

where

t = impurity addition to diameter (μm)

C = volumetric concentration of impurities

D_d = PSL-carrying droplet diameter before evaporation (μm)

D_p = PSL particle diameter (μm).

To estimate the effect of impurities on the particle size, measurements were performed to determine the PSL particle-carrying droplet diameter before evaporation, the concentration of impurities in the water used to dilute the PSL particle suspension, the impurities in the diluted PSL particle suspension, and the impurity concentration effect on particle diameter.

3.3.1 Characterizing the Atomizer As seen in eq (22), the PSL-carrying droplet diameter strongly influences the effect of impurities on particle diameter. The droplet distribution was determined by atomizing a solution containing a known concentration of NaCl, and measuring the resulting residue particle size distribution using the classifier.

The droplet size distribution can then be determined using the simple relationship between the impurity concentration, C, residue particle size, D_p, and the droplet size, D_d:

$$D_p = D_d \cdot C^{(1/3)}. \quad (23)$$

The atomizer can be used in two configurations. First, for sizing the 0.1 μm particles, an impactor is used at the outlet of the atomizer to remove large droplets (see fig. 2). Without the impactor the larger droplets, capable of carrying larger PSL spheres, are allowed to pass through the outlet of the atomizer. Figure 11 shows the number distribution of droplets produced with and without the impactor. With the impactor in place, the mode of the number distribution is around 0.7 μm. Without the impactor, the mode of the number distribution is around 0.8 μm, with significantly more large droplets than exist with the impactor. The effect of the impactor is more obvious if the droplet distribution is weighted by mass or volume as shown in figure 12.

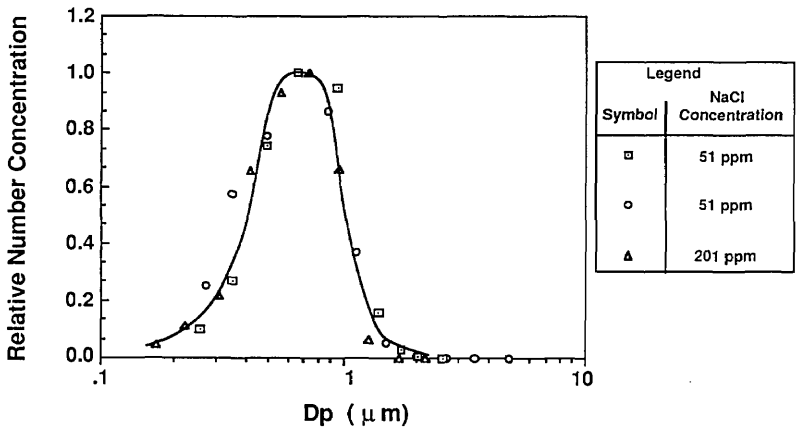

Figure 11a. Droplet number distribution with impactor.

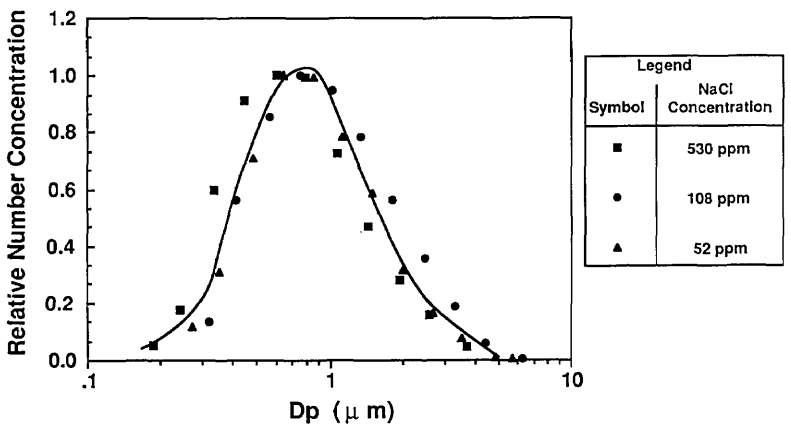

Figure 11b. Droplet number distribution without impactor.

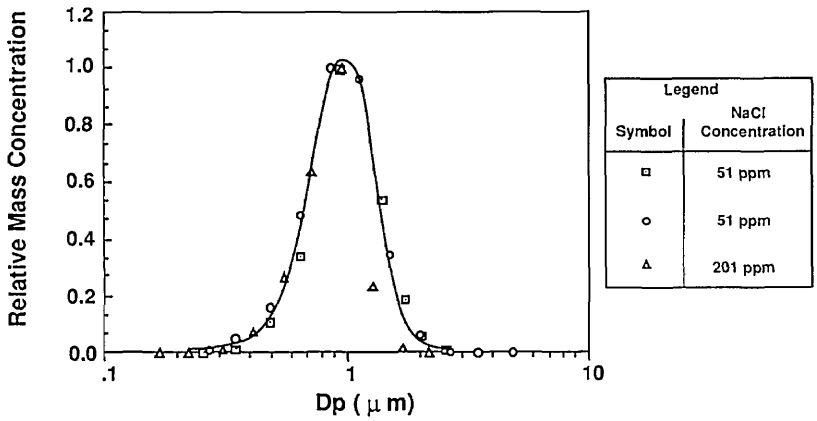

Figure 12a. Droplet mass distribution with impactor.

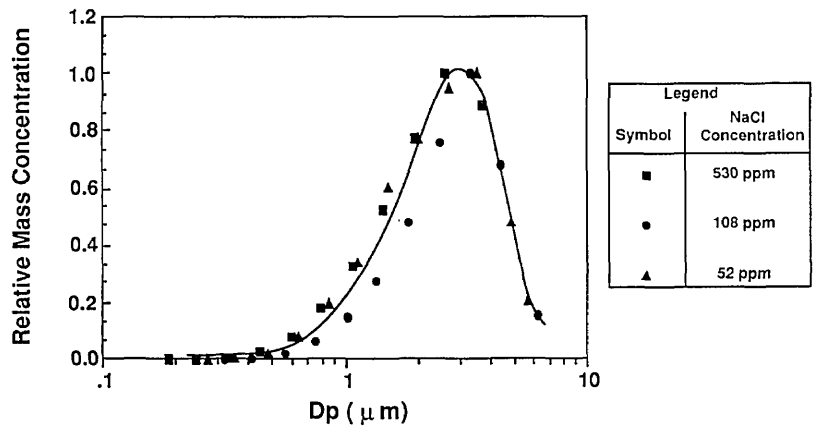

Figure 12b. Droplet mass distribution without impactor.

Similar measurements of an atomizer's droplet distribution using this technique, reported by Niida et al. [16], suggest that the droplet distributions measured in this work are biased toward larger particles because of diffusional losses of small residue particles upstream of the classifier. The measured droplet distributions are only qualitatively representative of the actual distributions. The droplet distribution of the atomizer suggests that sizing PSL spheres without the impactor in place will result in larger PSL particle-carrying droplets, and more significant impurity effects.

3.3.2 Measuring the Concentration of Impurities in the Water Used to Dilute the PSL Particle Suspension The volumetric impurity concentration was measured for tap water and distilled, deionized water using three methods. The tap water impurity concentration measurements were conducted for comparative purposes. Two measurement methods involved evaporating droplets and measuring the resulting residue particle size. The third method involved gravimetric measurements of evaporation residue.

Classifying Atomized DI Water

In the first method used to estimate water impurities, the water was atomized without PSL or other additives. The atomizer was used without the impactor so that larger residue particles were formed. The droplets formed from the atomization were dried and the resulting residue particles were sized using the classifier. This measurement was done for tap water and distilled, deionized (DI) water, and the resulting mass distributions are shown in figures 13a and 13b along with the residue particle distributions produced by atomizing a known solution of NaCl.

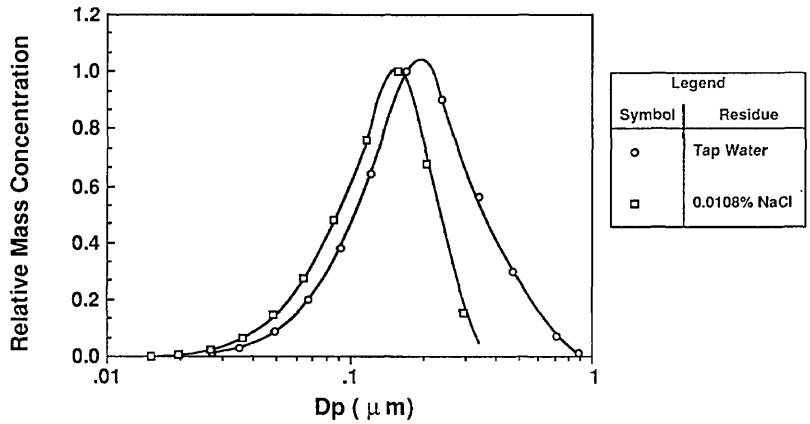

Figure 13a. Comparison of residue particles for tap water and 0.010% NaCl.

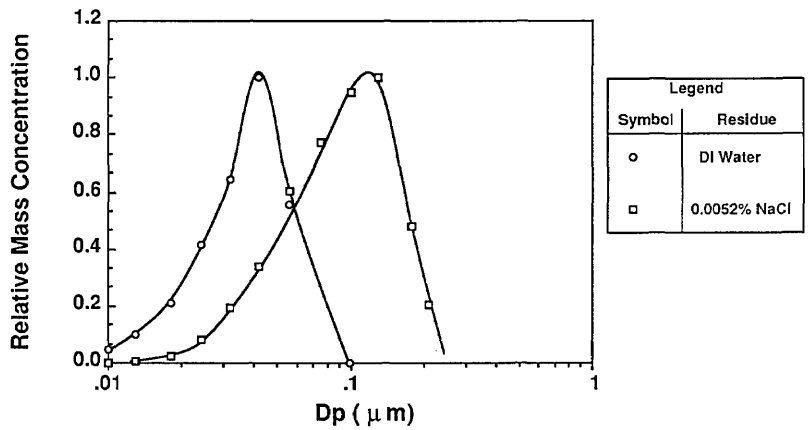

Figure 13b. Comparison of residue particles for deionized water and 0.0052% NaCl.

The calculation of impurity concentration is accomplished by comparing the means of the mass distributions of the water residue and NaCl residue particles. The DI water residue particles were compared to the residue particles produced from a solution of 0.0052% NaCl by volume. The tap water residue particles were compared to the residue particles produced from solution of 0.0108% NaCl by volume. The impurity concentrations were calculated from the following expression derived from eq (22):

$$C_{\text{water}} = \left(\frac{D_{\text{p NaCl mode}}}{D_{\text{p water mode}}}\right)^3 \times C_{\text{NaCl}} \qquad (24)$$

where

C_{water} = volumetric impurity concentration in water

C_{NaCl} = volumetric concentration of NaCl

$D_{\text{p NaCl mode}}$ = mode of the NaCl residue distribution

$D_{\text{p water mode}}$ = mode of the water residue distribution.

The result of the impurity measurement follows from figures 13a and 13b:

Atomizer solution	Residue particle mode (μm)	Volumetric impurity concentration	Uncertainty
0.0052% NaCl	0.11	0.0052% (52 ppm)	
DI-water	0.04	0.0002% (2 ppm)	±1 ppm[a]
0.0108% NaCl	0.15	0.0108% (108 ppm)	
Tap water	0.20	0.026% (260 ppm)	±70 ppm

[a] Uncertainties resulting from estimation of mode diameter.

One problem with sizing the residue particles from the DI water is the loss of particles downstream of the atomizer before being classified. To reduce electrostatic losses a Kr-85 bipolar charge neutralizer was added at the outlet of the atomizer for the DI water residue particles and the 0.0052% NaCl residue particles. Evidence of these losses is apparent from the observation that the number

concentration of residue particles for the 0.0052% NaCl solution is about 30 times greater than the concentration of the residue particles produced from the DI water. This would suggest that the mode of the number distribution of the residue particles from the DI water is outside the range of the classifier. The mode of the mass distribution of the residue particles appears to be within the range of the classifier.

Classifying Residue Particles From the Vibrating Orifice

The second method used to determine the volumetric concentration of the impurity in the water again involved sizing the residue particles produced by evaporating large water droplets of known size. In this method the Vibrating Orifice Monodisperse Aerosol Generator (VOAG) (TSI, Inc., Model 3450) was used to produce large monodisperse water droplets. The vibrating orifice generator was operated without a filter on the liquid pump so that impurities were not removed from the solution being tested. The VOAG was used to produce 39 μm droplets of the DI water. The resulting residue particles were sized with the classifier. Except for a secondary peak corresponding to doubly-charged particles, the residue particles were monodisperse with a size of about 0.27 μm. Using eq (22), the concentration of impurities in the water is calculated to be 0.3 ppm.

This same method was used to estimate the level of impurities in normal tap water and lab distilled water. Using the classifier to size the residue particles for normal distilled water, the impurity concentration was calculated to be 5 ppm. For normal tap water, the residual particles were too large to size using the classifier. Instead the TSI Model 3310 Aerodynamic Particle Sizer (APS) was used. The resulting distribution is shown in figure 14 to have a peak particle aerodynamic diameter of about 2.7 μm. For a unit density particle, the aerodynamic diameter is equal to the geometric diameter, and the volumetric impurity concentration can be estimated using eq (22) to be 330 ppm.

Impurity Measurements using a Gravimetric Method

A third attempt at measuring the volumetric impurity concentration of the water was to evaporate a known mass of water and measure the resulting impurity mass. This method did not work for the distilled water or the DI water because the impurity mass was too low. The method did work for the tap water and indicated a mass concentration of about 220 ppm.

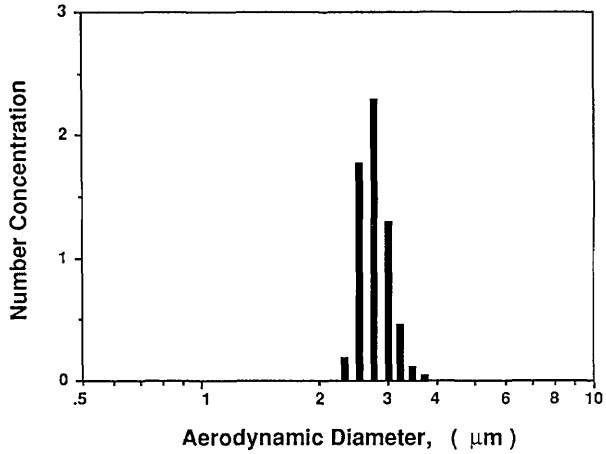

Figure 14. Tap water residue particles produced by the vibrating orifice and measured with the aerodynamic particle sizer.

The three methods for measuring the impurity concentration are qualitatively in agreement. For the deionized/filtered water, the methods indicated impurity concentrations on the order of 1 ppm. The impurity concentration measurements of the tap water were conducted to compare the different methods. The measurements made with the VOAG-APS and the gravimetric method are in qualitative agreement, with best agreement occurring if unit density impurity is assumed. For unit density impurity, the VOAG-APS indicates 330 ppm volumetric impurity and the gravimetric method indicating 220 ppm volumetric impurity. As stated above, the tap water impurity was measured by sizing residue particles from the atomizer to be about 260 ppm.

3.3.3 Estimating the Impurity Concentration in the PSL Particle Suspension In the previous section, the impurity concentration in the water used to dilute the PSL suspension was measured. The second source of impurities, the concentrated PSL suspension, is considered below. The total nonvolatile impurity concentration in the diluted suspension is estimated in this section and also the predicted effect of the impurity on the particle diameter is compared with measurements.

Calculation of the Impurity Concentration

Concentrations of impurities in the solids composing PSL particle suspensions have been reported to be from about 1 to 7% [17]. If the concentrated PSL particle suspension is not sufficiently diluted with water, these impurities will have a significant

effect on the resulting particle size. For the 0.1 μm particles, the percentage of solids in the concentrated PSL suspension was about 10%. Dilution of the concentrated suspension was normally about 1 to 2500 with DI water. Assuming an impurity concentration in the PSL solids to be 3% (in the middle of the range reported by Raabe [17]), the resulting PSL particle suspension, including 1 ppm impurity in the dilution water, will have an impurity concentration of about 2.2 ppm. Using eq (22) with a droplet diameter of about 0.9 μm, the resulting residue thickness (in diameter) is about 0.00005 μm or about a 0.05% addition to the diameter. The same calculation for the 0.269 μm SRM particles containing 0.5% solids and 50 ppm of biocide in the concentrated PSL particle suspension, (assuming 3% impurities in the PSL solids, a dilution of 1 to 250, and a larger droplet diameter of 2.5 μm since sizing occurs without the impactor on the atomizer), indicates that an increase in diameter of 0.0001 μm or about 0.06% would be expected.

Measurement of the Impurity Concentration

Measuring the concentration of impurities in the actual PSL suspension is difficult. As discussed in section 2.1, the aerosol produced by the atomizer consists of both PSL spheres and impurity particles resulting from evaporation of droplets which do not contain a PSL particle. Measurement of the impurity concentration in the PSL suspension was made by classifying the entire distribution of particles existing in the PSL particle aerosol, and comparing the distribution of impurity particles to the distribution of particles produced by atomizing a solution with a known concentration of NaCl. In figure 15, the entire distribution of the 0.1 μm PSL aerosol is shown. The secondary peaks in the vicinity of the main PSL particle peak are the result of doubly charged singlet particles and various multiplet particles. The distribution of impurity particles is clearly identified. The mode of the impurity particle mass distribution was compared to the mode of residue particles produced from a 0.0052% NaCl solution indicating the impurity concentration to be about 6 ppm. This same technique was used to estimate the impurity concentration existing in the 0.269 SRM particles using a typical dilution of the concentrated PSL suspension by about 1 to 300 with DI water. The resulting impurity residue particles were compared to impurity particles from a 0.0108% NaCl solution. The measurement indicated an impurity concentration of about 52 ppm. This result is significantly higher than the estimated concentration using Raabe's estimates of impurities in the PSL solids.

Effect of Impurities on the SRM Particle Measurements

A simple method of determining whether or not the impurities in the PSL solids are contributing to measurement errors is to size the PSL spheres using a very dilute PSL particle suspension, and compare the measurement to that resulting from a very concentrated PSL particle suspension. If the impurities in the undiluted PSL suspension are causing significant measurement errors, the diameter measured using a very dilute suspension should be smaller

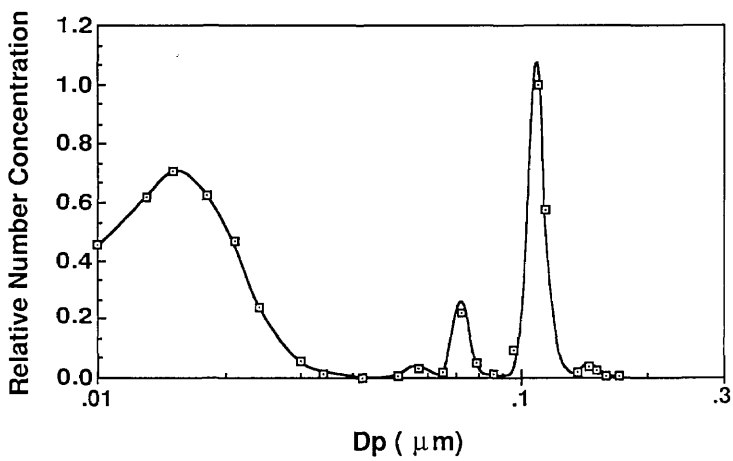

Figure 15. Number concentrations vs particle diameter for 0.1 μm PSL particles and associated impurity residue particles.

than the diameter measured using a concentrated suspension. This measurement was conducted for the 0.269 μm SRM particles. The concentration of the PSL suspension was varied by over a factor of 15 (from 3 drops of undiluted PSL in 500 ml of DI water to 10 drops of undiluted PSL in 100 ml of DI water), and no systematic change in the diameter measurement was noticed.

An attempt was also made to size the 0.269 μm SRM particles using an impactor on the atomizer in an effort to reduce the effect of impurities in the suspension. The diameter measured with the impactor was similar to the diameter measured without the impactor giving strong evidence that impurities are not influencing the measurement. It is noted, however, that atomizing the 0.269 μm particles with the impactor leads to extremely low particle concentrations because most of the particles are removed by the impactor. As discussed in section 3.1, if the concentration of the PSL spheres in the aerosol is too low, significant uncertainties result. Based on these two measurements, it is concluded that impurities increase the particle diameter for the 0.269 μm SRM by less than 1%.

Effect of Impurities on Measurements of the 0.1 μm Particles

To investigate the relationship between impurity concentration and particle size, the nominally 0.1 μm PSL spheres were sized using aqueous NaCl solutions of known concentration. In this measurement, the atomizer was used with the impactor in place because without the impactor the concentration of NaCl particles overshadowed the PSL distribution. The particles were first sized using clean water for suspension and then sized using several different NaCl solutions. Figure 16 summarizes the results. One of the data points used in the figure is the result obtained when the PSL is classified with tap water. Here the impurity concentration of the tap water was 0.033% as measured by sizing the residue particles produced by the Vibrating Orifice Generator with the Aerodynamic Particle Sizer.

This data can be used to predict the effective PSL particle-carrying droplet diameter. The predicted increase in diameter by eq (22) for a droplet diameter of 0.9 μm is seen to be in good agreement with the data in figure 16. This diameter can be used, with an estimate of the impurity concentration in the PSL suspension, to calculate the expected residue thickness added to a particle. Assuming an impurity concentration in the 0.1 μm particle suspension of about 10 ppm as calculated

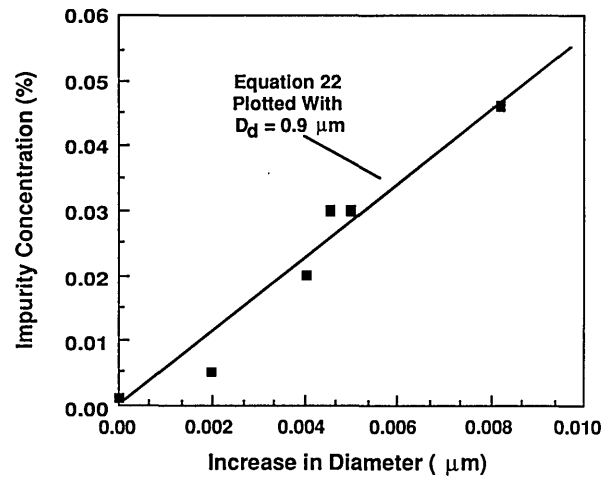

Figure 16. Impurity concentration vs increase in diameter for 0.1 μm particles in a NaCl solution.

and as measured, eq (22) is used to estimate the impurity residue increase in diameter to be about 0.2%. Several data points taken with NaCl concentrations of about 900 ppm, indicating thicknesses of about 0.01 μm, were not included in Figure 16. This data indicated much lower thickness than would be expected possibly due to clumping of the residue on the surface of the particle. This data also did not agree with droplet distribution data obtained using lower NaCl concentrations, possibly because the NaCl residue particles were forming as hollow clumps.

A final method for estimating the effect of impurities involved sizing of dilute and concentrated PSL suspensions. For PSL concentrations of 3 drops per 1000 ml to 3 drops per 25 ml of DI water, no noticeable size shift occurred. This would suggest that impurities are not influencing the measured diameter of the 0.1 μm particles. If eq (22) is used with the previously estimated impurity concentration of 6 ppm, and particle-carrying droplet diameter of 0.9 μm, the resulting increase in diameter can be estimated to be 0.00015 μm or 0.15%. The uncertainty estimate is approximate and we double the value given above so that the overall uncertainty from impurities is 0.00030 μm or 0.3%.

The use of an impactor immediately downstream of the atomizer further reduces the impurity effect by removing the larger droplets. The impactor reduces the peak voltage of the mobility distribution of the 0.1 μm particles by about 130 V as indicated in figure 17. This corresponds to about an 0.002 μm (2%) reduction in the particle size. For the estimated impurity concentration of 6 ppm, a droplet

size of 2.2 μm is estimated using eq (22). Thus it is found to be very important to use an impactor to minimize the droplet size in addition to using high purity dilution water.

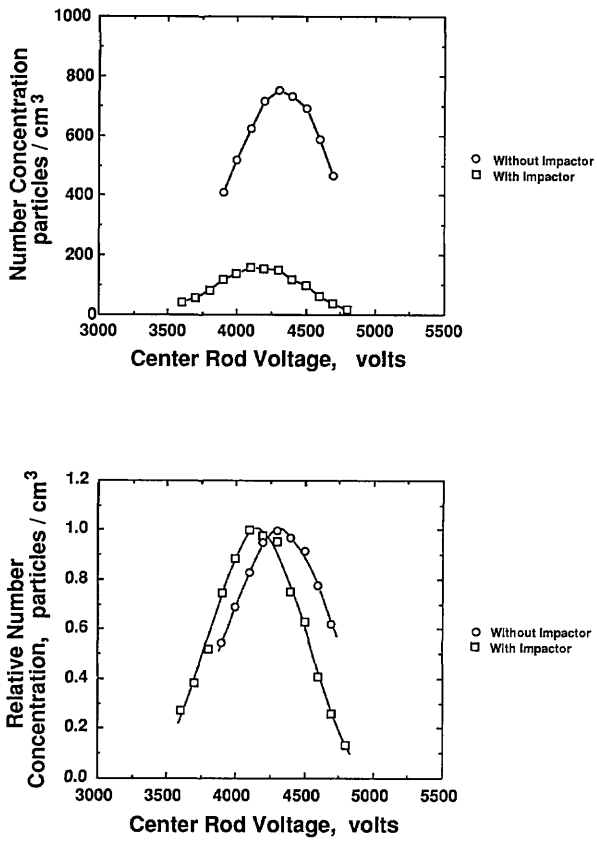

Figure 17. Effect of impactor on particle mobility.

3.4 Estimates of Uncertainty in the Classifier Performance in the Particle Diameter Measurements

In the previous section, results were presented regarding the precision associated with repeat measurements and uncertainties associated with the quantities appearing in the governing equations, eqs (1) and (12), including flow rate, voltage, and slip correction. In this section, a summary is presented of all the uncertainties and an estimate of the overall uncertainty is given for the electrical mobility classifier. An overall estimate of the uncertainty in measuring the 0.1 μm PSL spheres is obtained by combining the uncertainty associated with the impurity effect and the uncertainty associated with the use of the classifier.

3.4.1 Random Error The random component of the uncertainty associated with the measurement of the average particle size can be obtained from the 14 repeat measurements of the particle size (sec. 3.2.5). The average of these 14 measurements and the associated standard deviation, σ, are 0.1068 and 0.0002 μm, respectively. The random component of the uncertainty, R, is given by

$$R = t_{n-1}(0.025)\,\sigma/(n)^{1/2}, \qquad (25)$$

where n is the number of repeat measurements, 14, and $t_{n-1}(0.025)$ is the Student t-value for $n-1$ degrees of freedom and for 95% confidence level ($t_{13}(0.025)=2.16$). The value of R is 0.0001 μm, which corresponds to a relative error of 0.1%.

3.4.2 Uncertainty in the Flow Rate The flow rate uncertainty reported in table 3 represents a combination of flow meter calibration accuracy, precision of flow rate selection, the uncertainties in the pressure and temperature correction to the flowmeter calibration, and the effect of humidity on the flow calibration. The precision of flow rate selection is estimated to be ±0.4% reflecting the stability of the flow rate after it is set, and the precision of the initial flow rate setting. This value was calculated for the sheath air meter at nominally 333 cm³/s by estimating the precision of flowmeter voltage setting to be ±.002 V for a voltage setting of 3.160 V. The uncertainty in voltage was converted to uncertainty in flow rate using the calibration curve. The uncertainty in the calibration, normally quoted by the NIST flow calibration facility, is ±0.25% with 99% confidence. Uncertainties in the flow rate produced by the temperature and pressure correction, given by eq (15) result from uncertainties in the temperature and pressure. The uncertainty in pressure is estimated as ±3 mm Hg due to uncertainties in the barometric pressure reading, and uncertainties in measuring the pressure inside the classifier. The uncertainty in temperature is estimated as ±0.5 °C. The resulting uncertainty in volumetric flow rate due to temperature and pressure uncertainties is estimated as ±0.4%. The effect of humidity on the volumetric flow rate is estimated to be 0.2% in section 3.2.2. The sum of all the flow related uncertainties is 1.25% and the sum in quadrature is 0.5%. We use as an overall uncertainty in the volumetric flow rate an intermediate value of ±1.0%.

Table 3. Summary of uncertainties[a] associated with measurement of particle diameter

Variable	Uncertainty in variable	Resulting uncertainty in diameter
Q_c = sheath air flowrate	1.0%	0.6%
Q_m = excess air flowrate	1.0%	0.6%
r_2 = outer radius	0.3%	0.26%
r_1 = inner radius	0.2%	0.16%
L = length	0.5%	0.30%
V = center rod voltage	0.45%	0.26%
ϵ = elementary unit of charge	negligible	0.025%
μ = viscosity of air	0.04%	0.025%
C = slip correction	0.9%	0.5%
T = temperature	0.2%	0.01%
P = pressure	0.4%	0.16%
Worst case estimate from eqs (1) and (12)		±2.4%
Random error, R		±0.1%
Residual uncertainty associated with effect of aerosol flowrate on apparent size		±0.5%
Total uncertainty associated with classifier		±3.0%
Impurities related uncertainty		+0%/−0.3%
Total uncertainty—classifier + residue layer		+3.0%/−3.3%

[a] The uncertainty in particle diameter determined by electrical mobility measurements arises from the uncertainties in the variables used in eqs (1) and (12).

$$Z_p = \epsilon C(D_p)/(3\pi\mu D_p) \quad (1)$$

$$Z_p = (Q_c+Q_m)\ln(r_2/r_1)/(4\pi VL) \quad (12)$$

3.4.3 Uncertainty in Geometric Measurements The uncertainty in the values of the center rod radius, r_1, the outer cylinder radius, r_2, and the classification length, L, listed in table 3 are estimates of how accurately the measurements can be made. For the inner radius, r_1, the uncertainty of ±0.2% represents about ±0.04 mm in diameter, which includes the variability of the diameter over the length of the center rod and the difference between the diameter indicated by the manufacturer (1.874 cm) and the single measurement made during this project (1.870 cm). The uncertainty in r_2 is estimated as 0.3% in a similar manner to r_1, although its larger value represents the increased difficulty in measuring the inner diameter of the cylinder. The uncertainty in length is estimated as 0.5% reflecting both the uncertainty in measuring the length (manufacturer's measurement was 44.44 cm compared to 44.37 cm measured in this study), as well as the distortion of the electric and flow fields at the entrance and exit of the classifier column.

3.4.4 Uncertainty in Peak Voltage The uncertainty in voltage corresponding to the peak is estimated as ±0.25% corresponding to ±10 V for the nominal 0.1 μm peak voltage of 3750 V when 333 cm^3/s sheath air is used. This value of uncertainty was estimated by considering the data used during the repeatability measurement. It represents twice the voltage spread for the second day of the repeatability measurements (the repeatability measurements are shown in table 1). The uncertainty in voltage reading due to calibration accuracy is estimated as ±0.2%. Summing both uncertainty levels, the overall uncertainty in the voltage is estimated as ±0.45%.

3.4.5 Uncertainty in Slip Correction The uncertainty in the slip correction for 0.1 μm particles is estimated to be ±0.4% based on a recent study by Allen and Raabe [14]. However, there is a 2.4% difference between the slip correction computed by Allen and Raabe [14] for a Knutsen number of 1.3 (0.1 μm diameter sphere at ambient pressure) and

their earlier computation [15] based on a reanalysis of Millikan's oil drop data [18,19]. Allen and Raabe [14] attribute this discrepancy to the difference in the surface accommodation for the solid PSL spheres in their study compared to the liquid droplet surface in Millikan's studies. Because of this large difference (2.4%) and because there have been no slip correction measurements on 0.1 μm spheres, an intermediate estimate of the slip correction uncertainty of ±0.9% is used.

3.4.6 Pressure, Temperature, and Viscosity The effects of the uncertainty in the temperature and pressure measurements on the flow calibration and flow measurements has been included in the flow uncertainty. However, the temperature and pressure also affect the mean free path of the gas eq (18), which in turn affects the slip correction, and the temperature affects the viscosity eq (19). The uncertainty in the viscosity of air itself is about 0.04% [20,21].

3.4.7 Additional Uncertainties—Aerosol Flow Rate and Impurity Effect All of the uncertainties discussed above directly affect the quantities appearing in the governing equations. The uncertainty associated with varying the aerosol flow rates in tandem is not accounted for by propagating the uncertainty through the governing equations. In fact, as pointed out in sec. 3.2.4, the particle size computed from eqs (1) and (12) is not affected by changing the aerosol flow rates as long as they are kept equal. In section 3.2.4 the uncertainty associated with the aerosol flow rate is estimated to be ±0.5%.

The uncertainty associated with impurities in the water does not affect the measuring accuracy of the classifier itself, but it does lead to a systematic increase in the PSL particle diameter as an aerosol compared to the actual size of the PSL sphere without any impurity coating. The impurity uncertainty is estimated to be 0/−0.3% based on the effect of impurity concentration on the residue thickness together with the effect of an impactor on the PSL particle diameter (sec. 3.3.3).

3.4.8 Total Uncertainty in the Particle Size Measured by the Classifier All of the various sources of systematic uncertainty in regard to the electrostatic classifier are listed in table 3. A conservative measure of the combined systematic uncertainty is to consider the worst-case situation in which each variable is offset by its uncertainty to produce an extreme value of the diameter. The estimate is made by calculating the diameter using the nominal variable values and comparing to the diameter calculated if all the variables are offset by the magnitude of their uncertainty with the signs chosen so that the total uncertainty is a maximum. The percent change in the diameter is ±2.4%. Adding to this the random error, R, an overall error of ±2.5% is obtained.

There is one additional uncertainty that must be included and this is the uncertainty associated with the aerosol flow rate, ±0.5%. Adding this value to the worst case total, we arrive at our best estimate of the uncertainty in measuring particle size with the electrostatic classifier as $U = \pm 3.0\%$.

3.4.9 Total Uncertainty in the Measurement of the 0.1 μm PSL Spheres To obtain the total uncertainty in sizing the 0.1 μm diameter PSL spheres with the classifier, we must include the impurity effect. While impurities in the water and in the particle suspension do not affect the performance of the classifier, they do cause the size of the PSL sphere to be slightly larger as an aerosol compared to the size of the PSL sphere itself. In this case the error is only in the minus direction; that is, this error causes the measured size to be too large by up to 0.3%. Adding this error to the worst case estimate for U given above, we obtain a total uncertainty for the 0.1 μm PSL spheres of +3.0%/−3.3%. This corresponds to the following range in terms of particle diameter:

$$\text{Diameter} = 0.1069 \begin{matrix} +0.0032 \\ -0.0035 \end{matrix} \ \mu\text{m}.$$

4. Discussion

One way of assessing the validity of the uncertainty estimates is to compare the classifier results for the 0.3 and 1.0 μm SRMs with the certified values. In both cases the diameter obtained by the classifier method is larger than the certified value, by 1.6% for the 0.269 μm SRM and by 1.7% for the 0.895 μm SRM. The important point is that the percent difference between the SRM values and the certified values are smaller than the percent uncertainty (+3.0/−3.3) that we have estimated for the 0.1 μm particle diameter.

In a recent study, Knollenberg [10] summarized other measurements for the same batch of PSL sphere and reported 0.102 μm ±0.007 μm (Knollenberg, light scattering) and 0.105 μm (Yamada, [11], electron microscopy). There are unresolved issues about the accuracy of size measurements by electron microscopy because of the uncertainties in

the determination of the magnification and in defining the edge of the particle [22]. Yamada's study [11] has quantified the effect of the electron beam exposure time on the change in the particle diameter. The good agreement between the classifier measurements and the electron microscopy is encouraging but not conclusive because of the undefined uncertainties in the electron microscopy results.

In Knollenberg's study, the light scattering intensity of 0.1 μm PSL sphere is compared with that of 0.269 μm SRM spheres for wavelength large enough that the scattering is in the Rayleigh regime. In this case the primary source of error is the uncertainty in the SRM particle itself. The size reported by Knollenberg [10], 0.102 μm, is outside the uncertainty limits of the classifier measurement; however, the uncertainty limits for the light scattering measurement are broad (±0.007 μm) and include the 0.107 μm average size obtained by the classifier.

To further reduce the uncertainty associated with the classifier method, it is proposed that the classifier be calibrated with the 0.895 μm SRM, which has an uncertainty of ±0.9%. Both the 0.1 μm PSL and the 0.895 μm SRM would be measured using the same flow conditions in the classifier to remove the large flow uncertainty. By analyzing the multiply charged 0.895 μm particles, a high flow rate can be used in the classifier thus minimizing the uncertainties associated with operating the classifier at low flow. It is believed that the uncertainty in the determination of the average particle size for the 0.1 μm PSL can be reduced to about 1.5% by using this procedure.

Acknowledgment

This study was supported by National Institute of Standards and Technology, Contract 43NANB807219, and by the Particle Contamination Control Research Consortium at the University of Minnesota. Ken Benson and George Mattingly of NIST assisted with the flow calibrations and Martin Misakian performed the voltage calibration.

5. References

[1] Knutson, E. O., and Whitby, K.T., J. Aerosol Sci. **6**, 443 (1975).
[2] Knutson, E. O., in Fine Particles, Liu, B. Y. H. ed., Academic Press, New York (1976) p. 739.
[3] Hoppel, W. A., J. Aerosol Sci. **9**, 41 (1978).
[4] Fissan, H. J., Helsper, C., and Thielen, H. J., J. Aerosol Sci. **14**, 354 (1982).
[5] Plomp, A., ten Brink, H.M., Spoelstgra, H. and van de Vate, J. F., J. Aerosol Sci. **14**, 363 (1982).
[6] Scheibel, H. G., Hussin, A., and Porstendorfer, J., J. Aerosol Sci. **15**, 372 (1983).
[7] Kousaka, Y., Okuyama, K., and Adachi, M., Aerosol Sci. Technol. **4**, 209 (1985).
[8] Kousaka, Y., Okuyama, K., Shimada, M. and Ohshima, H., J. Aerosol Sci. **4**, 501 (1988).
[9] Rader, D. J., and McMurry, P. J., J. Aerosol Sci. **17**, 771 (1986).
[10] Knollenberg, R. G., J. Aerosol Sci. **20**, 331 (1989).
[11] Yamada, Y., Miyamoto, K., and Koizumi, A., Aerosol Sci. and Tech. **4**, 227 (1985).
[12] Liu, B. Y. H., Pui, D. Y. H., J. Colloids Interface Sci. **49**, 305 (1974).
[13] Agarwal, J. K., and Sem, G. J., J. Aerosol Sci. **11**, 343 (1979).
[14] Allen, M. O., and Raabe, O. G., Aerosol Sci. Technol. **4**, 347 (1985).
[15] Allen, M. O., and Raabe, O. G., J. Aerosol Sci. **13**, 537 (1982).
[16] Niida, T., Kousaka, Y., Oda, S., Part. Syst. Charact. **5**, 139 (1988).
[17] Raabe, O. G., in Fine Particles, Liu, B. Y. H., ed., Academic Press, New York (1976) p. 57.
[18] Millikan, R. A., Phys. Rev. **15**, 544 (1920).
[19] Millikan, R. A., Phys. Rev. **22**, 1 (1923).
[20] Birge, R. T., Am. J. Phys. **13**, 63 (1945).
[21] Millikan, R. A., Electrons (+ and −), Protons, Photons, Mesotrons, and Cosmic Rays., The University of Chicago Press, Chicago (1947).
[22] Swyt, D. A., A look at techniques for the dimensional calibration of standard microscopic particles. Natl. Bur. Stand. (U.S.) Spec. Publ. 260-85 (1983).

About the Authors: Patrick D. Kinney was a guest worker at NIST while a graduate student in Mechanical Engineering at the University of Minnesota and is currently employed at SAES Pure Gas Inc., San Luis Obispo, CA. David Y. H. Pui is an Associate Professor in Mechanical Engineering and is a member of the University of Minnesota Particle Technology Laboratory, Minneapolis, MN. George W. Mulholland is a research chemist and Nelson P. Bryner a chemical engineer in the Fire Measurement and Research Division of the NIST Building and Fire Research Laboratory.

Volume 96, Number 2, March-April 1991
Journal of Research of the National Institute of Standards and Technology

[J. Res. Natl. Inst. Stand. Technol. 96, 177 (1991)]

A Multiple Variable-Angle Light Scattering Detector for Gel Permeation Chromatography

Volume 96 | Number 2 | March-April 1991

Peter H. Verdier

National Institute of Standards and Technology,
Gaithersburg, MD 20899

A light scattering detector has been designed and constructed for use with gel permeation chromatographs. The detector measures light scattered from the eluting sample simultaneously at nine scattering angles, and is connected to a computer-controlled display which exhibits the angular dependence of the scattering in real time while the sample is eluting. Use of the light-scattering detector in conjunction with the usual concentration-sensitive detector allows the direct determination of molecular weight as a function of elution volume, thereby making the chromatographic system "self-calibrating." Tests of the system with a series of linear and branched polystyrenes suggest that it will be a useful tool for the study and characterization of branched polymers.

Key words: branched polymers; chain branching; gel permeation chromatography; light scattering; polymer chain branching; polymer molecular weight; size exclusion chromatography; star polymers; star-branched polymers.

Accepted: February 7, 1991

1. Introduction

Gel permeation chromatography (hereafter GPC; also referred to as size exclusion chromatography, or SEC) is very widely used to estimate molecular weight distribution (MWD) of polymeric materials in solution [1]. However, GPC by itself is merely a chromatographic separation technique, not an absolute method for determining MWD. Therefore, its use for the quantitative estimation of MWD requires either calibrating the chromatographic columns with samples of known molecular weight for each kind of polymer to be studied, or the use of simplifying assumptions, such as the "universal calibration" hypothesis [2], regarding the nature of the chromatographic separation process. However, the addition of a second detector, sensitive to molecular weight, in addition to the usual detector sensitive to concentration, can in principle allow the direct determination of MWD without the need for either calibrants or the aforesaid simplifying assumptions. Detectors have been constructed for this purpose which measure solution viscosity [3] and light scattering [4–10]; some are available commercially. In this paper we report the design, construction and testing of a detector which measures the light scattered over a range of scattering angles by the GPC effluent. The range of scattering angles over which data are taken is adjustable. Extrapolation to zero scattering angle and zero concentration allows determination of the molecular weight of the effluent at each point in the chromatogram, leading to direct determination of the MWD. We demonstrate this "self-calibration" with a series of linear polystyrenes. In addition, we report the results of preliminary studies of a series of star-branched polystyrenes. These studies suggest that this instrument will be a useful tool for the study of branched polymer systems.

2. Instrumental Design

The determination of molecular weight by measuring the scattering of light from dilute solution as a function of scattering angle and solution concentration is a well-established technique [11]. In the present application, the requirements of small sample volume for the flowing GPC effluent and the ability to measure scattering simultaneously at several well-defined scattering angles place severe constraints upon the design of the light-scattering detector cell. The design employed in this instrument is shown schematically in figure 1. The cell body is made from a brass block 6.25 cm long. A 1 mm diameter hole is drilled the length of the block, with its center 2 mm from one face as shown in figure 1. Both the incident light and the flowing sample pass along this hole. A milled slot 1 mm wide and 12 mm long meets this hole, allowing a path for scattered light to exit the cell. Incident light enters the cell, and scattered light leaves it, through quartz windows clamped to cover the upstream end of the 1 mm hole and the exit slot, respectively. Unscattered light is removed by a piece of absorbing glass clamped over the downstream end of the 1 mm hole. The two windows and the absorbing glass are sealed by gaskets cut from PTFE film 0.025 mm thick. The part of the exit window which covers the exit slot is covered by an opaque evaporated Cu film except for a slit 2 mm wide, through which scattered light leaves the cell. The inside surfaces of the cell and the evaporated Cu film are blackened chemically with commercial blackening agents [12].[1] The sample solution enters and leaves the cell through a pair of stainless steel tubes of 0.5 mm i.d. These tubes are silver brazed into holes drilled into the cell body from above at an angle of 30° from vertical, which meet the 1 mm hole just inside the entrance window and exit absorber.

The cell assembly shown schematically in figure 1 is immersed in a paraffin oil bath. The bath vat is made of 100 mm o.d. glass tubing to which a flat glass bottom is fused. A flat face 1 cm wide is ground and polished on the outside of the vat at the entrance of the incident light beam. The cell assembly is positioned in the vat with the exit slit ("F" in fig. 1) centered on the center axis of the vat. Thus the incident light does not travel along a diameter of the vat, but rather travels parallel to and 2 mm away from a diameter. The scattered light is detected by nine photomultiplier tubes positioned on a turret at 15° intervals. The turret can be rotated to vary the 120° range covered by the nine photomultipliers. The angular acceptance and scattering volume are defined by the width of the exit slit, the height of the incident light beam in the sample, and a 3.2 mm diameter circular aperture in front of each detector, at a distance of about 11.5 cm from the exit slit [13].

The incident light beam, of 633 nm wavelength, is obtained from a 5 mW He-Ne laser, and is linearly polarized with the E-vector perpendicular to the plane of the incident and scattered beams (so-called vertical polarization). A pellicle beamsplitter directs a small fraction of the incident light through an absorbing glass filter to a reference photomultiplier for monitoring. A simple biconvex lens of 30 cm focal length reduces the incident beam diameter to about 0.4 mm at the sample cell. The laser, scattering cell vat, and photomultipliers are all enclosed in a light-tight box. An electrically operated shutter at the laser exit window allows detector dark currents to be measured without turning off the laser.

The light-scattering detector cell is inserted in an otherwise conventional GPC system, employing a fixed-volume loop for sample injection upstream of the chromatographic columns, and a detector which senses changes in refractive index (RI). A second, large (2 mL) injection loop between the chromatographic columns and the detectors facilitates calibration measurements as described in the following section. The light-scattering cell is inserted between this injection loop and the RI detector, since the latter is extremely sensitive to even the small back pressure that would be produced by the cell and its connecting tubing if they were connected downstream of it. The stainless steel tubing between the two detectors is kept as short as possible to minimize the volume and consequent time delay between signals from the two detectors. The signals from the scattering and reference photomultipliers, which are operated in current mode rather than photon counting mode, are sent through current-to-voltage converters and amplifiers to a 16-channel, 12 bit A/D converter. Signals from the RI detector, temperature sensor, and sample inject signal are also sent to the A/D converter. Every 100 ms, the 13 signals are digitized by the converter and read by a dedicated minicom-

[1] Certain commercial equipment, instruments, or materials are identified in this paper to specify adequately the experimental procedure. Such identification does not imply recommendation or endorsement by the National Institute of Standards and Technology, nor does it imply that the materials or equipment identified are necessarily the best available for the purpose.

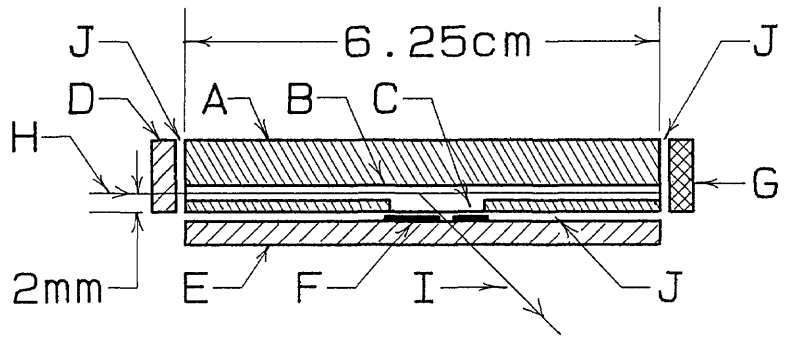

Figure 1. Schematic drawing of multiple-angle flow-through light scattering cell for GPC detector, seen from above and shown in section through the (horizontal) plane of the incident and scattered light paths. A: Cell body (brass); B: Hole, 1 mm dia. (not to scale); C: Milled slot, 1 mm high; D: Entrance window (quartz); E: Exit window (quartz); F: Exit mask with slit (evaporated Cu, thickness not to scale); G: Incident beam dump window (adsorbing glass); H: Incident light path; I: Scattered light path; J: PTFE gaskets (not shown).

puter which processes the input data, writes the results to disk, and sends the scattering data to a video display terminal which plots the angular variation of scattered intensity in real time as the chromatogram is being obtained. Data from runs at several concentrations are then re-read from disk and combined to give molecular weight as a function of elution volume, allowing calculation of the MWD and various average molecular weights.

3. Calibration

Before this instrument can be operated as a molecular-weight detector, several calibration measurements must be made. These measurements are necessary to account for the time delays between signals reaching the RI detector and the photomultipliers, to determine the solution injection volume, to establish true scattering angles inside the solution, and to convert scattering signals to Rayleigh ratios. The first two depend only upon the equipment, not upon the solvent used; the last two are solvent-dependent.

3.1 Time Delays

Although the volume of the tubing connecting the RI and light scattering detectors has been kept as small as practical, it amounts to about 150 μL, corresponding to a delay between the light-scattering detector and the RI detector of about 10 s at a typical flow rate of 1 mL/min. In addition, the geometry of the sample cell is such that a given part of the solution is "seen" by the nine photomultipliers at slightly different times. At a flow rate of 1 mL/min, the response of the photomultiplier at the largest scattering angle is effectively delayed by about $1\frac{1}{2}$ s relative to the response of the photomultiplier at the smallest scattering angle. The programs which process data from the instrument can readily allow for the relative delays between the different signals, once the delay times are known. The delays are most conveniently determined by injecting a sample between the chromatographic columns and the detectors, and observing the relative times at which the resulting signals reach the RI detectors and the photomultipliers. The time delays, which result from the system volume between the regions "seen" by the various detectors, are proportional to flow rate.

3.2 Injection Volume

In order to convert signals from the RI detector to concentrations, which are needed to calculate molecular weights from the scattering data, we need to know the sample injection volume v_0. This volume may be determined by injecting a suitable solution of concentration c_0 and integrating the resulting RI signal $s(v)$ over elution volume v. Since $s(v)$ is proportional to the concentration $c(v)$, we set $c(v)=ks(v)$, and the total mass m of solute injected can be written:

$$m = c_0 v_0 = \int c \, dv = k \int s(v) dv . \quad (1)$$

The proportionality factor k can be determined by injecting a sample of the same material at a known concentration c' (typically much less than c_0) directly into the RI detector, bypassing the chromatographic columns, and observing the resulting signal s'. Then the injection volume v_0 is given by:

$$v_0 = (c'/c_0)\int s(v)\mathrm{d}v/s' . \quad (2)$$

3.3 Scattering Angles

It will be seen from figure 1 that refraction at the solution-exit window and exit window-bath liquid interfaces will in general cause the scattered light path to be more complex than that shown in figure 1. If the bath liquid is chosen for a close index match with the exit window, then the true scattering angle θ in the solution (measured, as usual, from the direction of the incident light path) is given in terms of the externally measured scattering angle θ_e and the indices of refraction n_s and n_b of solution and bath by Snell's law, in the form:

$$n_s\cos\theta = n_b\cos\theta_e . \quad (3)$$

Thus the index of refraction of the solution must be known in order to determine the scattering angles. The difference between θ and θ_e is negligible for solutions with indices near n_b, which is about 1.5 for the paraffin oil used as the bath liquid. However, the difference can become large for measurements on samples in solvents such as tetrahydrofuran or water, with indices of 1.4 or less, when θ_e is far from $\pi/2$. (For example, for a solution of index 1.4, an external angle θ_e of 30° corresponds to a true scattering angle θ of less than 22°.)

3.4 Rayleigh Ratios

In order to convert scattering signals to the Rayleigh ratios needed for the calculation of molecular weights, the detector systems must be calibrated against a material of known Rayleigh ratio. As a practical matter, this means determining the Rayleigh ratio of the solvent as a function of scattering angle and using it as a working standard. In principle, this could be done by measuring solvent scattering as a function of scattering angle with a conventional light scattering photometer, relative to a standard of known Rayleigh ratio. In practice, however, with the present scattering cell we have been unable to prevent a certain amount of stray light, scattered from cell windows, cell walls, etc., from reaching the photomultipliers. If the amounts of stray scattering detected are constant in time and not too large, they may be determined and treated as instrumental parameters by measuring the relative scattering signals from solvent and some convenient solution both in the scattering cell and in a conventional light scattering photometer. At each scattering angle θ_i, if ϵ_i is the ratio of stray scattering to solvent scattering, then we have:

$$1 + \epsilon_i = (r_{t,i} - 1)/(r_{a,i} - 1), \quad (4)$$

where $r_{t,i}$ is the "true" ratio of solution scattering to solvent scattering at θ_i, measured with the conventional photometer, and $r_{a,i}$ is the "apparent" ratio measured with the present instrument. For the work reported here, using toluene as a solvent, the stray scattering turned out to be a few percent of solvent scattering except at the smallest scattering angle employed, where it was 23% of solvent scattering.

4. Operation

As with conventional chromatography, when maximum precision is desired, each data collection injection is preceded by a trial injection during which the instrumental gains are set so that the maximum signal from each detector is close to the largest that can be digitized by the A/D converter. For this purpose, the video display terminal attached to the computer serves as a convenient 16-channel output meter, allowing gains in the photomultiplier and RI detector channels to be set as the sample is eluted.

After instrumental gains have been set, a data collection injection may be made. As with any determination of molecular weight by light scattering, dark signals, working standard signals and solvent signals must be obtained and used in conjunction with the signals from the sample solutions. (For the present instrument, as previously noted, the solvent is used as the working standard.) Prior to actual injection, therefore, a data collection run begins by recording the photomultiplier signals with the laser shutter closed. Running averages of the dark signals so obtained are calculated by the computer and displayed upon operator request at the video display terminal, together with sample standard deviations of the individual samples and of their means.

When the dark signals are deemed sufficiently precise, their collection is ended and the final averages and standard deviations are stored. The laser shutter is opened, a few seconds are allowed for the detector channels to settle down, and collection of solvent signals begins. As with the dark signals,

running averages and standard deviations are displayed when desired while the data are being collected, to aid in deciding when the solvent/working standard readings are sufficiently precise.

After the collection of solvent/working standard readings is complete, the sample is injected. A switch on the sample injection valve gives the computer a reference point for zero time/elution volume for the chromatogram. When sample elution from the columns begins, the video display terminal plots the angular dependence of the scattering, updated every few seconds, to allow continuous verification that the experiment is under control.

5. Data Treatment

As previously described, the scattering and other signals generated by the instrument are sent to a 12 bit A/D converter. Every 100 ms, the minicomputer used for data acquisition reads the converter, stores its readings in memory, and updates an internal clock reading. Before being analyzed, the input data are pre-treated by routines which can be thought of as simulating electronic filters, delay lines, etc. The pre-treated data are then sent to a video display terminal which calculates and displays the angular dependence of scattering in real time, and to a hard disk for later analysis. Finally, after the experimental data have all been obtained, the results are read back from disk, combined and analyzed to obtain molecular weight distribution and other desired quantities.

5.1 Pre-Analysis Processing

The A/D converter used in this instrument converts input signals in the range 0 to 5 V to integers in the range 0 to 4095. Input signals less than 0 V or greater than 5 V result in integer values of 0 and 4095, respectively. These values are therefore used as out-of-range indicators. In the data-collecting phases of operation, the input signals are first examined. If any are found equal to either 0 or 4095, the values in all the channels are displayed with an error message and the run is terminated. If not, the input values are compared with running minimum and maximum values for each channel, which are updated as necessary and displayed at the end of each run, as an aid to setting gains for subsequent runs. The input values I are then added into weighted running sums, by replacing each sum S by S', given by:

$$S' = (15S + I)/16, \qquad (5)$$

an operation which has the same effect as a low-pass RC filter with a time constant of 16 input readings, or 1.6 s. Finally, the filtered values are stored in arrays which compensate for the differences in the times at which a given part of the eluting liquid is sensed by each of the detectors. The arrays, one for each photomultiplier and one for the RI detector, are large enough to contain all the readings taken during the maximum time difference between photomultiplier channels, and are filled cyclically. Every 1.6 s a value is extracted from each array, with offsets in the array indices corresponding to the sensing time differences between the photomultipliers. The offset in the array of RI detector values is chosen to make the delay between the extracted RI signal and the photomultiplier signals precisely 9.6 s, or 6 samples.

5.2 Pre-Injection Data Treatment

During the collection of dark current data, the photomultiplier signals, pre-processed as previously described, are added into running sums and sums of squares. When requested by the operator, these are used to form mean values, sample standard deviations, and sample standard deviations of the mean, which are then displayed. When the operator ends the dark current collection, the final values of these quantities are calculated, displayed and written to disk for later use analysing the data.

During the collection of solvent/working standard readings, the previously-obtained mean dark currents are subtracted from each of the sampled photomultiplier signals, and the differences are divided by the reference photomultiplier signal less its mean dark current. The resulting ratios are added into running sums and sums of squares. Upon request, these are used to form and display mean values, sample standard deviations, sample standard deviations of the mean, and relative sample standard deviations of the mean. As with the dark currents, when the collection of solvent/working standard readings is finished, the final values are calculated, displayed and written to disk. In addition, the mean values are sent to the video display terminal for use in calculating and displaying the angular dependence of the scattering after sample injection.

5.3 Post-Injection Data Treatment

After the switch on the sample injection valve has informed the program that a sample has been injected, data from the photomultipliers are treated in the same way as already described for

solvent data collection, except that instead of being added into running sums and sums of squares, they are written to disk every 1.6 s, together with the RI detector data and a sample count which gives elapsed time since injection in units of 1.6 s. In addition, every 1.6 s the smoothed detector signals S are further smoothed by adding them into weighted display sums S_d, by replacing each value of S_d by S'_d, where:

$$S'_d = (3S_d + S)/4, \tag{6}$$

giving the effect of an additional low-pass RC filter with a time constant of 6.4 s. Every 6.4 s these smoothed signals are sent to the video display terminal, which calculates and displays plots of reciprocals of the differences between solution scattering and solvent scattering, corrected for stray scattering by the use of eq (4), vs $\sin^2(\theta/2)$, for scattering angles θ calculated from eq (3). The plots so displayed are used only to provide real-time assurance that sensible data are being obtained; they are not used in the final analysis of the results.

5.4 Subsequent, Post-Experiment Treatment

Each chromatogram obtained as described in the preceding sections produces one file of scattering data and RI data as functions of elution volume. At least two such chromatogram files, obtained at different solute concentrations, are needed to obtain molecular weights from the scattering data, to allow extrapolation to the zero-concentration limits. In addition, in order to obtain concentrations from the RI data, baselines must be determined and subtracted from the RI data in each file. The processing needed to convert the files produced during the chromatographic runs into calibration parameters is accomplished by a series of programs after the chromatograms have been run and the raw data files obtained.

5.4.1 Baseline Determination The stability of the chromatographic RI detector is not sufficient to allow a solvent reading to be obtained by simply averaging before a run, as is done with photomultiplier dark currents and solvent/working standard readings. Instead, the file originally written to disk is read and the RI signal plotted vs. elution volume. Up to three regions of apparent baseline are located by eye on the plot (typically, one each before and after the sample starts to elute, and optionally a third region after the "trash peaks"). The chosen regions are specified to the program, which then determines the baseline, by unweighted linear least squares, as a linear function of elution volume in the chosen regions, adds the calculated baseline to the plot of RI signal, and integrates the RI signal less baseline over a user-specified region. It then copies the portion of the input file that was selected for integration out to disk, preceded by the baseline parameters and the value of the integral, and with the time-lag between the RI detector and photomultiplier readings removed.

5.4.2 Determination of Molecular Parameters Two or more files produced as just described, containing data at two or more concentrations, are next combined to give molecular parameters as functions of elution volume. At each sampling time, the smoothed scattering signals S' in eq (5) are read in from these files for each scattering angle θ_i and concentration c_j. Let us change notation by replacing S', which was defined in eq (5), by $S(x_i,c_j)$, where $x_i = \sin^2(\theta_i/2)$. The solvent signal at θ_i is then just $S(x_i,0)$. Form the array

$$y_{ij} = c_j K_i S(x_i,0)/[S(x_i,c_j) - S(x_i,0)], \tag{7}$$

where:

$$c_j = g_j c_0 v_0 / \int g_j(v)\mathrm{d}v, \tag{8}$$

g_j is the RI detector signal less baseline,
$\int g_j(v)\mathrm{d}v$ is its integral over elution volume v,
c_0 and v_0 are the concentration and volume of sample injected, and the factor K_i is given by:

$$K_i = 4\pi^2(\mathrm{d}n/\mathrm{d}c)^2/[\lambda_0^4 N_A R_V(1+\epsilon_i)], \tag{9}$$

where:

$\mathrm{d}n/\mathrm{d}c$ is the differential refractive index of the solution,
λ_0 is the vacuum wavelength of the incident light,
N_A is Avogadro's number,
R_V is the Rayleigh ratio of the solvent/working standard for vertically polarized radiation, and
ϵ_i is the correction for stray scattering at θ_i, determined from eq (4). The values y_{ij} are then fitted by unweighted linear least squares to the form:

$$y_{ij} = P + Qx_i + Rc_j, \tag{10}$$

determining P, Q, and R.

Finally, the weight-average molecular weight M_w, mean-square radius $\langle s^2 \rangle$, and second virial coefficient A_2 are obtained as:

$$M_w = P^{-1}, \tag{11}$$

$$\langle s^2 \rangle = 3(4\pi n_s/\lambda_0)^{-2})Q/P, \tag{12}$$

$$A_2 = R/2; \tag{13}$$

these quantities are calculated, written out to disk, and sent to a plotter.

5.4.3 GPC Calibration. The file of molecular weight vs elution volume obtained for a given sample may be used to calibrate the GPC columns for that sample. Its MWD may then be calculated from concentration data vs elution volume. In this sense, the instrument is self-calibrating; only the sample to be analyzed is necessary. However, the precision of the molecular-weight data naturally falls off in the wings of the chromatogram, where sample concentrations are small. If, as is frequently the case, additional samples of the same type of polymer as the sample under study but of different molecular weights are available, calibration data may also be obtained from them. The final calibration of the columns for a given polymer may then utilize data obtained for all the available samples of that polymer, resulting in a more precise calibration than could have been obtained using data from only one sample. The procedure employed here is to fit all the available values of M_w vs v (which may, of course, be only the data for the sample being analyzed) to the form

$$\ln M_w = A + Bv \tag{14}$$

by unweighted linear least squares. The distribution $W(M)$ in molecular weight M is then given in terms of the calibration parameters A and B and the concentration data $c(v)$ for a given injection by:

$$M = \exp(A + Bv), \tag{15}$$

$$W(M) = c(v)/[c_0 v_0 B \cdot \exp(A + Bv)], \tag{16}$$

and the classical average molecular weights M_n, M_w, etc., may be obtained from the moments of $W(M)$ in the usual way.

6. Results

As a test, the instrument was tried out on two series of polystyrenes in toluene at room temperature. The first was a series of linear polystyrenes, the second a series of star-branched polystyrenes. For this preliminary study, only the molecular-weight data were analyzed; mean-square radius and second virial coefficient are subjects for future work.

6.1 Linear Polystyrenes

Four linear polystyrene Standard Reference Materials (SRMs) [14] were used for initial tests of the performance of the detector. Their molecular-weight characteristics are summarized in table 1. SRMs 1478, 705, and 1479 are anionically polymerized materials, with relatively narrow MWDs and with M_w's of approximately 4×10^4, 2×10^5, and 1×10^6, respectively. SRM 706 is a thermally polymerized material, with a relatively broad MWD and an M_w of about 3×10^5. The chromatograms of these four linear polystyrenes, shown in figures 2 through 5, are obtained from the RI detector signal [15]. They exhibit the single, narrow peaks expected for the anionically polymerized materials, and a much broader peak for SRM 706.

Table 1. Linear polystyrenes used for tests of the light scattering detector

No.[a]	Width of MWD	Weight-average molecular weight, M_w, g/mol
705	Narrow	2×10^5
706	Broad	3×10^5
1478	Narrow	4×10^4
1479	Narrow	1×10^6

[a] Standard Reference Material No. [14].

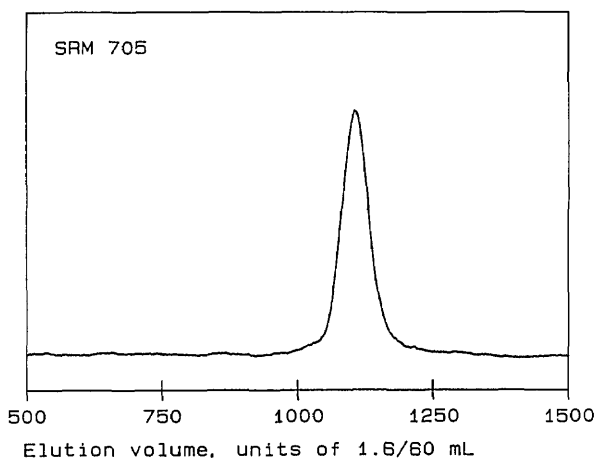

Figure 2. Chromatogram of polystyrene Standard Reference Material 705. The ordinate is a linear function of solution concentration in arbitrary units; the abscissa is elution volume in units of 1.6/60 mL.

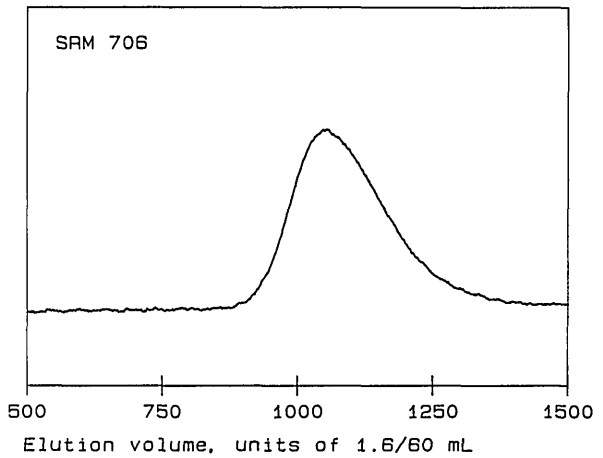

Figure 3. Chromatogram of polystyrene Standard Reference Material 706. The ordinate is a linear function of solution concentration in arbitrary units; the abscissa is elution volume in units of 1.6/60 mL.

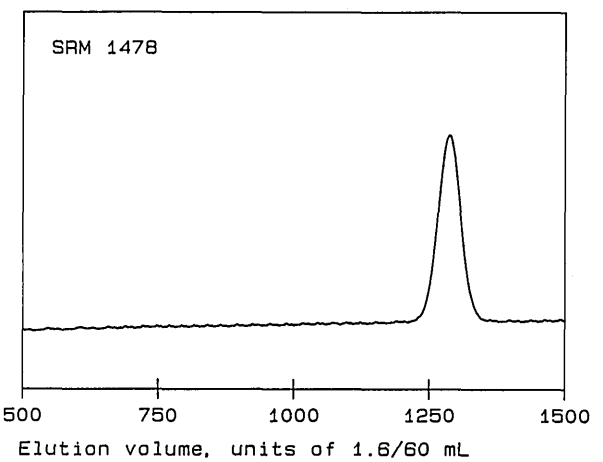

Figure 4. Chromatogram of polystyrene Standard Reference Material 1478. The ordinate is a linear function of solution concentration in arbitrary units; the abscissa is elution volume in units of 1.6/60 mL.

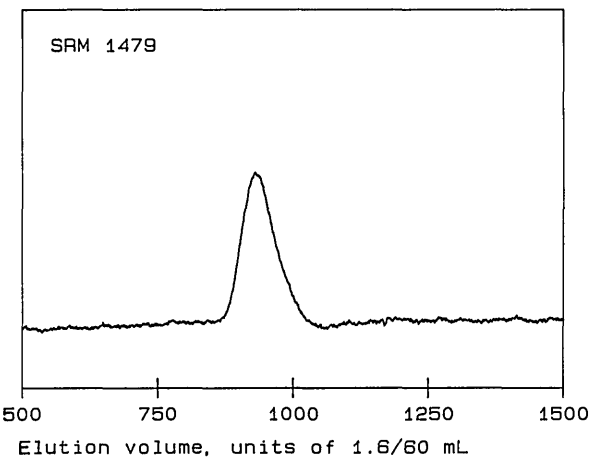

Figure 5. Chromatogram of polystyrene Standard Reference Material 1479. The ordinate is a linear function of solution concentration in arbitrary units; the abscissa is elution volume in units of 1.6/60 mL.

Plots of molecular weight vs elution volume for these linear polystyrenes, obtained from the light scattering detector and RI detector signals as described in the preceding section, are shown in figure 6. To obtain these molecular weights, using eqs (7–11), the Rayleigh ratio R_V of toluene was taken [16] as 14.0×10^{-6} cm^{-1}, a nominal value [17] of 0.11 mL/g was used for the differential refractive index of polystyrene in toluene at a wavelength of 633 nm, and the sample injection loop volume was taken to be the vendor's nominal value. Also shown in figure 6 is the straight line obtained by fitting the logarithm of molecular weight for all four samples to a linear function of elution volume by unweighted linear least squares.

It will be seen from figure 6 that the data for SRMs 706, 1478, and 1479 do indeed appear to establish a calibration of the chromatographic columns for linear polystyrene. (The large variation in the molecular weights obtained for SRM 1478 is presumably a consequence of the relatively small scattering strength of this rather low molecular-weight material.) In contrast, the data for this sample of SRM 705 lie almost entirely above the calibration line, touching it only in a short region near the lowest molecular weights for which there are data. However, comparison of figures 2 and 6 shows that the molecular-weight curve for SRM 705 lies close to the calibration line in the region where the peak of the chromatogram occurs. A curve lying above the calibration for linear material would be expected if the sample contains branched components, which have smaller dimensions than linear chains of the same molecular weight, and which therefore leave the chromatographic col-

umns at larger elution volumes. Thus it appears that most of the material in SRM 705 is linear, but there may be small amounts of branched material in the high molecularl-weight tail of its MWD. The presence of star-branched components in SRM 705, due possibly to side reactions having occurred during chain termination, has occasionally been suggested.

The sample of SRM 705 used in the foregoing analysis had been stored in our laboratory for many years, with no special attention to storage conditions. A second series of runs was carried out using another sample of the same material which had been stored in different rooms under slightly different conditions. The results for the two samples are compared in figure 7. It will be seen that they

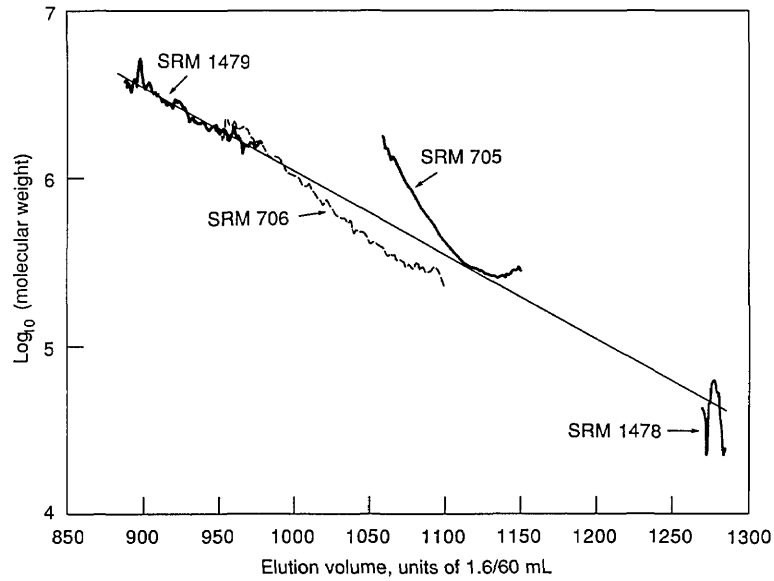

Figure 6. Semilog plots of molecular weights of four linear polystyrenes, SRMs 705, 706, 1478, and 1479, vs elution volume in units of 1.6/60 mL. Also shown is the straight line resulting from an unweighted linear least-squares fit of the logarithm of molecular weight to elution volume.

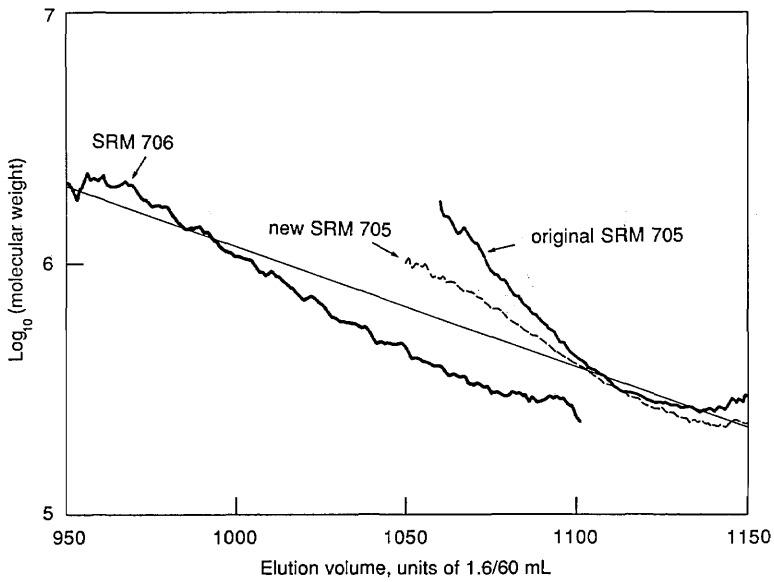

Figure 7. Semilog plots of molecular weights of original and new samples of polystyrene SRM 705, and the original sample of SRM 706, vs elution volume in units of 1.6/60 mL.

are in close agreement in the elution volume range containing most of the material, but differ in the high molecular-weight tail, where the second sample shows considerably less evidence of branching than does the original sample. Replicate measurements on a single sample reproduced these features. These findings, if confirmed by further studies, suggest that the instrument may well be useful for investigating subtle structural variations in studies of polymer aging and similar phenomena.

Finally, comparison of figure 6 with the data in table 1 shows that the molecular weights obtained for all the samples are consistently higher than the values obtained by conventional methods. The present study was carried out primarily to demonstrate the utility of the instrument for obtaining qualitative information about molecular weight distributions, and the steps needed to obtain absolute accuracy were not taken. In particular, the sample injection volume, which according to eqs (7–11) is inversely proportional to the calculated value of molecular weight, was not determined, but instead was taken equal to the nominal volume of the injection loop. This value could easily be in error by 20%, leading to corresponding errors of the same size in the calculation of molecular weights. However, careful determination of injection volume and the other calibration parameters in future studies should lead to molecular weights as accurate as those obtained by conventional light-scattering methods.

6.2 Star-Branched Polystyrenes

Three commercially available star-branched polystyrenes were studied. These materials, obtained from Polysciences, Inc. [18], are listed by the vendor as "Star Shaped Polystyrene"; their stated properties are shown in table 2. Their chromatograms are shown in figure 8; all three are bimodal. Figure 9 is a replotting of the molecular weight vs elution volume data shown in figures 6 and 7, with the results for the star-shaped polystyrenes added. The straight line also shown in figure 9 is the calibration obtained using linear polystyrene samples 706, 1478, and 1479. (Sample 705 was omitted from this calibration because of doubts about its linearity, as previously discussed.) For star-branched samples 18143 and 18145, sufficiently large scattering signals for molecular-weight calculations could only be obtained for the components corresponding to the lower elution-volume peaks. For star-branched sample 18144, however, molecular-weight data were obtained for both components, as shown in figure 9.

Table 2. Vendor-supplied characteristics of star-branched polystyrenes used for tests of the light scattering detector

No.[a]	Molecular weight	Arm M_n	No. of arms
18143	90,200	7,000	12
18144	367,300	59,200	6
18145	852,800	116,700	6

[a] Vendor's catalog No. [18].

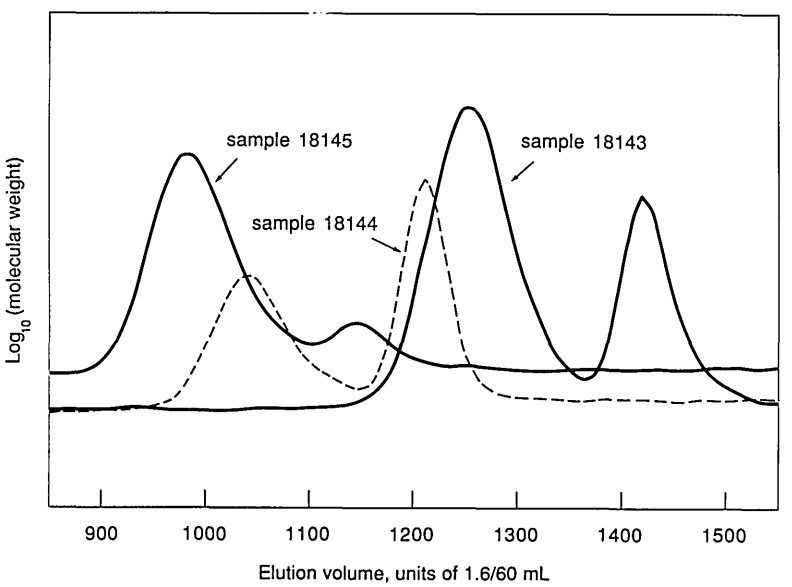

Figure 8. Chromatograms of three star-branched polystyrenes used for tests of the light scattering detector. The ordinate is a linear function of solution concentration in arbitrary units; the abscissa is elution volume in units of 1.6/60 mL.

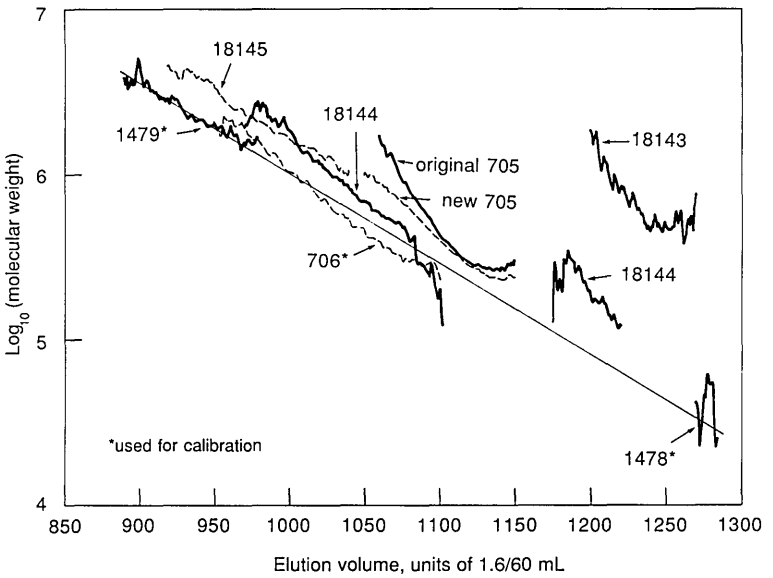

Figure 9. Semilog plots of molecular weights of linear [14] and star-branched [18] polystyrenes vs elution volume in units of 1.6/60 mL. Also shown is the straight line resulting from an unweighted linear least-squares fit of the logarithm of molecular weight to elution volume, using just the three linear polystyrenes marked with asterisks.

Table 3 summarizes the molecular-weight information at chromatographic peaks given in figures 2 through 5, 8, and 9. Shown are values M_{GPC} of the *apparent* molecular weight inferred from the elution volume at the peak and the calibration curve for *linear* polystyrene, together with the values M_{LS} obtained from the light-scattering data. Also shown are values of the ratio M_{LS}/M_{GPC}, whose deviation from unity depends upon branching.

A plausible interpretation of the bimodal chromatograms obtained for the three star-branched samples might be that in each case, the peak at higher elution volume arises from unreacted linear "arm" molecules and the peak at lower elution volume arises from star molecules. Comparison of the values of "Arm M_n" in table 2 with the values of M_{GPC} in table 3 shows that the data are reasonably consistent with this supposition. However, for sample 18144, for which light-scattering data were obtained for both peaks, it is clear from figure 9 and table 3 that the higher elution-volume component of sample 18144 is not linear polystyrene. In fact, the molecular-weight values for this peak are perceptibly farther above the linear calibration curve than are the molecular-weight values for the lower elution-volume component of this sample. The molecular weights obtained for the lower elution-volume components of all three star-branched samples lie above the curve for linear molecules, as expected, and the data for the lower elution-volume component of sample 18143 lie farther above the linear curve than do those for the other two samples, consistent with this sample being more highly branched than the others, with 12 arms to their 6.

Table 3. Apparent peak molecular weights M_{GPC} inferred from peak position on the chromatogram and the column calibration curve for linear polystyrene, and peak molecular weights M_{LS} obtained with the light scattering detector, for linear and star-branched polystyrenes. Also shown are the ratios M_{LS}/M_{GPC}

Sample No.	Elution volume at peak, units of 1.6/60 mL	M_{GPC} g/mol	M_{LS} g/mol	M_{LS}/M_{GPC}
Linear polystyrene				
705	1106	3×10^5	4×10^5	1.3
706	1053	5×10^5	4×10^5	0.8
1478	1287	3×10^4	3×10^4	1.0
1479	927	3×10^6	3×10^6	1.0
Star-branched polystyrene				
18143	1252	4×10^4	5×10^5	12
	1426	5×10^3		
18144	1040	6×10^5	8×10^5	1.3
	1210	7×10^4	1.4×10^5	2.0
18145	981	1.3×10^6	2×10^6	1.5
	1142	1.7×10^5		

If we assume that the components of the star-branched samples shown in figure 9 are indeed equal-arm star molecules, we can attempt rough estimates of the numbers of arms for these materials. The most readily accessible measure of branching in our data is the ratio M_{LS}/M_{GPC}, which is the ratio of the molecular weight of the molecule of interest to the molecular weight of a *linear* molecule eluting from the chromatographic columns at the same time. Assuming universal calibration, we can write:

$$M_{LS}[\eta]_{LS}=M_{GPC}[\eta]_{GPC}, \tag{17}$$

where $[\eta]_{LS}$ and $[\eta]_{GPC}$ are intrinsic viscosities corresponding to M_{LS} and M_{GPC}, respectively. The intrinsic viscosity $[\eta]_{LS}$ is related to the intrinsic viscosity $[\eta]'$ of a linear chain of molecular weight M_{LS} by the viscosity branching index g', given by

$$g'=[\eta]_{LS}/[\eta]', \tag{18}$$

and $[\eta]_{GPC}$ and $[\eta]'$, which are both intrinsic viscosities of linear chains, are given in terms of empirical parameters K and α by the Mark-Houwink relation:

$$[\eta]_{GPC}=K(M_{GPC})^{\alpha}, \tag{19}$$

$$[\eta]'=K(M_{LS})^{\alpha}, \tag{20}$$

Substituting eqs (18–20) into (17), we obtain:

$$M_{LS}/M_{GPC}=(g')^{-1/(1+\alpha)}. \tag{21}$$

For star-branched polystyrenes in good solvents, Bauer et al. [19] have given ratios $R_V/(R_V)_a$ of equivalent radii R_V of star-branched molecules to the equivalent radii $(R_V)_a$ of their component arms, related to the values of g' by:

$$g'=[R_V/(R_V)_a]^3 f^{-(1+\alpha)}, \tag{22}$$

for stars of f arms, giving finally

$$M_{LS}/M_{GPC}=f[R_V/(R_V)_a]^{-3/(1+\alpha)}. \tag{23}$$

In order to make use of eq (23), we need to know α for polystyrene in toluene at room temperature. A review by Wagner [20] lists four values of α for polystyrene in toluene at 25 °C ranging from 0.71 to 0.75, with a mean of 0.73. Using this value, eq (23) becomes:

$$M_{LS}/M_{GPC}=f[R_V/(R_V)_a]^{-3/1.73}$$

$$=f[R_V/(R_V)_a]^{-1.73}. \tag{24}$$

For $f=6$ and $f=12$, Bauer et al. [19] give values of 2.33 and 2.93, respectively, for $R_V/(R_V)_a$, giving values of 1.4 and 1.9 for the ratios M_{LS}/M_{GPC}. The ratios obtained for the lower elution-volume components of star-branched samples 18144 and 18145 are seen to be roughly consistent with the calculated value of 1.4 for 6-armed stars. However, the higher elution-volume component of sample 18144 has a value close to that calculated for a 12-arm star, rather than the value of unity for a linear chain. Bauer et al. do not give ratios for polystyrene stars for values of f greater than 12. However, for polyisoprene stars, which have values of $R_V/(R_V)_a$ almost identical with those for polystyrene stars at the f-values for which data for both are available, they report values of $R_V/(R_V)_a$ for f-values up to 56.2, for which they obtain $R_V/(R_V)_a=4.50$. At this f-value, eq (23) gives a value of only 4.1 for M_{LS}/M_{GPC}, nowhere near the value of 12 found for the lower elution-volume component of sample 18143. Thus this component appears to have a structure considerably more compact than that of a simple equal-armed star.

7. Conclusion

Despite the crudeness of these preliminary results, it seems clear that the multiple-angle light scattering detector can be a powerful tool for the study of branched systems. Used in conjunction with other detectors in gel permeation chromatography, it should also serve as a valuable aid in the study of copolymer and other complex systems. Improvements in instrumental sensitivity will also allow direct determination of molecular size and interactions in solution via eqs (12) and (13).

8. Acknowledgments

It is a pleasure to acknowledge helpful discussions with and assistance from many members of the Polymers Division, especially B. J. Bauer, C. M. Guttman, C. C. Han, F. I. Mopsik, H. L. Wagner, and F. W. Wang.

9. References

[1] See, for example, Yau, W. W., Kirkland, J. J., and Bly, D. D., Modern Size-Exclusion Liquid Chromatography, John Wiley & Sons, New York (1979), Glöckner, G., Polymer Characterization by Liquid Chromatography, Elsevier, Amsterdam (1987), Hunt, B. J., and Holding, S. R., Size Exclusion Chromatography, Chapman and Hall, New York (1989).

[2] Grubisic, Z., Rempp, P., and Benoit, H. J., Polym. Sci. B **5**, 753 (1967).
[3] Ouano, A. C., J. Polymer Sci. A-1 **10**, 2169 (1972).
[4] Kaye, W., and Havlik, A. J., Appl. Opt. **12**, 541 (1973).
[5] Kaye, W., Anal. Chem. **45**, 221A (1973).
[6] Ouano, A. C., and Kaye, W., J. Polym. Sci. A-1 **12**, 1151 (1974).
[7] Ouano, A. C., J. Chromatogr. **118**, 303 (1976).
[8] Ouano, A. C., J. Colloid Interface Sci. **63**, 275 (1978).
[9] Kato, T., Kanda, A., Takahashi, A., Noda, I., Maki, S., and Nagasawa, M., Polymer J. **11**, 575 (1979).
[10] Beltzung, L., and Strazielle, C., Makromol. Chem. **185**, 1145, 1155 (1984).
[11] See, for example, Yamakawa, H., Modern Theory of Polymer Solutions, Harper & Roe, New York (1971).
[12] Enthone, Inc., West Haven, CT 06508.
[13] A fixed slit of this sort, giving a scattering volume nearly independent of scattering angle, was proposed and used long ago, Harpst, J. A., Krasna, A. I., and Zimm, B. H., Biopolymers **6**, 585 (1968).
[14] Office of Standard Reference Materials, National Institute of Standards and Technology, Gaithersburg, MD 20899.
[15] The unit of 1.6/60 mL in which elution volume is expressed in this and subsequent figures is the interval between the writing of successive samples to disk (1.6 s at a flow rate of 1 mL/min).
[16] Kaye, W., and McDaniel, J. B., Appl. Opt. **13**, 1934 (1974).
[17] Han, C. C., private communication.
[18] Polysciences, Inc., Warrenton, PA 18976.
[19] Bauer, B. J., Fetters, L. J., Graessley, W. W., Hadjichristidis, N., and Quack, G. F., Macromol. **22**, 2337 (1989).
[20] Wagner, H. L., J. Phys. Chem. Ref. Data **14**, 1101 (1985).

About the author: *Peter H. Verdier is a research chemist in the Polymers Division of the NIST Materials Science and Engineering Laboratory.*

Volume 96, Number 2, March-April 1991
Journal of Research of the National Institute of Standards and Technology

[J. Res. Natl. Inst. Stand. Technol. 96, 191 (1991)]

Proposed New Electrolytic Conductivity Primary Standards for KCl Solutions

Volume 96 Number 2 March-April 1991

Y. C. Wu, W. F. Koch, and K. W. Pratt

National Institute of Standards and Technology,
Gaithersburg, MD 20899

An absolute determination of aqueous electrolytic conductivity has been made for 0.01 molal (m) and 0.1 m potassium chloride solutions, over the temperature range of 0 to 50 °C in 5 degree intervals. A cell with a removable center section of accurately known length and area was used for the measurements. Values were adjusted to be in conformity with the ITS-90 temperature scale. The overall uncertainty over the entire temperature range is estimated to be 0.03%. Values at 25 °C for 0.01 and 0.1 m are 0.00140823 and 0.0128246 S/cm, respectively. It is proposed that these values be adopted as primary standards for aqueous electrolytic conductivity, replacing the demal scale.

Key words: cell constant; conductance; demal; electrolytic conductivity; molal; potassium chloride; primary standards; resistance; specific conductance.

Accepted: December 20, 1990

1. Introduction

Parker and Parker [1] introduced the unit of "demal" to denote the concentration scale for electrolytic conductivity standards some 60 years ago. Since then the electrolytic conductivities (specific conductances) for that unit have been subjected to two major revisions. One was by Jones and Bradshaw [2] about 10 years later, and the other was based on recalculations [3,4,5] due to changes in basic constants and measurement scales, such as the international ohm to absolute ohm, and the temperature scale from the International Practical Temperature Scale, IPTS-48, to IPTS-68. Now a new International Temperature Scale (ITS-90) has been adopted as of January 1, 1990 [6]. Hence, the old values for the conductivity standards have to be revised again.

In 1987, we reviewed the primary and secondary conductivity standards [3] and stated that "although these changes have affected the values of standards to 0.1% or less, this is significantly greater than the claimed accuracy of the original measurements. Moreover, the 'demal' unit is not a customary unit of concentration in solution chemistry, and 50 years is a long time for any given standard to go without remeasurement and verification." For these reasons, we redetermined the primary standards in 1989, based on a conductance cell with a well-defined geometry whose dimensions were accurately measured, and concluded that ... future adoption of the molality scale as the basis for the primary standards for specific conductance would be desirable when data for other molalities and temperatures are available [7].

We have recently completed measurements of the conductivities of two aqueous solutions of KCl, based on the molal (m) scale, having broad application, viz., 0.01 and 0.1 m. Measurements were made from 0 to 50 °C at 5 °C intervals. For a better documentation of this determination we shall redescribe the cell construction, the apparatus, and the procedures of measurements [7,8].

2. The Design of the Conductance Cell

2.1 The Principle

The electrolytic conductivity (specific conductance), κ, of a given material is the reciprocal of ρ, the resistivity. By definition

$$R = \rho(l/A) \tag{1}$$

where R is the resistance, l is the length and A is the cross sectional area of the given material. Thus, if l/A is already known for a measured R, ρ and $1/\kappa$ are determined. Since the cell constant in a Jones-type conductance cell is determined by the lines of force between the two electrodes, the center section of the tube can be removed in order to shorten the distance between the electrodes, thereby reducing the resistance. Subsequently, the same section can be put back, lengthening the distance and increasing the resistance, provided that the lines of force are not disturbed. The difference in resistance is due to the geometry of the displacement of the center tube and the resistivity (or electrolytic conductivity) of the solution in question. If the geometry of the tube, l/A, and the difference in resistance are known, the electrolytic conductivity can be determined, independent of any reference material; ergo, it is an absolute determination. This principle can be expressed as follows:

$$R_N = \rho G_N \tag{2}$$

$$R_W = \rho(G_N + l/A) = \rho G_W \tag{3}$$

$$R_W - R_N = \rho l/A \tag{4}$$

$$1/\rho \equiv \kappa = l/A\,(R_W - R_N) \tag{5}$$

where G_N and G_W are the cell constants of the cell without and with the center tube, respectively; l/A is the length-to-cross sectional area of the center tube, called the cell constant, G_T; and R_N and R_W are the measured resistances for the cell without and with the center tube, respectively. It should be noted that κ, the electrolytic conductivity of the given solution, includes the contribution of the solvent.

2.2 The Construction of the Cell

In order to insert the center tube into the cell, the cell must be cut into two halves, which can be connected together with or without the center tube. When they are connected together, the inside diameter of the joint or joints must be streamlined and there must be no leakage.

To meet these requirements, a length of precision-bore 1-cm I.D. Pyrex[1] tubing, with uniformity certified by the manufacturer, was cut into three sections. A prefabricated flange with an I.D. of 1.3 cm, O.D. of 2.5 cm and thickness of 0.65 cm was epoxied onto each of the tubes such that the face of the flange was flush with the cut end of the tube. Then, each flanged end was ground to optical flatness. The unflanged end of each of the singly flanged tubes was joined to the corresponding electrode chamber, each of which contained a 2 cm (diameter) platinum disk electrode. The electrodes were gold soldered to a 2 mm platinum wire that extended through a graded-glass seal. The component parts of the cell are shown schematically in figure 1.

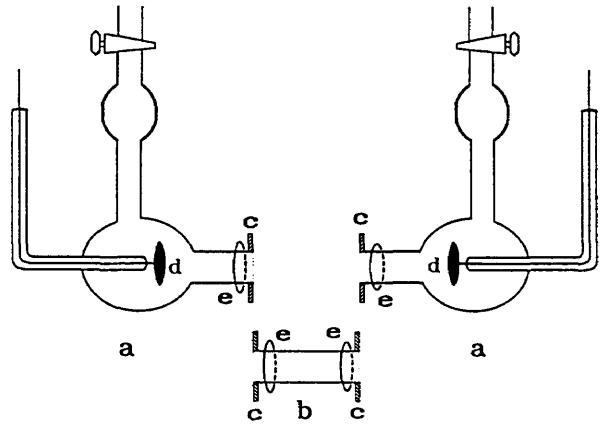

Figure 1. Component parts of the cell. a, half cells; b, center tube; c, flanges; d, platinum electrodes; e, o-rings.

To assemble the cell, the mating flange ends were held together by a C-shaped Bakelite band which could be slightly enlarged with a little pressure, such that the two flanges fit snugly into it. In this way the flanges were prevented from moving laterally. Lateral and rotational movements were

[1] Certain commercial equipment, instruments, or materials are identified in this paper to specify adequately the experimental procedure. Such identification does not imply recommendation or endorsement by the National Institute of Standards and Technology, nor does it imply that the materials or equipment identified are necessarily the best available for the purpose.

prevented by a Bakelite two-plate assembly tightened together with four nylon screws and nuts. A rubber O-ring was inserted between each plate and the rear side of the flange. This assembly is shown schematically in figure 2. The whole cell assembly with holder is shown in figure 3.

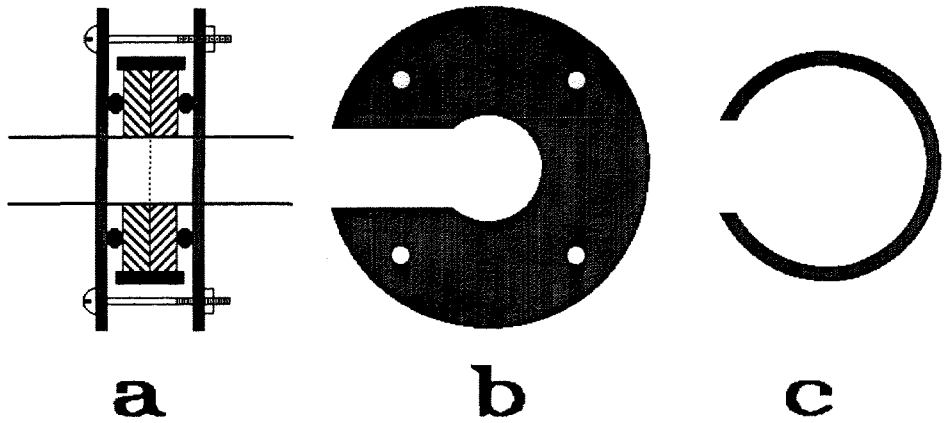

Figure 2. Detail of the flange assembly. a, overall cross section; b, side view of holder; c, side view of c-ring.

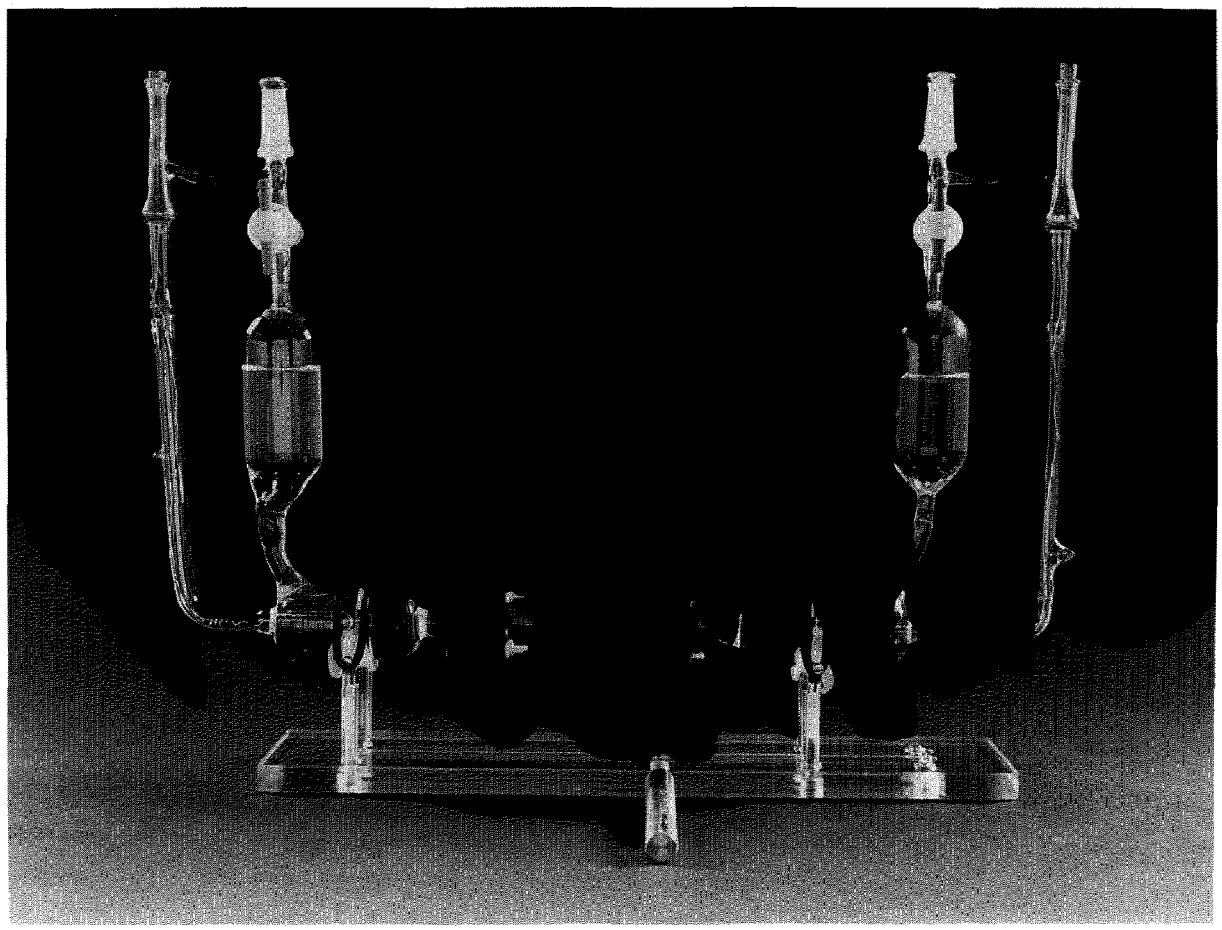

Figure 3. Photograph of cell assembly with holder.

2.3 The Determination of the Cell Constant

From eq (5), the electrolytic conductivity is determined from the cell constant, $G_T \equiv l/A$, of the center tube. For the cell used in this work, the length l and the I.D. of the center tube were determined by the Length and Mass Division of the National Institute of Standards and Technology. The reported mean values are as follows:

$l = 8.00046 \pm 0.00019$ cm,

$D = 1.00634 \pm 0.00005$ cm,

$A = 0.79539 \pm 0.00008$ cm^2.

Thus

$$G_T = l/A = 10.0585 \pm 0.0013 \text{ cm}^{-1} .$$

The relative value of the uncertainty in l indicates that the two flanges on the tube are not exactly parallel; the axes of the tubes are off by a maximum of 0.02 degree, which is established by the limit of accuracy of the instruments used to fabricate the cell.

2.4 Temperature Effect on Cell Constant

The cell constant is defined as the effective length between the two electrodes over the effective area of the electrodes, l/A. In a Jones-type of cell, the effective l/A is controlled by the size of the center tube, according to eq (5). The conductance is exactly determined by the removable section of the center tube, i.e., G_T. The temperature effect on G_T can be expressed [9] as

$$\frac{1}{G_T}\frac{dG_T}{dt} \approx \frac{1}{l}\frac{dl}{dt} - \frac{1}{A}\frac{dA}{dt}$$

$$= \alpha_g - 2\alpha_g = -\alpha_g \qquad (6)$$

where $\alpha_g = 3.6 \times 10^{-6}$ °C^{-1}, the thermal expansion coefficient of Pyrex glass. For platinum, $\alpha_{pt} = 9 \times 10^{-6}$ °C^{-1}. Over the whole range of experimental temperatures, i.e., 0 to 50 °C, ΔG_T is approximately 0.02%. However, G_W and G_N are not changed in the same way as in eq (6), for there is no means to determine the cell dimension of the entire cell shown in figure 3. The only way to determine the temperature effect on G_W and G_N is through eqs (2) and (3), at a series of temperatures.

2.5 Consistency

At a given temperature, each of the three cell constants, G_W, G_N, and G_T (of which only two are independent), has a fixed value which is independent of the conductivity of a solution. Thus, by eliminating κ from eqs (2) and (3), we obtain for any two solutions A and B at a given temperature t:

$$(R_W/R_N)_A = G_W/G_N = (R_W/R_N)_B \qquad (7)$$

where subscripts A and B solutions A or B. This consistency was verified for $t = 25$ °C in the previous report [7]. The same principle has been applied for each temperature in this present study.

3. Experimental

3.1 Apparatus

Three major instruments are required for these measurements: the cell, a constant temperature bath for the cell, and an ac bridge with a null detector.

The cell has been described in the preceding section. The constant-temperature bath is a rectangular, steel, open-top box surrounded by a wood cabinet with a hinged cover. The space between the five sides of the steel box and the wood cabinet, about 8 cm, is insulated with glass wool. Within the steel box, there are vertical inner walls situated about 5 cm from the sides and front of the steel box and 15 cm from the rear side, which end about 10 cm from both the top and the bottom of the box. A length of 0.635 cm (0.25 in) diameter copper tubing is looped twice around the outside of the inner walls, and leads to the outside of the wood cabinet for connection to a temperature-controlled fluid circulating system. An 8 cm diameter, 25 cm long trough is located at the bottom of the steel box and is centered on and close to a stirrer, located at the rear bottom of the steel box. This stirrer forces the bath fluid out through the trough and over the rim of the inner walls, resulting in good circulation. On the front side of the steel box, two studs are mounted to provide a support for the cell. The support is adjustable and allows the cell to be manipulated to a desirable position.

The fluid previously used for the constant temperature bath was light-weight petroleum oil [7]. It performed poorly because at low temperature its viscosity increased; air-bubbles produced by the stirrer were entrained, which caused nonuniform thermal conductivity. Temperature control degraded to ±0.02 °C. To improve the viscosity and to

avoid trapped air, a 50-50 mixture of light-weight petroleum oil and "Petroleum spirits" was used. Additional styrofoam insulation was attached to the bath enclosure. With the new fluid and insulation, the bath temperature was controlled to ±0.005 at 0 °C, ±0.001° at 25 °C, and ±0.002° at 50 °C. An ice bath was also tried for 0 °C. However, oil was drawn into the cell through the joints, due to the sudden drop in temperature (from 25 to 0 °C). Thus, all the results reported were obtained through the use of the modified constant temperature oil bath. A small circulating cryogenic bath, whose temperature was controlled to ±0.05 °C, was used to cool the oil bath.

A cooling fluid, a mixture of ethylene glycol and water, at a constant temperature of 1.5 °C below that of the experiment, was circulated by pumping through the copper coil and back into the control chamber. The heating of the oil bath was facilitated with a 250 W quartz heater (Corning) submerged into the bath. In the heater circuit, a 60 W light bulb was connected in series so that the power of the heater was reduced. The whole heating unit was connected to a proportional temperature control unit that had been modified to decrease the maximum temperature bandwidth from 0.1 to 0.03 °C. A thermistor was used as the sensor for the temperature controller. The quartz thermometer and frequency counter used as the bath temperature indicator had been calibrated with the NIST standard thermometer to the accuracy of 1 mK. The quartz thermometer was calibrated every 3 months at the beginning. After 1-1/2 years, the calibration drift rate gradually diminished. After 3 years, the calibration was stable to within 1 to 2 mK. The room temperature of the laboratory was controlled at 23.5±0.5 °C.

When the temperature controlling equipment was correctly adjusted, the temperature deviation rarely exceeded ±0.005 °C over an extended period, e.g., overnight. However, the temperature could readily be controlled to ±0.001 °C during experiments with minor adjustments of the heating rate. This is demonstrated in figure 4.

The bridge was a Jones bridge equipped with capacitance compensation specifically designed for conductance measurements [10,11]. This bridge also employed a Wagner ground to minimize the effects of stray capacitance on the accuracy of the null point. Because the bridge was relatively old, the bridge resistors were recalibrated by the Electricity Division at NIST before beginning this experiment. The overall accuracy of the bridge was within ±0.005% without correction and ±0.001% with correction, using the recalibrated values. The lead resistance for the connections from the binding posts of the bridge to the electrodes of the cell was determined separately and was 0.301 Ω. For measurements of the cell resistance, the observed values read from the bridge were corrected both for the lead resistance and for the recalibration of the bridge resistors.

Alternating current was supplied to the bridge from a signal generator. The generator was modified by floating the secondary of the output transformer to obtain an ungrounded output, which was required to make use of the Wagner ground of the Jones bridge. A single-ended (unbalanced) output was obtained from a secondary winding of the output transformer and was used as the phase reference for the detector. The applied ac voltage to the bridge was 1.2 V RMS. A differential input preamplifier, tuned amplifier and oscilloscope were used in the detector circuit. The differential input of the preamplifier maintained the balance of the Wagner ground and eliminated the need for an input transformer. The tuned amplifier was used in the bandpass mode at a Q of 10 to 50, as required, to attenuate sufficiently the second and higher harmonics at the null point. The output of the tuned amplifier and the reference signal from the signal generator were connected to the vertical and hori-

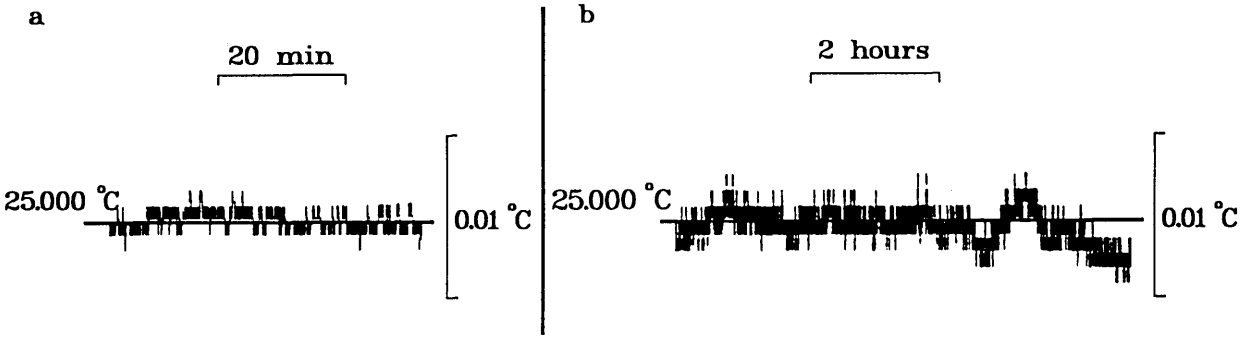

Figure 4. Temperature control of the oil bath. a, short-term (1 h) control with adjustment; b, long-term (8 h) control without adjustment.

zontal inputs of the oscilloscope, respectively. The displayed pattern on the oscilloscope was a Lissajous figure and was used to indicate simultaneously both capacitive and resistive balance of the bridge [12]. The technique was superior to using the in-phase and quadrature output meters of the lock-in amplifier to indicate resistive and capacitive balance of the bridge.

With this setup, a 0.0010% change in cell resistance was readily detected on the oscilloscope. Hence, a millidegree change in the bath temperature (0.002% in R) was easily observed, and the uncertainty in the null point measurement did not contribute significantly to the overall uncertainty of the measurement.

The frequency generator could be operated from 20 Hz to 15 kHz. The normal operating range of frequency ω was 1 to 5 kHz. The polarization effect could be corrected by extrapolating R versus ω^{-1} to $\omega = \infty$ [9].

The frequency counter for the quartz thermometer was connected to a digital-to-analog converter, the output of which was monitored using a strip chart recorder. This setup was capable of monitoring small changes in temperature (100 millidegree full-scale). Because of the thermal conductivity of the oil (bath fluid) and the path between the thermometer and the conductivity cell, there was a time lag of 2 min for the two corresponding temperatures, and a minimum of 10 min at constant temperature was required to ensure that the resistance reading is at the indicated temperature.

3.2 Material

It has been stated previously that "KCl solutions were adopted as standard because of the stability of these solutions and the ease with which KCl could be purified" [3]. The KCl used was NIST Standard Reference Material (SRM) 999. The purity of this SRM was certified at 99.99_1% based on K, and at 99.98_1% based on Cl. The fine crystalline KCl was ignited at 500 °C for 4 h and stored in a desiccator before use. A batch of SRM 999 KCl was recrystallized twice and ignited at 500 °C. No noticeable difference in conductance was observed between the original SRM 999 and the recrystallized material. The SRM 999 was thus used throughout, without recrystallization.

The in-house distilled water was passed through a deionizing column before use. When the water was freshly deionized, the electrolytic conductivity, κ, was 0.2 μS cm^{-1}; after it was stored in a polyethylene bottle for a few days, κ was equal to 1 ± 0.1 μS cm^{-1}, and was stable at 25 °C. Because of the CO_2 content in the atmosphere, it was preferable to let the solution attain equilibrium with the CO_2, rather than avoiding the CO_2.

At other temperatures, the CO_2 content was, of course, different than at 25 °C. The CO_2 equilibrium was established for each temperature after thermal cycling. The electrolytic conductivities of the water at various temperatures were determined with a cell design similar to the one used by Daggett, Blair, and Kraus [13], which had a cell constant of 0.055302 cm^{-1} at 25 °C. The deviation at any given temperature was about ± 1%, which was less than 0.02 μS/cm, far beyond the uncertainty of experimental results for the electrolytic conductivities of the standard KCl solutions.

Two kg each of 0.01 and 0.1 m (mol/kg$_{H_2O}$) KCl solution were prepared. All solution weights were corrected to vacuum. The solutions were stored in polyethylene bottles for a few days to reach equilibrium with atmospheric CO_2 before use.

3.3 Procedure

When the cell was first made, it was cleaned with chromic acid cleaning solution, washed with water, soaked in a water bath overnight, and then vacuum dried at room temperature. If the water washing, soaking and vacuum drying did not remove the trace of adsorbed chromate, the process was repeated. Although the use of chromic acid cleaning solution is not recommended, other strong acids and organic solvents were tried without satisfaction. After the cell was clean and dry, it was assembled and filled with 0.01 m KCl solution. If no leak was detected at the flanged joints after the filled cell stood for an hour, the cell was put into the bath. It normally took about 30 to 40 min for the cell to reach thermal equilibrium after being put into the bath. The reading was then recorded. If no drift was noted for another hour, the bath was adjusted to the next temperature and the process was repeated three times. If the deviation of the results was random within ± 0.005%, the mean was taken as the final result. If the deviation showed a trend toward increasing or decreasing resistance, there were two probable causes: cell contamination or loss of water from the solution by evaporation. Cell contamination was generally caused by adsorption of foreign substance(s) on the walls and electrodes. There was no easy way out of this except to repeat the experiment until the foreign substances were leached out and the readings were constant. If the drift was due to concentration increase by evapora-

tion, a fresh solution had to be used and the experiment repeated. (The evaporation occurred while-transferring solution from the bottle to the cell, a process that was performed in the open. Since the rate of evaporation was about 3 mg per min and the transferring processes took about 2 min, a total of about 6 mg of water was lost, approximately 0.003% of the total volume. Because of this, no bottle of solution was used twice.)

The procedures for changing from one concentration to another, or for replacing the center tube in the cell, were similar. Caution was always exercised to prevent the oil on the outside of the cell from creeping inside. If this occured, the cleaning process was repeated.

The bath temperature was generally started at 25 °C, and was either raised or lowered in 5 degree steps to 50 or 0 °C, and then back to 25 °C. The resistance readings for the cycle of 25-0-25 °C were reproducible to within ±0.005%, while those for the cycle of 25-50-25 °C were not as good. The measured resistances for the reverse cycle from 50-25 °C were generally lower than the forward cycle (25 to 50 °C) due to evaporative loss of water from the cell. Hence, only those results for the forward cycle were used in the final analysis. In addition, at high temperatures (45 and 50 °C), small air bubbles would sometimes form in the chamber between electrodes, in which case higher resistance readings resulted. There was no easy way to get rid of the bubbles except to take the cell out and to rotate it. This process usually resulted in loss of water vapor, ending in lower resistance readings. It was preferable to rotate the cell while it was still in the bath, but this was only successful a third of the time. In most cases, the measurement had to be repeated when bubbles developed.

14. Results

All the values listed in the following tables were based on the measurements at the 1968 temperature scale (IPTS-68) from 0 to 50 °C in 5 degree increments. Currently, a new 1990 international temperature scale has been adopted (ITS-90) [6]. The portion of the new scale that affects our values (0 to 50 °C) can be described as

$$t_{90} - t_{68} = -2.6 \times 10^{-4} t . \tag{8}$$

The corrected values for the electrolytic conductivities are listed separately.

The observed resistances, corrected for lead resistance, are listed in table 1. Calculated cell constants, based on the development outlined in section 2, are listed in table 2. The electrolytic conductivities, κ, of 0.01 m and 0.1 m KCl solutions, and of solvent are listed in table 3.

The temperature effect can be expressed as

$$\kappa_{68} = a + bt + ct^2 + dt^3 \tag{9}$$

where a, b, c, and d are temperature coefficient constants for κ. Their values for 0.01 m and 0.1 m KCl solutions are listed in table 4.

The change of κ_{68} with respect to t is

$$\frac{d\kappa_{68}}{dt} = b + 2ct + 3dt^2 \tag{10}$$

Thus, the κ_{90} of the ITS-90 temperature scale will be

$$\kappa_{90} = \kappa_{68} + (b + 2ct + 3dt^2) \times 2.6 \times 10^{-4} t . \tag{11}$$

The values for κ_{90} are listed in table 5.

Table 1. Observed resistance values for 0.01 m and 0.1 m KCl solutions (ohm)

t °C	0.01 m R_W	0.01 m R_N	0.01 m ΔR	0.1 m R_W	0.1 m R_N	0.1 m ΔR
0	24073.1	11067.20	13005.90	2615.85	1202.97	1412.88
5	20883.7	9601.68	11282.00	2275.40	1046.22	1229.18
10	18350.7	8436.89	9913.81	2004.06	921.46	1082.60
15	16301.0	7494.65	8806.35	1784.00	820.30	963.70
18	15252.6	7012.39	8240.21	1671.20	768.26	902.94
20	14616.6	6720.06	7896.54	1603.02	737.06	865.96
25	13213.3	6075.00	7138.30	1451.86	667.59	784.27
30	12030.5	5531.43	6499.11	1324.38	608.93	715.45
35	11024.4	5069.10	5955.30	1215.70	559.02	656.68
40	10161.3	4671.80	5489.50	1122.30	515.99	606.31
45	9414.10	4328.10	5086.00	1041.47	478.82	562.65
50	8762.80	4028.90	4733.90	970.70	446.34	524.36

Table 2. Cell constants, cm^{-1}

t °C	G_W	G_N	G_T
0	18.6204	8.56110	10.0594
5	18.6202	8.56105	10.0592
10	18.6200	8.56101	10.0590
15	18.6198	8.56096	10.0589
18	18.6197	8.56093	10.0588
20	18.6196	8.56091	10.0587
25	18.6194	8.56086	10.0585
30	18.6192	8.56082	10.0583
35	18.6190	8.56077	10.0581
40	18.6188	8.56072	10.0580
45	18.6185	8.56067	10.0578
50	18.6183	8.56062	10.0576

Table 3. Electrolytic conductivities for 0.01 m and 0.1 m KCl solutions, IPTS-68 scale (S/cm, H_2O corrected)

	κ (S/cm)		
t °C	0.01 m KCl	0.1 m KCl	H_2O
0	7.72921×10^{-4}	7.11685×10^{-3}	0.58×10^{-6}
5	8.90932×10^{-4}	8.18342×10^{-3}	0.68×10^{-6}
10	1.01389×10^{-3}	9.29113×10^{-3}	0.79×10^{-6}
15	1.14135×10^{-3}	1.04362×10^{-2}	0.89×10^{-6}
18	1.21981×10^{-3}	1.11395×10^{-2}	0.95×10^{-6}
20	1.27289×10^{-3}	1.16147×10^{-2}	0.99×10^{-6}
25	1.40805×10^{-3}	1.28230×10^{-2}	1.10×10^{-6}
30	1.54641×10^{-3}	1.40573×10^{-2}	1.20×10^{-6}
35	1.68753×10^{-3}	1.53137×10^{-2}	1.30×10^{-6}
40	1.83097×10^{-3}	1.65883×10^{-2}	1.40×10^{-6}
45	1.97628×10^{-3}	1.78776×10^{-2}	1.51×10^{-6}
50	2.12305×10^{-3}	1.91775×10^{-2}	1.61×10^{-6}

Table 4. Parameters for κ of eq (9) for 0.01 m and 0.1 m KCl solutions

	0.01 m	0.1 m
a	7.72921×10^{-4}	7.11685×10^{-3}
b	2.30786×10^{-5}	2.08948×10^{-4}
c	1.07659×10^{-7}	8.98677×10^{-7}
d	-5.83639×10^{-10}	-5.06729×10^{-9}

Table 5. Electrolytic conductivities for 0.01 m and 0.1 m KCl solutions, recommended values ITS-90 scale

	μS/cm	
t °C	0.01 m	0.1 m
0	772.921	7116.85
5	890.961	8183.70
10	1013.95	9291.72
15	1141.45	10437.1
18	1219.93	11140.6
20	1273.03	11615.9
25	1408.23	12824.6
30	1546.63	14059.2
35	1687.79	15316.0
40	1831.27	16591.0
45	1976.62	17880.6
50	2123.43	19180.9

5. Discussion

Accuracy is the necessary requirement for a primary standard. There are four main factors that could affect the accuracy of these results, viz., 1) the purity, stability, and accuracy of the concentration of the KCl solutions during preparation, storage, and measurement; 2) the cell constants and the cleanliness of the cell; 3) the temperature control; and 4) the measuring instrumentation. Of these, the last one caused the least problem (<0.002%). With regard to the bath temperature, the stability and control attained were ±0.001 to ±0.002 °C, except at 50, 5, and 0 °C, where the stability degraded to ±0.003, ±0.003, and ±0.005 °C, respectively. The cell constants, G_W and G_N, were permanently changed during the initial thermal cycling from 0 to 50 °C. After this, they were stable and consistent. Most likely, this was due to the graded glass used for sealing the platinum electrodes and the joint to the Pyrex glass. It is advised that any cell used for conductivity measurement over a wide range of temperature should be subjected to the same thermal cycle before it is calibrated. Thereafter, its stability should be monitored. The uncertainty in the values for electrolytic conductivity due to the measurement and maintenance of temperature is estimated not to exceed 0.01%.

Maintaining the cleanliness of the cell was not a simple problem. During the course of lowering the cell temperature, if the change was too abrupt, such as from room temperature to 0 °C, the oil from the bath could be drawn into the cell. There was no easy way to remove the thin oil film adhering to the cell wall except to use chromic acid.

However, the chromate ions tended to adsorb to the cell. It took about two weeks to leach out these ions by repeating soaking and refilling with high-purity water. The extent to which the cell is "clean" may be the controlling factor in the random uncertainty in the measurement (see below). The uncertainty in the cell constant is estimated to be 0.02%, as discussed in section 2.3.

The accuracy of the concentration of the KCl solutions, as limited by the purity, stability, and preparation, was estimated to be within ±0.005%. The least known effects resulted from evaporation, condensation and contamination during the course of transferring solution from the stock to the cell, and thermal cycling from one temperature to another. The solutions were occasionally contaminated (perhaps by the cell) as noted by the conductance drifting upward. These random events could compromise the reproducibility to ±0.01 to 0.02%.

Therefore, the total uncertainty in the electrolytic conductivity values over the entire range of temperatures was estimated conservatively to be approximately 0.03% (determined by the root sum square method of combining uncertainties).

There were at least three determinations made for each temperature and concentration. Each of these points consisted of two independent measurements, one with the center tube in place, and the other without the center tube. The difference in resistance between the two was used to determine the electrolytic conductivity, κ, as shown in eq (5).

To ensure that the κ's obtained are consistent and accurate, eqs (2) and (3) have to be used to determine the same κ's for verification.

In section 2.5, eq (7) shows that $(R_W/R_N)_A=(R_W/R_N)_B$, which is the same as $(G_W/G_N)_A=(G_W/G_N)_B$. It will also be true that

$$G_W/G_T=R_W/\Delta R, \tag{12}$$

$$G_W=(R_W/\Delta R)G_T \tag{13}$$

and

$$G_N=(R_N/\Delta R)G_T\,. \tag{14}$$

Since

$$G_T(t)=G_T(25)\,[1-\alpha_g(t-25)], \tag{15}$$

from the ratio of the observed resistances, i.e., the ratio of G's, as a function of temperature the cell constants, G_W and G_N can be obtained by eqs (13), (14), and (15). Using eqs (2), (3), and (4), three sets of κ can be computed. They should be identical within experimental uncertainty.

It is possible, however, that both R_W and R_N may be off by some fraction, α, i.e., $\alpha R_W/\alpha R_N=R_W/R_N$. In this case, either the κ or the G's will be off by the same factor α. Statistically, we can compute the standard deviation from any one of the three elements, R, κ, and G, for they are interrelated. We selected G, because (a) it is a constant at a given temperature, (b) it is a linear function of temperature [eq (15)], (c) its change through the temperature range of 0–25 and 25 to 50 °C is small, and (d) at 25 °C we have accumulated more data to ensure its constancy.

Employing these smoothed cell constants, all the values for κ at all temperatures were recalculated and were fitted to a polynomial function of temperature with the method of least squares. The final values are shown in table 3. The differences between the observed and the smoothed values are plotted in figures 5 and 6.

Finally, a new temperature scale ITS-90 was adopted at the beginning of 1990 (after all the measurements had been done with IPTS-68 temperature scale). Therefore, the electrolytic conductivity values had to be adjusted to the new ITS-90 scale by eq (11). The adjusted values are shown in table 5. A few values at 25 and 40 °C were determined using a thermometer calibrated on the ITS-90 scale in order to validate the adjustment. These values were within 0.01% of the adjusted values. It is recommended that the electrolytic conductivity values listed in table 5 be adopted as the primary standards for electrolytic conductivity over the temperature range studied.

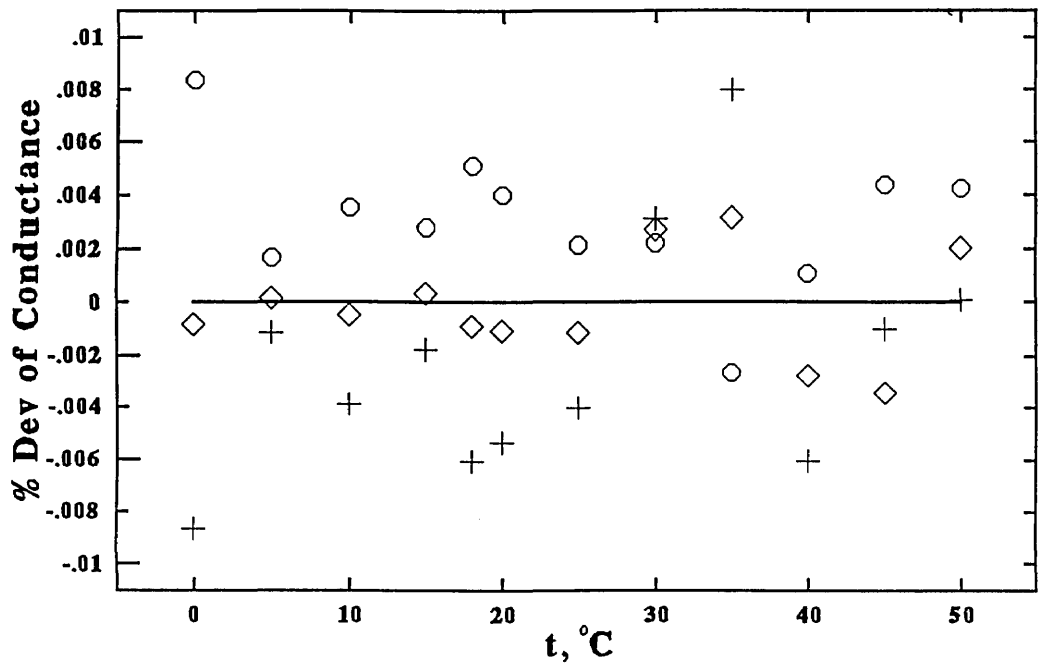

Figure 5. 0.01 *m* KCl, percent deviations of values obtained using the three different cell configurations from the smoothed values (solid line): without center tube, ○; with center tube, ◇; center tube only, +.

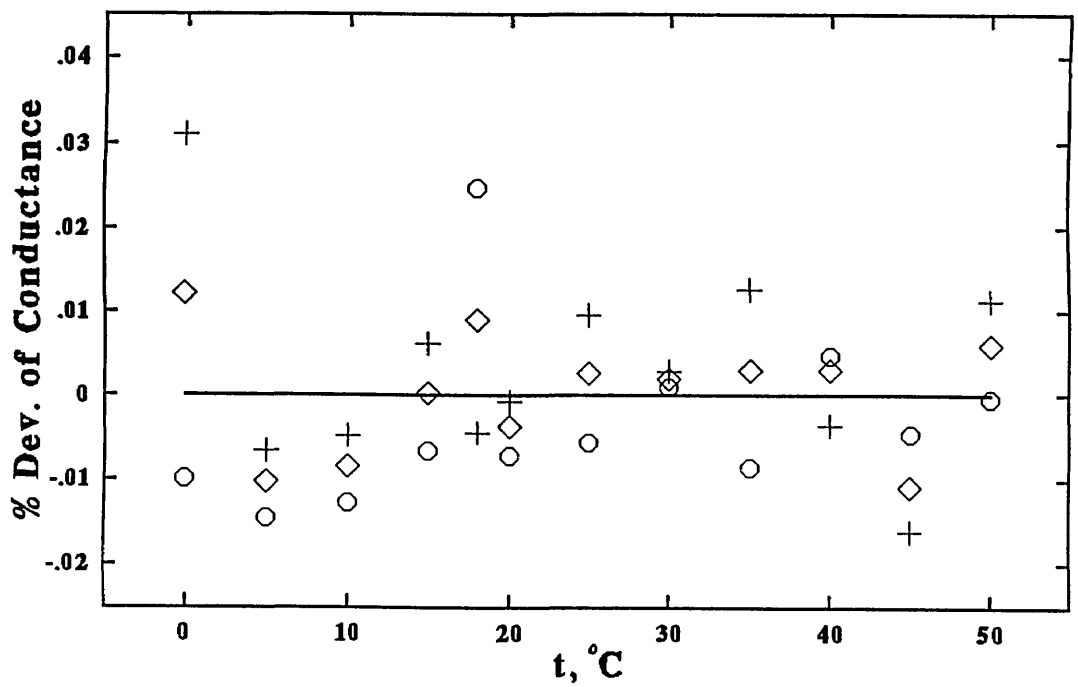

Figure 6. 0.1 *m* KCl, percent deviations of values obtained using the three different cell configurations from the smoothed values (solid line): without center tube, ○; with center tube, ◇; center tube only, +.

6. References

[1] Parker, H. C., and Parker, E. W., J. Am. Chem. Soc. **46**, 312 (1924).
[2] Jones, G., and Bradshaw, B. C., J. Am. Chem. Soc. **55**, 1780 (1933).
[3] Wu, Y. C., Koch, W. F., Hamer, W. J., and Kay, R. L., J. Solution Chem. **16**, 985 (1987).
[4] Standard Solutions Reproducing the Conductivity of Electrolytes, International Recommendation No. 56, OIML, 1st ed., June 1980, Bureau International de Metrologie Legale, Paris (1981).
[5] Jukes, E., and Marsh, K. N., Pure and Appl. Chem. **53**, 1844 (1981).
[6] Officially adopted by the Comité International des Poids et Mesures (CIPM) on Sept. 26–28, 1989, Meeting at the Bureau International des Poids et Mesures (BIPM).
[7] Wu, Y. C., Pratt, K. W., and Koch, W. F., J. Solution Chem. **18**, 515 (1989). In this reference there are two misprints on Table I: The No. 1 row, last column, should read 0.0128516, the No. 3 row, the number in parentheses should read 0.1 m.
[8] Wu, Y. C., and Koch, W. F., to be published.
[9] Robinson, R. A., and Stokes, R. H., Electrolytic Solutions, 3rd ed., Butterworths, London (1959).
[10] Jones, G., and Josephs, R. C., J. Am. Chem. Soc. **50**, 1049 (1928).
[11] Dike, P. H., Rev. Sci. Instruments **2**, 379 (1931).
[12] Lamson, H. W., Rev. Sci. Instruments **9**, 272 (1938).
[13] Daggett, H. M., Bair, E. J., and Kraus, C. A., J. Am. Chem. Soc. **73**, 799 (1951).

About the Authors: *Yung Chi Wu and Kenneth W. Pratt are senior research chemists in the Electroanalytical Research Group, Inorganic Analytical Research Division, NIST. William F. Koch is the leader of the Electroanalytical Research Group and the Deputy Chief of the Inorganic Analytical Research Division, NIST.*

Volume 96, Number 2, March–April 1991
Journal of Research of the National Institute of Standards and Technology

[J. Res. Natl. Inst. Stand. Technol. 96, 203 (1991)]

Digital Image Analysis Assisted Microradiography—Measurement of Mineral Content of Caries Lesions in Teeth

Volume 96 | Number 2 | March–April 1991

L. C. Chow, S. Takagi, W. Tung,[1] and T. H. Jordan[2]

American Dental Association Health Foundation, Paffenbarger Research Center, National Institute of Standards and Technology, Gaithersburg, MD 20899

This study investigated the feasibility of using a digital image analysis system to process the information contained in microradiographs of tooth sections that included dental caries lesions. The results show that by using an aluminum step wedge to provide a range of thickness standards and a sound area of the sample as an internal reference, data on tooth mineral content as a function of the location can be obtained with an estimated error of less than 5% relative to the mineral content of sound area. This microradiographic technique allows the response of tooth samples to a remineralization treatment to be quantitatively measured and statistically analyzed.

Key words: demineralization; dental caries; digital image analysis; microradiography; remineralization; tooth mineral.

Accepted: January 28, 1991

1. Introduction

Contact microradiography is an important and frequently used technique [1-4] for qualitative assessment of the mineral content of partially demineralized lesions in tooth enamel or root dentin. With a scanning microdensitometer connected to a computer, quantitative information on the mineral content of different regions in the lesion can also be obtained from microradiographs [5,6]. Digital image analysis systems that are capable of transforming photographic images, including those from microradiographs, into digital forms have become widely available in recent years. The digitized microradiographs can also be used to obtain quantitative information on the mineral content distribution as a function of location in the lesion [7]. The precision and sensitivity of this type of measurement are affected by numerous factors including parameters associated with the radiographic procedure, the quality of the microscope, and the characteristics of the digital image analysis system, e.g., spatial resolution, range of grey levels (brightness), etc. The present study examined the feasibility of quantitation of the mineral content in caries lesions using a digital image analysis system capable of producing 256 grey levels. Mineral contents of the lesions in extracted human root dentin were measured before and after a remineralization treatment. Several factors associated with the radiographic procedures or with the densitometric measurements that may produce significant errors in the final results were investigated. A procedure that can produce data on mineral density distribution with an estimated error of below 5% is described.

[1] Present address: Brown University, Providence, RI.

[2] Chemistry Department, Cornell College, Mt. Vernon, IA.

2. Materials[3] and Methods

2.1 Thickness Standards

As is common to all quantitative analytical procedures, it is necessary to have a set of standards of known values of the property being measured, i.e., mineral content in the present case. It can be shown [5] that under a given measurement condition, a fixed relationship exists between the radio-opacities of aluminum and enamel (or root). Thus, an aluminum step wedge was used as a set of thickness standards. These, in turn, were used as the standards for measuring the mineral content of tooth specimens. A total of four wedges were prepared by folding 15 μm thick aluminum foils (A.D. Mackay, Inc., New York, NY) such that each step in the wedge contained from 1 to 13 layers of the foil (fig. 1), yielding thicknesses ranging from 15 to 195 μm. The first eight layers of the standards were used because the radio-opacities of these standards encompassed but did not greatly exceed those of partially demineralized and intact areas of the root dentin specimens used in the present study. The overall dimension of the wedge was approximately 2 mm in width by 17 mm in length.

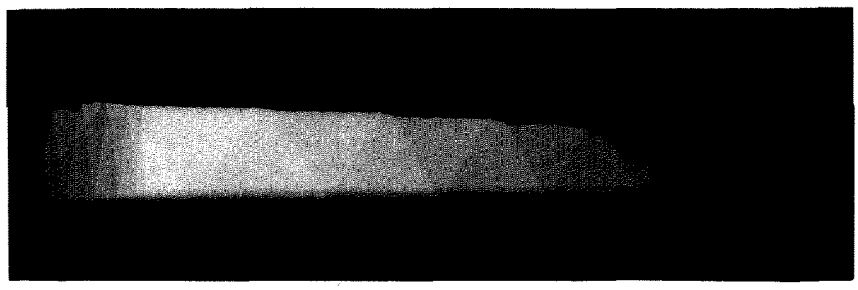

Figure 1. An aluminum step wedge used as the thickness standards.

2.2 Formation of Caries Lesions in Tooth Specimens

A pH 4 acetate-containing solution [8] was used to form caries-like lesions in the roots of human molar teeth extracted for orthodontic reasons. The demineralized root samples were sectioned longitudinally (along the length of the root) with a diamond blade (Isomet, Buehler Ltd., Lake Bluff, IL). The sections were then ground by hand on wet 600 grit sand paper (Buehler Ltd., Lake Bluff, IL) to a thickness of approximately 120 μm. Radiographs of four root dentin sections containing lesions were produced by the procedure described below.

2.3 Remineralization Treatment

Following documentation of the lesions on the radiographs, the specimens were treated with a remineralizing solution ([Ca] = 1.5 mmol/L, [P] = 1.2 mmol/L, [F] = 53 μmol/L, [HEPES] = 25 mmol/L, [KCl] = 30 mmol/L, pH = 7.4). The solution was applied to the single section specimens, each placed in a holder consisting of two tightly held microscope glass slides and a layer of parafilm between the tooth section and each slide (fig. 2). In a previous study [9] this assembly was immersed in a pH 7 methylene blue (1 wt. %) dye solution for 5 days. No penetration of the dye into the tooth-parafilm or the parafilm-glass interface was

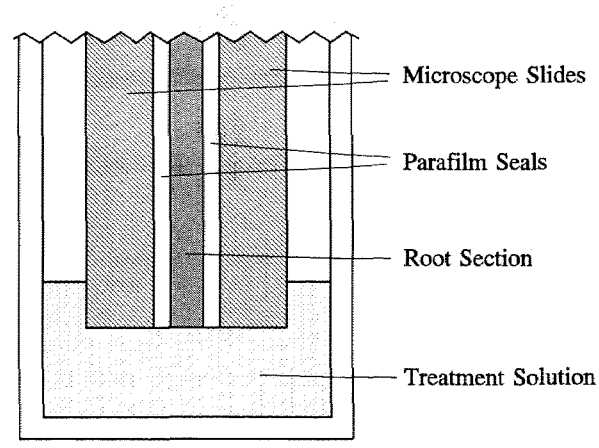

Figure 2. Schematic drawing of a thin section of tooth in a holder which protected the cut surfaces of the specimen from being exposed to the treatment solution.

[3] Certain commercial equipment, instruments, or materials are identified in this paper to specify adequately the experimental procedure. Such identification does not imply recommendation or endorsement by the National Institute of Standards and Technology or the ADA Health Foundation, nor does it imply that the materials or equipment identified are necessarily the best available for the purpose.

detected, indicating the presence of water-tight seals at the interfaces. Thus when the tooth section in the holder was immersed in the remineralizing solution, only the natural surfaces of the tooth, positioned near the lower edges of the slides, would be exposed to the solution. Tooth sections were exposed to the remineralizing solution for 5 days, and the solution was changed daily. After the remineralization treatment the specimens were removed from the holders and radiographs were again produced.

2.4 Microradiography

Contact microradiographs of the tooth specimens were obtained with Ni-filtered CuK_α radiation (Faxitron, Model 43855A, Hewlett Packard, McMinnville, OR) operating at 40 kV and 3 mA. The x-ray source to film distance was 30.5 cm. The exposure time used was 13 min, which was determined in preliminary experiments as optimum for the type of specimens used. A fine grain film (Kodak Professional film SO343, Eastman Kodak Co., Rochester, NY) designed for contact microradiography was used. The x-ray films were developed according to the procedure recommended by the manufacturers. Radiographs containing either four aluminum step wedges or several tooth sections and one step wedge were produced.

2.5 Digital Image Analysis System

A commercially available digital image analysis system (Bioquant System IV, R & M Biometrics, Inc., Nashville, TN) was interfaced to a microscope (Leitz Ortholux, Germany) and a personal computer. The image analysis system consisted of a monochrome video camera (Model 65, Mk IV Series, Dage-MTI, Inc., Michigan City, IN), a pointer device, a frame grabber card capable of storing an image containing 252×246 pixels (picture elements) with 256 grey levels, and the necessary software for video counting and microdensitometry measurements. In this setup, the maximum spatial resolution, as determined by the optical magnification of the microscope (250X) and the number of pixels included in the image, was approximately 1.10 and 1.45 μm in the horizontal and vertical directions, respectively. After the digitized images of the standards and samples were obtained, the data were processed, as described below, using additional software developed specifically for microradiographic study on tooth specimens [10,11].

2.6 Precision of Radiographic Measurements

In a typical radiograph produced for measurement of tooth mineral contents, there is a distance, usually of several millimeters, between the standards and the specimen. Variations in brightness and contrast in the radiograph over such distances can contribute to errors in the measurement. An experiment consisting of the following steps was conducted to determine the extent of variation in radio-opacity of identical objects placed at different sites of a given radiograph: (1) A microradiograph containing four aluminum step wedges was obtained under the conditions outlined above. (2) The microradiograph was placed on the microscope to which the digital image analysis system was attached, and the average grey level of each step of all the wedges was measured in triplicate. (3) For each wedge the known thicknesses (Th_k), in the unit of number of layers, were plotted against the measured grey level (GL) values, and a calibration curve was constructed by fitting the data to a first, second, or third order polynomial function (eqs (1), (2), and (3), respectively) with the least squares method.

$$Th_k = a_0 + a_1 GL \tag{1}$$

$$Th_k = a_0 + a_1 GL + a_2 GL^2 \tag{2}$$

$$Th_k = a_0 + a_1 GL + a_2 GL^2 + a_3 GL^3 \tag{3}$$

(4) Steps (1) through (3) were repeated such that data on a total of twenty different step wedge images from five radiographs were obtained. (5) For each type of regression function, the average standard error of y estimate and the correlation coefficient were computed to determine the goodness of fit (table 1). (6) One step wedge in each radiograph was randomly selected to serve as the standard, and the other three step wedges were treated as samples, each having segments of different thicknesses. (7) The measured grey level values for the "samples" were used to compute the corresponding calculated thicknesses by use of the calibration curve obtained from the "standard" of that radiograph. (8) A linear regression analysis with eq (4) was performed to determine the correlation between the calculated thicknesses (Th_c) and the known thickness (Th_k) for each aluminum wedge (table 2).

$$Th_c = b\, Th_k \tag{4}$$

Equation (4), which represents a linear model with forced zero intercept, was chosen for the reason given in section 4.

Table 1. Regression statistics of thickness of aluminum wedges vs grey level

	Polynomial Function					
	1st order		2nd order		3rd order	
Wedge	S.E.[a]	R[b]	S.E.	*R*	S.E.	*R*
A1	0.254	0.994	0.195	0.997	0.133	0.998
A2	0.164	0.997	0.133	0.998	0.126	0.998
A3	0.136	0.997	0.080	0.999	0.083	0.999
A4	0.233	0.996	0.187	0.998	0.192	0.998
B1	0.136	0.997	0.096	0.999	0.089	0.999
B2	0.090	0.998	0.090	0.998	0.070	0.999
B3	0.158	0.994	0.127	0.998	0.132	0.997
B4	0.111	0.996	0.048	0.999	0.034	0.999
C1	0.137	0.998	0.099	0.999	0.085	0.999
C2	0.257	0.992	0.182	0.996	0.190	0.989
C3	0.173	0.996	0.143	0.998	0.144	0.998
C4	0.190	0.994	0.074	0.999	0.074	0.999
D1	0.145	0.998	0.143	0.998	0.146	0.998
D2	0.108	0.999	0.101	0.999	0.070	0.999
D3	0.211	0.995	0.173	0.997	0.067	0.999
D4	0.180	0.992	0.064	0.999	0.056	0.999
E1	0.400	0.987	0.245	0.996	0.238	0.996
E2	0.354	0.990	0.200	0.997	0.196	0.997
E3	0.184	0.996	0.156	0.997	0.155	0.998
E4	0.441	0.985	0.160	0.998	0.164	0.998
Mean	0.200	0.995	0.135	0.998	0.122	0.998
S.D.	0.101	0.003	0.053	0.001	0.056	0.001

[a] S.E. = Standard error of *y* estimate.
[b] R = correlation coefficient.

Table 2. Regression statistics of measured thickness vs. known thickness of aluminum step wedges.

Radio-graph	Wedge	Slope	(S.E.[a])	Correlation coefficient	S.E. of *y* estimate
	1	0.987	(0.008)	0.997	0.157
A	2	1.294	(0.006)	0.999	0.107
	3	0.917	(0.009)	0.994	0.246
	1	1.009	(0.019)	0.989	0.245
B	2	1.063	(0.010)	0.996	0.134
	3	1.511	(0.012)	0.998	0.115
	1	0.946	(0.010)	0.995	0.201
C	2	0.987	(0.010)	0.995	0.198
	3	1.276	(0.014)	0.994	0.227
	1	1.004	(0.007)	0.997	0.143
D	2	1.086	(0.011)	0.995	0.210
	3	1.528	(0.028)	0.985	0.334
	1	0.809	(0.006)	0.996	0.216
E	2	1.046	(0.013)	0.993	0.258
	3	1.078	(0.008)	0.997	0.218
	Mean	1.103	(0.011)	0.995	0.201
	S.D.	0.202		0.003	0.059

[a] Standard error of the slope.

The conditions used for developing the radiographs and the light intensity of the microscope inevitably varied slightly from one measurement to the next. These have lead to the differences in brightness and contrast of the digitized radiographs as would generally be encountered in the measurement.

2.7 Assessment of Mineral Content

This procedure consisted of the following steps: (1) A microradiograph containing images of the tooth specimens and a step wedge was obtained. (2) The radiograph was placed under the microscope, and the average grey levels of the standards were measured in triplicate as described earlier. (3) The data were processed and a standard curve was constructed as before. (4) An image of an area of the sample approximately 277 μm high × 357 μm wide containing the lesion being studied (fig. 3) was "captured" digitally, and the grey levels of all the pixels in the image were stored in a "grey level" file in the computer. (5) The grey levels of the individual pixels stored in the file were converted to thickness values through the use of the standard curve obtained in (3), and these were stored in a "thickness" file. (6) An area, approximately 100 μm high and 25 μm wide, located in the sound portion of the specimen (fig. 3) was chosen as the internal standard reference for that sample. (7) The average thickness of all the pixels located within this internal reference area was calculated, and this value was considered to be equivalent to a mineral content of 100%. (8) The thickness values of the individual pixels of the digitized image were then divided by the average thickness of the internal standard. Each pixel now had a value in the unit of % mineral content relative to the sample internal standard. (9) A window covering an area 70 pixels (102 μm) high and 200 pixels (220 μm) wide

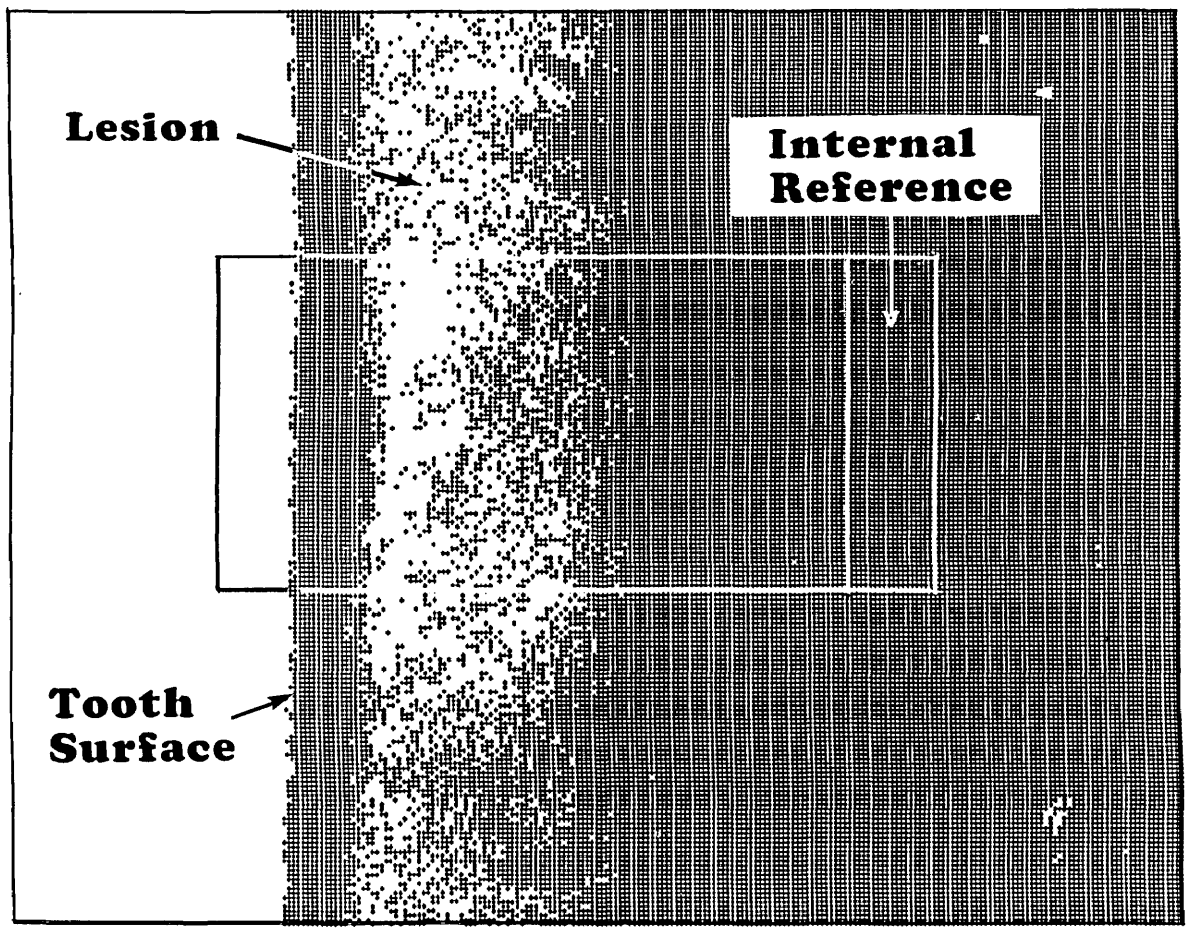

Figure 3. A digitized microradiographic image of a root specimen containing a lesion with a mineral dense surface layer. Black dots are pixels where the percent mineral contents were 60 or higher.

of the sample including the lesion and the internal reference was delineated (fig. 3), and the mean and standard deviation of the % mineral content of all the pixels within each column, i.e., at a given distance from the root surface, were calculated. (10) The data obtained were used to produce a mineral content profile of the specimen, i.e., the average mineral content as a function of distance (from the tooth surface toward the pulp).

3. Results

Curve B in figure 4 shows the relationship between the measured grey level values and the thickness of an aluminum step wedge. Regression statistics (table 1) of the data on 20 radiographic images of the step wedges from 5 radiographs shows that both the second [eq (2)] and third [eq (3)] order polynomial functions provided a better fit of the thickness vs. grey level data than did the first order-function [eq (1)]. Since there was no statistically significant difference between the second and the third order functions, in subsequent calculations the second order function was used for constructing the calibration curves. Data in table 1 show that for the second order curve the average standard error of thickness estimate is 0.135 layers.

In figure 5 the calculated thicknesses were plotted against the known thicknesses for the three step wedges from radiograph E (table 2). There was a good linear relationship between the two parameters. Listed in table 2 are the results of linear regression analysis of the data by the zero intercept model. It is seen that the calculated thickness and actual thickness are strongly correlated (mean correlation coefficient = 0.995). However, the slopes of the straight lines ranged from 0.809 to 1.528, suggesting considerable discrepancies between the calculated and the actual thicknesses. The mean standard error of the estimated Th_c is approximately 0.2 layers (table 2).

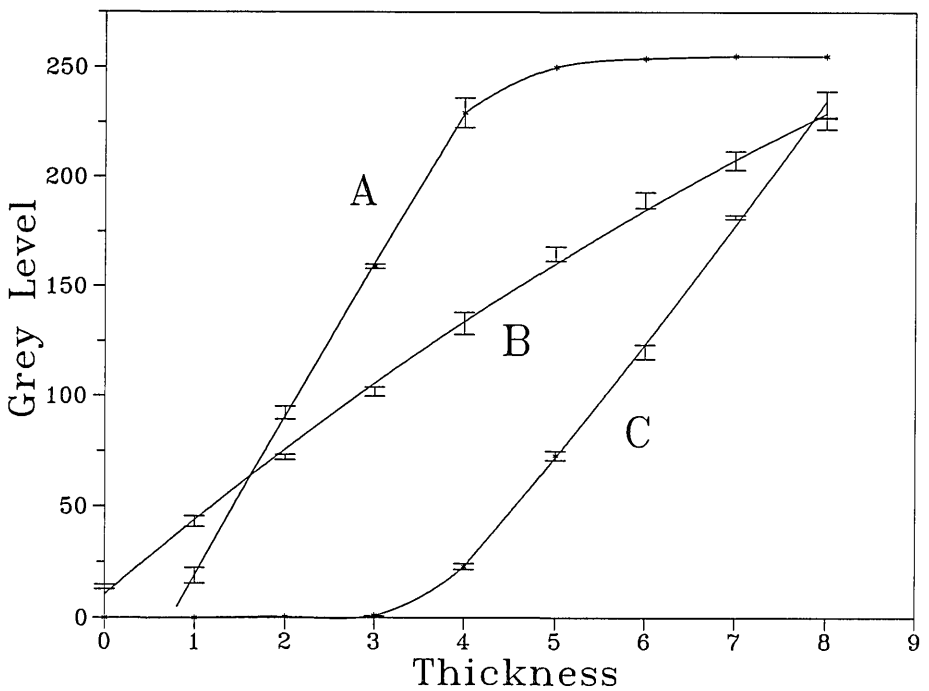

Figure 4. Relationships between grey level and thickness of aluminum step wedge under different radiographic or microscope illumination conditions (see text). The bars denote standard deviations ($n = 3$).

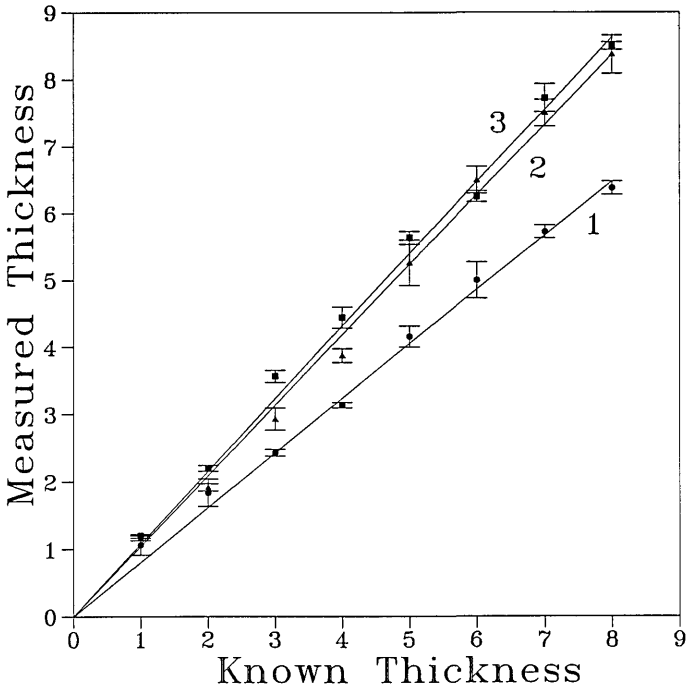

Figure 5. Relationships between known thicknesses and thicknesses calculated from the grey level values measured for the three step wedges in radiograph E (table 2). The straight lines are least square lines with forced zero intercept [eq (1)]. The bars denote standard deviations ($n = 3$).

Curve B in figure 6 shows the mean and standard deviation of % mineral content of a lesion as a function of distance from the tooth surface. The peak on the left corresponds to a mineral dense layer at the tooth surface preceding the body of the lesion. The mineral density profile of the same lesion after remineralization treatment is also shown (curve A, fig. 6). A two-tailed t test of the data shows that for this sample the increase in mineral content was significant in the area of the lesion from approximately 5 to 70 μm from the tooth surface. Figure 7 shows the average mineral profile of all four specimens before remineralization (curve B) and after the remineralization treatment (curve A). To gain a more quantitative picture, the average mineral gains in the various zones of the lesions (in 10 μm intervals from the tooth surface) were calculated from the data (table 3). The results show that immersing the root lesions in the pH 7.4 calcium phosphate solution produced a small but statistically significant increase in mineral content of the lesion to a depth approximately 70 μm.

Data contained in the digitized images of a caries lesion may be used to plot mineral content profiles in a three-dimensional coordinate system with the horizontal axes representing the location coordinates and the vertical axis representing the percent mineral content. Figures 8 (I) and 8 (II) show the images of a lesion before and after the remineralization treatment, respectively. The same data may also be used to produce isodensitraces of the radiographs [figs. 9 (I) and 9 (II)] in which the contour lines correspond to steps of 5% change in the mineral content. A commercially obtained software package (SURFER, Golden Software, Golden, CO) was used to produce the plots.

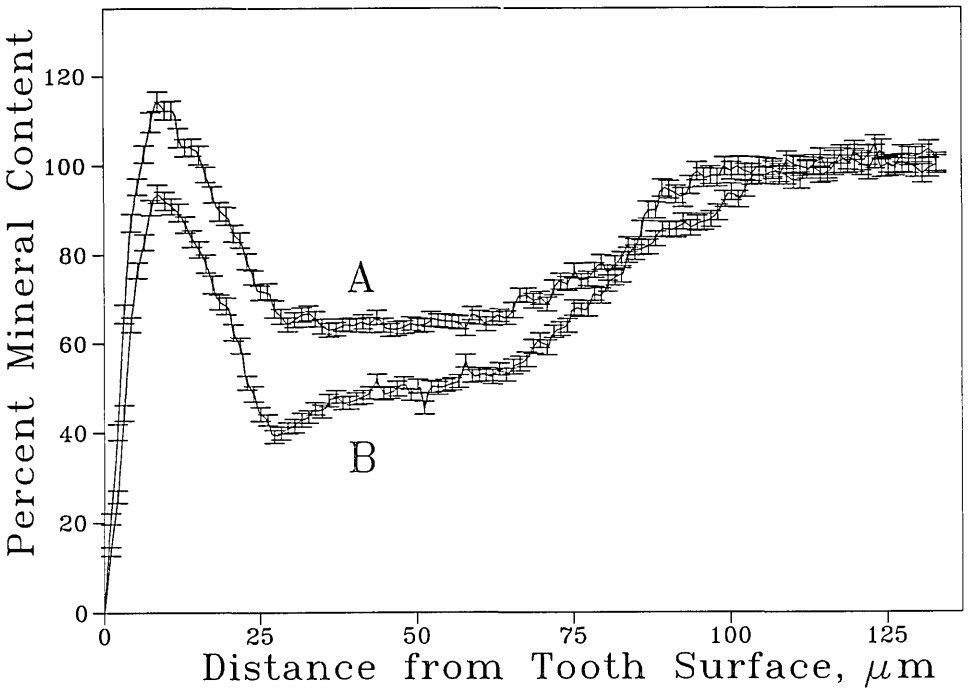

Figure 6. Mineral content profile of a root sample with lesion before (B) and after (A) a remineralization treatment. The profiles shown are averages of a window approximately 100 μm in height (70 pixels) as shown in figure 3. The bars denote standard errors of the mean ($n = 70$).

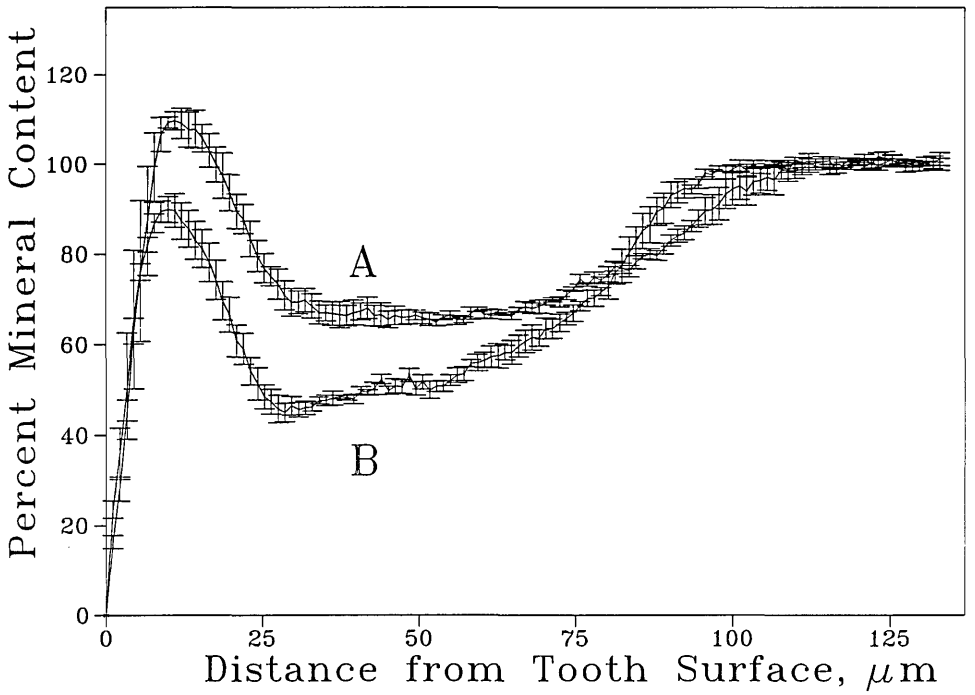

Figure 7. Average mineral content profile of 4 root lesions before (B) and after (A) a remineralization treatment. The bars denote standard errors of the mean ($n = 4$).

Table 3. Change in mineral content (%) of root dentin lesion produced by the remineralization treatment

	Distance (μm) from tooth surface							
	1-10	11-20	21-30	31-40	41-50	51-60	61-70	71-80
Before	57.5	79.5	51.0	47.2	50.8	52.7	59.0	67.8
S.D.[a]	(1.2)	(6.8)	(4.4)	(1.6)	(1.9)	(2.1)	(3.8)	(3.0)
After	67.8	103.0	78.0	67.5	66.3	65.9	67.5	72.6
S.D.	(8.2)	(5.0)	(4.5)	(4.0)	(2.8)	(1.1)	(0.5)	(1.1)
Paired Difference	-0.8[b]	20.9	28.5	21.4	15.7	12.9	7.5	3.3[b]
S.D.	(7.5)	(5.6)	(3.3)	(3.8)	(3.6)	(2.6)	(3.4)	(3.1)

[a] S.D. = standard deviation of the mean; $n = 4$.
[b] Statistically non-significant ($p > 0.05$).

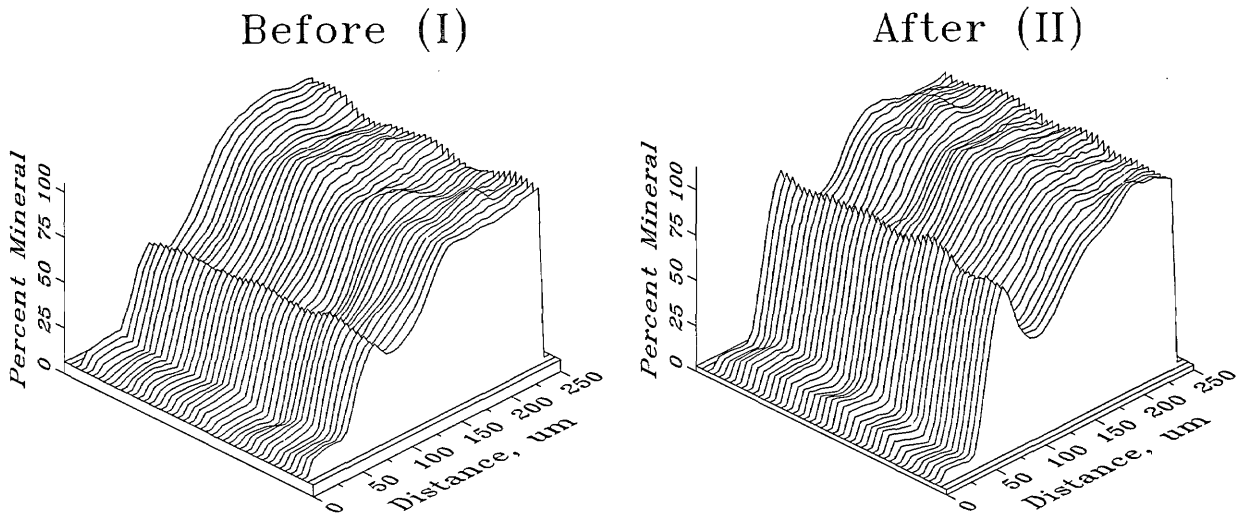

Figure 8. Mineral profiles of a root specimen with lesion before (I) and after (II) remineralization treatment. The horizontal axes are location coordinates and the vertical axis represents the mineral content.

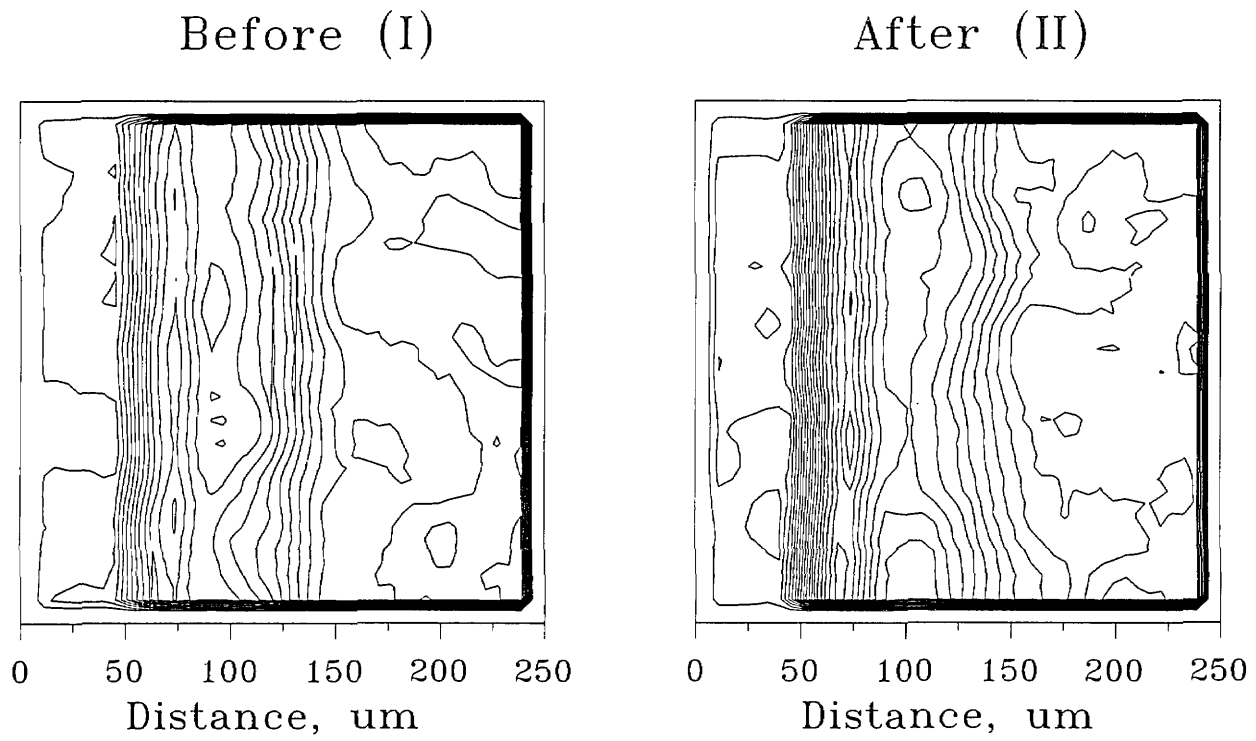

Figure 9. Isodensitraces of the same specimen as in figure 8 before (I) and after (II) remineralization treatment. The lines denote steps of 5% change in mineral content.

4. Discussion

The relationship between the grey level and the thickness of the aluminum step wedge is determined by the brightness and contrast of the radiographic image recorded in the digitized form. Figure 4 shows three characteristic relationships between the two parameters in three characteristic situations: (1) a near linear relationship holds for the lower portions of the standards, but after a certain thickness the grey level reaches the saturation values of 255 (curve A), (2) a near linear relationship prevails for the entire range of thickness (curve B), and (3) the grey levels for the first several standards were essentially zero, and a near linear relationship holds thereafter (curve C).

The brightness determines the horizontal location, whereas the contrast determines the slope of the standard curve. Thus curve A in figure 4 was obtained from an image with a greater brightness than the one from which curve C was obtained. Further, the radiographs that produced curves A and C had greater contrast than the one that produced curve B.

In the present experimental setup, the brightness and contrast of the digitized radiographic image are controllable by the following factors: (1) the brightness and contrast of the original radiograph; these, in turn, were determined by the x-ray exposure conditions and those used for developing the film, (2) light intensity of the microscope, which affects the brightness of the image, and (3) additional controls of brightness and contrast provided by the digital image analysis device through variable attenuation of the signals from the video camera.

Since curve B shown in figure 4 provides a more consistent relationship between grey level and thickness, the results reported in the present study were obtained under experimental conditions that would produce this type of calibration curve. It is noted that under some conditions curve A or C (fig. 4) may be desirable since it may allow for greater sensitivity of measurement because of the larger slope in the usable portion of the standard curve. On the other hand, since the standards are indistinguishable from one another over a portion of the curve (e.g., steps 5 through 8 for curve A), substantial errors would result should the sample mineral content fall within this region of the calibration curve.

Discrepancies in the calculated thickness and actual thickness of step wedges located in different areas of a given radiograph (fig. 5) are presumably

due to variations in the contrast and brightness over the relatively small distances separating the wedges. In some cases, e.g., E1 in table 2, the error was over 20%. This suggests that errors of such magnitude may be present in the mineral content of a tooth specimen estimated by a calibration curve established from a set of standards situated just 1 or 2 mm away on the same radiograph. Fortunately, data obtained in the present study indicate that the calculated and actual thickness are linearly correlated (fig. 5 and table 2). The linear relationship, with the intercept set to zero, makes it possible to correct for the deviation if an additional internal standard located within the sample is available. In the case of measuring the mineral content of a tooth specimen with caries lesions, the sample internal standard may be obtained by assigning an area located in the sound portion of the specimen to have 100% mineral content. Thus, the mineral content of the entire sample may be recalculated as percent of the mineral content of the internal standard. The data obtained from the step wedges indicate that when this procedure is used, the standard error of the estimated thickness is approximately 0.2 layers (table 2). Since the radiopacity of the sound portion of a typical tooth sample is comparable to that of 5 to 7 layers of aluminum, the standard error in the estimated mineral content would be in the range from 4 to 2.9% of the mineral content of the sound root dentin or enamel.

Quantitative microradiography using the procedure described here has advantages over that conducted by scanning the radiograph with a microdensitometer [5,6]. The digital image analysis method captures from the radiograph information on the mineral content in a two-dimensional area of the specimen. The digitized radiographic image obtained is equivalent to hundreds of contiguous scannings of the microradiograph at approximately 1.5 μm intervals. The mineral content profile produced (fig. 6) reveals both the mean and the variance of the mineral content as a function of distance from the tooth surface in a specific area of the specimen. Since this method does not require mechanically moving the densitometer, it generally can produce a higher spatial resolution than that obtainable in the scanning method. Elliott et al. [12] reported a scanning x-ray microradiographic system in which the x-ray absorption by the specimen was measured directly without using photographic recordings. By step-by-step translation of the specimen, a two-dimensional radiographic image with a resolution of 20 μm and a reproducibility of 1.5% can be obtained. Compared to this system, the digital image analysis method requires substantially shorter measurement times and produces higher spatial resolution. Photographic artifacts, which are common to all methods using photographic film recordings, are minimized by the use of thickness standards and an additional sample internal reference described above.

Like many other biological samples, tooth specimens are highly variable in their response to a given treatment. Consequently, a large sample size is often needed to detect small differences in mineral content distribution resulting from a remineralization treatment. The procedure investigated in the present study allows the mean and standard deviation of mineral content distribution (as a function of distance from the tooth surface) of a designated area of the lesion to be measured both before and after certain treatment. The quantitative nature of the measurement facilitates statistical analysis of the data and aids in detection of small but significant differences such as that shown in figure 7.

Acknowledgment

This investigation was supported, in part, by USPHS Research Grant DE05354 to the American Dental Association Health Foundation from the National Institutes of Health—National Institute of Dental Research and is part of the dental research program conducted by the National Institute of Standards and Technology in cooperation with the American Dental Association Health Foundation.

5. References

[1] Darling, A. I., Int. Dent. J. **17**, 684 (1967).
[2] Sharpe, A. N., Arch. Oral Biol. **12**, 583 (1967).
[3] Theuns, H. M., and Groeneveld, A., Caries Res. **11**, 293 (1977).
[4] Langdon, D. J., Elliott, J. C., and Fernhead, R. W., Caries Res. **14**, 359 (1980).
[5] Mallon, D. E., and Mellberg, J. R., J. Dent. Res. **64**, 112 (1985).
[6] Nyvad, B., ten Cate, J. M., and Fejerskov, O., Caries Res. **23**, 218 (1989).
[7] Bergstrom, D. H., Fox, J. L., and Higuchi, W. I., J. Pharmaceut. Sci. **73**, 650 (1984).

[8] Theuns, H. M., Van Dijk, J. W. E., Driessens, F. C. M., and Groeneveld, A., Caries Res. **18**, 7 (1984).
[9] Takagi, S., Chow, L. C., and Brown, W. E., J. Dent. Res. **64**, 325 (1985).
[10] Jordan, T. H., personal communication.
[11] Tung, W., personal communication.
[12] Elliott, J. C., Dowker, S. E. P., and Knight, R. D., J. Microscop. **123**, 89 (1981).

About the authors: *Dr. Laurence C. Chow is Chief Research Scientist, Dental Chemistry Program, and Dr. Shozo Takagi is Project Leader with the Paffenbarger Research Center, American Dental Association Health Foundation at NIST. Mr. Wayne Tung was a summer student worker at NIST. Dr. Truman H. Jordan is Professor of Chemistry at Cornell College.*

Volume 96, Number 2, March-April 1991
Journal of Research of the National Institute of Standards and Technology

[J. Res. Natl. Inst. Stand. Technol. 96, 215 (1991)]

Bidirectional Scattering Distribution Function (BSDF): A Systematized Bibliography

Volume 96 Number 2 March-April 1991

Clara Asmail

National Institute of Standards and Technology,
Gaithersburg, MD 20899

In conjunction with the development of a bidirectional scattering metrology project, a large number of papers pertaining to the theory and measurement of bidirectional scattering from optical surfaces were collected and categorized. This collection includes papers that deal with various aspects of the bidirectional scattering distribution function (BSDF), its measurement, interpretation, use, and implications. Each paper is classified in one or more subject categories on the basis of its technical content. The subject categories are included just to serve as a key to the most salient characteristics of each paper cited. Because of the interest in this field, this bibliography is being published as a service to the public.

Key words: bidirectional reflectance distribution function (BRDF); bidirectional scattering distribution function (BSDF); bidirectional transmittance distribution function (BTDF); coherence; diffuse reflectance; instrument signature; inverse scattering problem; polarization; scattering theory; specular reflectance; stray light; surface finish.

Accepted: December 13, 1990

1. Introduction

The bidirectional scattering distribution function (BSDF) radiometrically characterizes the scatter of optical radiation from a surface as a function of the angular positions of the incident and scattered beams. By definition, it is the ratio of the scattered radiance to the incident irradiance: the unit is inverse steradian. The term bidirectional reflectance distribution function (BRDF) is used when specifically referring to reflected scatter. Likewise, bidirectional transmittance distribution function (BTDF) refers to scatter transmitted through a material.

The bidirectional characterization of elastic scatter from surfaces is a property that is required for the evaluation of elements contained within larger systems that need minimal or controlled scattered light. The need for this information is readily seen in applications such as ring laser gyroscopes and telescopes. This type of information is also requisite for characterization of materials intended for use in temperature control where thermal radiation must be modelled or in imaging applications where stray light must be suppressed. It may also be used to assist the acceptance/rejection process in optical manufacturing settings.

The present state of most of the facilities measuring this quantity needs to be upgraded to support new and more stringent requirements as well as recent strides in the production of high-quality optics.

There is a lack of uniformity throughout the community for physical standards which can ascertain the accuracy of BSDF measurements (paper 91). The NIST Bidirectional Scattering Metrology Project is currently developing an instrument which will later serve to develop standard reference materials as well as a standard measurement technique.

In conjunction with the development of this BSDF instrument, a large number of papers pertaining to the theory and measurement of bidirec-

tional scattering from optical surfaces were collected and categorized. This collection includes papers that deal with various aspects of the BSDF, its measurement, interpretation, use, and implications.

Each paper is classified in one or more subject categories on the basis of its technical content. The subject categories are included just to serve as a key to the most salient characteristics of each paper cited. In the literature, there is a bibliography (paper 117) of papers published prior to 1975 that relate to scattering from surfaces. Building upon that bibliography, this bibliography includes papers related to BSDF published since that time to the present. Neither the category classification list nor the list of papers is complete. There were two selection criteria used to determine whether a paper should be included in this bibliography: the paper was used during certain phases of the NIST project development and/or it was regarded as relevant and important to the field. However, inclusion or omission from the list does not necessarily imply endorsement or reproval, respectively. This systematized bibliography is sufficiently extensive to be of significant help to workers in the field, and particularly to those just beginning to work in it. For further breadth of information, the reader is suggested to review the conference proceedings from the Society of Photo-Optical Instrumentation Engineers (SPIE) that focus on scattering from surfaces: some papers from each of these are cited here.

2. Categories

As an aid to identifying papers related to a certain field, each of the papers is listed under each category in which it has been classified. Due to the wide interdisciplinary nature of optical scattering metrology, some topics had to be grouped together so that the list would not become unmanageable. (In many instances, the title of the articles suggest the information covered.) The subject categories are coded and used as follows:

Abs—Aberrations

The optical design of a system determines the aberrations that will be present—assuming accurate alignment—and their magnitudes. The calculation of these aberrations and their effect on the measurement of BSDF are addressed in the following papers: 3,96,102,159,160.

Aprt—Apparatus

Many different instruments are described in the literature. A sampling of these apparatus overviews is contained in the following papers: 4,12,31,41, 51,52,63,65,66,76,77,79,83,84,87,89,90,93,94,95,103, 111,112,132,113,118,120,122,128,129,136,137,138, 140,145,146,151,159,160,161,166,168,169.

Calb—Calibration

Techniques for calibration and/or error analysis include reference methods and absolute methods. Specific details concerning calibration and the philosophy of calibration are discussed in these papers: 23,33,34,83,89,108,145,158.

Coh—Coherence

The use of laser sources in BSDF instruments is very common. Coherence becomes a critical property of these sources in diffuse BSDF metrology. The following papers address the property as it pertains to radiometry in general and to BSDF metrology in particular: 3,8,37,39,40,49,59,61,63, 73,80,97,98,101,125,126.

Desn—Design

Design criteria and plans or layouts of components or subsystems of BSDF instruments are separated out and described in detail. These subsystems include source, sample manipulation, receiver, attenuation, apertures, etc: 3,10,11,21,22,27,28,29,31, 35,41,51,52,60,66,68,69,71,76,85,86,87,89,90,93,94, 95,108,112,132,118,119,124,128,130,136,141,142,156, 157,159,160,162,163,166,168,170.

Diff—Diffraction

Truncation of optical beams by apertures cause diffraction and thereby affect the instrument signature of BSDF instruments. This effect is discussed in the following papers: 3,49,69,70,72,89,96,139, 159,160.

Expt—Experimental Data

These articles include experimental results in the form of tabulated data or graphs from a variety of different types of measurements. Some of these include data from actual BSDF scans on particular material samples while others give interpretive results highlighting instrument capabilities. Still

other papers give profilometry data that yield topographic information. The particular type of experimental data given within each paper should be obvious from the title of the paper: 4,5,7, 9,13,15,16,17,18,20,22,24,25,26,28,29,30,32,35,36,38, 40,41,42,44,46,48,52,53,54,57,59,64,67,73,76,78,79, 83,88,91,92,94,99,100,101,103,104,109,110,111,132, 113,114,115,119,120,121,122,123,127,128,129, 130, 131,133,134,135,138,139,140,142,143,145,147,149, 151,152,154,158,161,165,167,168,169,170.

Inst—Instrument Signature

The background measurement of the noise equivalent BSDF, or the instrument signature, limits an instrument to the measurement of samples that have a BSDF larger than the NEBSDF. Specific instrument profiles or signatures are displayed in some of the following papers. The other papers address general concerns in obtaining and improving the signature of an instrument: 4, 12, 36,76,77,85,86,90,120,124,130,136,137,139,141,151, 159,160,162,164,166,168,171.

Matl—Materials/Coatings

Particular optical materials and/or coatings are identified and experimental BSDF data are given for each of these in the following papers: 2,7,9, 13,16,17,22,24,25,28,29,32,35,42,48,52,53,64,67,76, 78,83,92,94,99,100,104,109,110,113,114,115,121,122, 123,129,130,131,133,135,138,145,149158,162,165,

Polarization

Polarization control, theory, and associated problems are examined: 5,6,23,24,25,59,79,95,144, 147,167.

Prof—Profile Analysis Techniques

Various types of mechanical and optical surface profiling techniques are described and/or compared against optical scattering predictions of surface finish (or the inverse: predictions of optical scatter from surface finish): 1,2,17,20,30,39,43,44, 46,54,56,57,59,65,88,91,100,109,111,134,137,140,150, 151.

Stnd—Standard Reference Methods

The following papers describe techniques used for, or problems in, referencing BSDF measurements, thereby assigning a level of confidence to the accuracy of the measurement: 33,53,83,91, 92,108,130,145,158,164.

Stra—Stray Light

Control, or suppression, of geometrically stray light is examined in this group of papers. Included in these are some papers which evaluate baffling materials with BRDF data: 18,22,27,28,29,42, 50,58,60,69,71,78,87,90,113,123,146,149,156,157,163, 170.

Surv—Survey

Below is a list of papers that are outstanding in their fields and provide comprehensive coverage of a well-defined topic within BSDF metrology: 19,24,45,46,65,74,76,77,81,82,89,91,92,105,106,107, 108,117,130,140,148,171.

Thry—Scattering Theory

Among the theoretical questions explored throughout these papers are: basic definition of BSDF, scattering theory of surfaces, mathematical treatment of surfaces, subsurface contributions to scatter, inverse scattering problem, and scaling of BSDF with respect to angle of incidence and wavelength: 1,3,5,6,7,8,12,14,15,16,17,18,20,23,26,37,38, 39,40,43,44,45,46,47,49,55,56,57,58,59,61,62,69,70, 71,72,74,75,77,79,80,81,82,90,94,96,97,98,101,103, 105,106,107,108,109,110,111,116,120,124,125,126, 129,131,134,139,144,146,147,148,150,152,153,154, 155,156,157,161,162,167,170.

Topo—Topography/Surface Finish

Surface roughness and sample isotropy, homogeneity, and cleanliness are all topographic contributions to optical scatter. These topics as well as some subsurface contributions are treated in the following papers: 1,2,4,9,14,15,16,17,18,19,20,30, 38,39,40,43,44,45,46,47,54,55,56,57,62,74,75,88,100, 109,110,111,116,120,121,125,127,134,135,139,142, 144,147,150,152,153,154,155,161,162,167,169.

Tran—Transmitted Scatter

Issues related to the bidirectional transmittance distribution function, BTDF, are considered in these papers: 52,103,122,126.

3. Bibliography

The papers are listed below in alphabetical order according to first author and are numbered. The related topic codes are listed alphabetically in the line immediately following the citation.

1. Al-Jumaily, G. A., Wilson, S. R., and McNeil, J. R., Frequency Response Characteristics of an Optical Scatterometer and a Surface Profilometer, SPIE Proceedings, **675** (1986).
Prof Thry Topo
2. Al-Jumaily, G. A., Wilson, S. R., McNally, J. J., McNeil, J. R., Bennett, J., and Hurt, H. H., Influence of Metal Films on the Optical Scatter and Related Micro-Structure of Coated Surfaces, Appl. Opt. **25**, 20 (1986) p. 3631.
Matl Prof Topo
3. Allred, D. B., and Mills, J. P., Effect of Aberrations and Apodization on the Performance of Coherent Optical Systems 3: The Near Field, Appl. Opt. **28**, 4 (1989) p. 673.
Abs Coh Desn Diff Thry
4. Amra, C., Grezes-Besset, C., Roche, P., and Pelletier, E., Description of a scattering apparatus: application to the problems of characterization of opaque surfaces, Appl. Opt. **28**, 14 (1989) p. 2723.
Aprt Expt Inst Topo
5. Bahar, E., and Fitzwater, M., Like- and Cross-Polarized Scattering Cross Sections for Random Rough Surfaces: Theory and Experiment, J. Opt. Soc. Am. A., **2**, 12 (1985) p. 2295.
Expt Pol Thry
6. Bahar, E., and Fitzwater, M., Full-Wave Copolarized Nonspecular Transmission and Reflection Scattering Matrix Elements for Rough Surface, J. Opt. Soc. Am., A., **5**, 11 (1988) p. 1873.
Pol Thry
7. Baltes, H., and Wolfe, W., K Correlations and Facet Models in Diffuse Scattering: Experimental Evaluation, Opt. Lett., **5**, 12 (1980) p. 549.
Expt Matl Thry
8. Baltes, H., Steinle, B., Jakeman, E., and Hoenders, B., Diffuse Reflectance and Coherence, Infrared Phys., **19** (1979) p. 461.
Coh Thry
9. Barnes, W., Jr., and McDonough, R., Low Scatter Finishing of Aspheric Optics, Opt. Eng., **18**, 2 (1979) p. 143.
Expt Matl Topo
10. Bartell, F., Infrared Calibration: Very Low Signals May Have Very Large Errors, SPIE Proceedings, **499** (1984) p. 108.
Desn
11. Bartell, F., BRDF Measurement Equipment Intrinsic Design Considerations, SPIE Proceedings, **511** (1984) p. 31.
Desn
12. Bartell, F., Dereniak, E., and Wolfe, W., The Theory and Measurement of Bidirectional Reflectance Distribution Function (BRDF) and Bidirectional Transmittance Distribution Function (BTDF), SPIE Proceedings, **257** (1980) p. 154.
Aprt Inst Thry
13. Bartell, F., Hubbs, J., Nofziger, M., and Wolfe, W., Measurements of Martin Black at ~10 μm, Appl. Opt., **21**, 17 (1982) p. 3178.
Expt Matl
14. Bennett, H., and Ricks, D. W., Effects of Surface and Bulk Defects in Transmitting Materials on Optical Resolution and Scattered Light, SPIE Proceedings, **683** (1986).
Thry Topo
15. Bennett, H., and Porteus, J., Relation Between Surface Roughness and Specular Reflectance at Normal Incidence, J. Opt. Soc. Am., **51**, 2 (1961) p. 123.
Expt Thry Topo
16. Bennett, H. E., Specular Reflectance of Aluminized Ground Glass and the Height Distribution of Surface Irregularities, J. Opt. Soc. Am., **53**, 12 (1963) p. 1389.
Expt Matl Thry Topo
17. Bennett, H. E., Scattering Characteristics of Optical Materials, Opt. Eng., **17**, 5 (1978) p. 480.
Expt Matl Prof Thry Topo
18. Bennett, H. E., Reduction of Stray Light from Optical Components, SPIE Proceedings, **107** (1977) p. 24.
Expt Stra Thry Topo
19. Bennett, J., When is a Surface Clean? Optics and Photonics News (June 1990) p. 29.
Surv Topo
20. Bennett, J., and Dancy, J., Stylus Profiling Instrument for Measuring Statistical Properties of Smooth Optical Surfaces, Appl. Opt. **20**, 10 (1981) p. 1785.
Expt Prof Thry Topo
21. Bennett, K., and Byer, R., Computer-Controllable Wedged-Plate Optical Variable Attenuator, Appl. Opt. **19**, 14 (1980) p. 2408.
Desn
22. Bergener, D., Pompea, S., Shepard, D., and Breault, R. Stray Light Rejection Performance of SIRTF: A Comparison, SPIE Proceedings, **511** (1984) p. 65.
Desn Expt Matl Stra
23. Bickel, W. S., and Bailey, W. M., Stokes Vectors, Mueller Matrices, and Polarized Scattered Light, Am. J. Phys., **53**, 5 (May 1985) p. 468.
Calb Pol Thry
24. Bickel, W. S., Zito, R. R., and Iafelice, V., Polarized Light Scattering From Metal Surfaces, J. Appl. Phys., **61**, 12 (June 15, 1987) p. 5392.
Expt Matl Pol Surv
25. Blau, H. H., Gray, E. L., and Bourioius, G. M. B., Reflection and Polarization Properties of Powder Materials, Appl. Opt., **6**, 11 (Nov. 1967) p. 1899.
Expt Matl Pol
26. Blazey, R., Light Scattering by Laser Mirrors, Appl. Opt. **6**, 5 (May 1967) p. 831.
Expt Thry
27. Breault, R. P., Current Technology of Stray Light, SPIE Proceedings, **675** (1986).
Desn Stra
28. Breault, R. P., Specular Black Vane Cavities, SPIE Proceedings, **384** (1983) p. 90.
Desn Expt Matl Stra
29. Breault, R. P., Problems and Techniques in Stray Radiation Supression, SPIE Proceedings, **107** (1977) p. 2.
Desn Expt Matl Stra
30. Bristow, T., and Lindquist, D., Surface Measurements with a Non-Contact Nomarski-Profiling Instrument, SPIE Proceedings, **816** (1987).
Expt Prof Topo
31. Brooks, L., and Wolfe, W., Microprocessor-Based Instrumentation for Bidirectional Reflectance Distribution Function (BRDF) Measurements, SPIE Proceedings, **257** (1980) p. 182.
Aprt Desn

32. Brooks, L., Hubbs, J., Bartell, F., and Wolfe, W., Scattering Characteristics of Martin Black at 118 μm, Appl. Opt., **21**, 14 (1982) p. 2465.
Expt Matl
33. Cady, F. M., Bjork, D. R., Rifkin, J., and Stover, J. C., Linearity in BSDF Measurements, SPIE Proceedings, **1165** (1989) .
Calb Stnd
34. Cady, F. M., Bjork, D. R., Rifkin, J., and Stover, J. C., BRDF Error Analysis, SPIE Proceedings, **1165** (1989) .
Calb
35. Cady, F. M., Cheever, D. R., Klicker, K. A., and Stover, J. C., Comparison of Scatter Data from Various Beam Dumps, SPIE Proceedings, **818** (1987) .
Desn Expt Matl
36. Cady, F. M., Stover, J. C., Schiff, T. F., Klicker, K. A., and Bjork, D. R., Measurement of Very Near Specular Scatter, SPIE Proceedings, **967** (1988) .
Expt Inst
37. Carter, W., and Wolf, E., Coherence Properties of Lambertian and Non-Lambertian Sources, J. Opt. Soc. Am., **65**, 9 (1975) p. 1067.
Coh Thry
38. Celli, V., Maradudin, A., Marvin A., and McGurn, A., Some Aspects of Light Scattering from a Randomly Rough Metal Surface, J. Opt. Soc. Am., A., **2**, 12 (1985) p. 2225.
Expt Thry Topo
39. Chandley, P. J., Surface Roughness Measurements from Coherent Light Scattering, Opt. Quantum Electron., **8** (1976) p. 323.
Coh Prof Thry Topo
40. Chandley, P. J., Determination of the Autocorrelation Function of Height on a Rough Surface from Coherent Light Scattering, Opt. Quantum Electron., **8** (1976) p. 329.
Coh Expt Thry Topo
41. Cheever, D. R., Cady, F. M., Klicker, K. A., and Stover, J. C., Design Review of a Unique Complete Angle Scatter Instrument (CASI), SPIE Proceedings, **818** (1987) .
Aprt Desn Expt
42. Chocol, C., and Wade, J., Reducing Optical Noise, SPIE Proceedings, **107** (1977) p. 130.
Expt Matl Stra
43. Church, E., and Zavada, J., Residual Surface Roughness of Diamond-Turned Optics, Appl. Opt., **14**, 8 (1975) p. 1788.
Prof Thry Topo
44. Church, E., Jenkinson, H., and Zavada, J., Measurement of the Finish of Diamond-Turned Metal Surfaces by Differential Light Scattering, Opt. Eng., **16**, 4 (1977) p. 360.
Expt Prof Thry Topo
45. Church, E., Jenkinson, H., and Zavada, J., Relationship Between Surface Scattering and Microtopographic Features, Opt. Eng., **18**, 2 (1979) p. 125.
Surv Thry Topo
46. Church, E., Sanger, G., and Takacs, P., Comparison of Wyko and TIS Measurements of Surface Finish, SPIE Proceedings, **749** (1987) p. 65.
Expt Prof Surv Thry Topo
47. Church, E. L., Statistical Effects in the Measurement and Characterization of Smooth Surfaces, SPIE Proceedings, **511** (1984) .
Thry Topo
48. Compton, J., Martin, J., and Quinn, T., Some Measurements of Outgassing Properties and Far-Infrared Reflectivities of Two Optical Blacks, J. Phys., **7** (1974) p. 2501.
Expt Matl
49. Considine, P. S., Effects of Coherence on Imaging Systems, J. Opt. Soc. Am., **56**, 8 (1966) p. 1001.
Coh Diff Thry
50. Crandell, F. F., General Concepts and Approach on Making Stray Light Calculations Without the Use of Large Computers, SPIE Proceedings, **257** (1980) .
Stra
51. Davis, L., and Kepros, J., Improved Facility for BRDF/BTDF Optical Scatter Measurements, SPIE Proceedings, **675**, 1 (1986) p. 24.
Aprt Desn
52. Dereniak, E., Brod, L., and Hubbs, J., Bidirectional Transmittance Distribution Function Measurements on ZnSe, Appl. Opt., **21**, 24 (1982) p. 4421.
Aprt Desn Expt Matl Tran
53. Dereniak, E., Stuhlinger, T., and Bartell, F., Bidirectional Reflectance Distribution Function of Gold-Plated Sandpaper, SPIE Proceedings, **257** (1980) p. 184.
Expt Matl Stnd
54. Detrio, J., and Miner, S., Standardized Total Integrated Scatter Measurements of Optical Surfaces, Opt. Eng., **24**, 3 (1985) p. 419.
Expt Prof Topo
55. Eastman, J., and Baumeister, P., The Microstructure of Polished Optical Surfaces, Opt. Commun., **12**, 4 (1974) p. 418.
Thry Topo
56. Elson, J., and Bennett, J., Vector Scattering Theory, Opt. Eng., **18**, 2 (1979) .
Prof Thry Topo
57. Elson, J., and Bennett, J., Relation Between the Angular Dependence of Scattering and the Statistical Properties of Optical Sufaces, J. Opt. Soc. Am., **69**, 1 (1979) p. 31.
Expt Prof Thry Topo
58. Elson, J. M., and Bennett, H. E., Image Degradation Caused by Direct Scatter from Optical Components into the Image Plane, SPIE Proceedings, **511** (1984) .
Thry Stra
59. Elson, J. M., Rahn, J. P., and Bennett, J. M., Relationship of the TIS from Multilayer-Coated Optics to Angle of Incidence, Polished Correlation Length and Roughness, Appl. Opt., **22**, 20 (1983) p. 3207.
Coh Expt Pol Prof Thry
60. Freniere, E. R., First-Order Design of Optical Baffles, SPIE Proceedings, **257** (1980) .
Desn Stra
61. Fribert, A. T., Effects of Coherence in Radiometry, SPIE Proceedings, **194** (1979) p. 55.
Coh Thry
62. Fung, A. K., and Chen, M. F., Numerical Simulation of Scattering from Simple and Composite Random Surfaces, J. Opt. Soc. Am., A., **2**, 12 (1985) p. 2274.
Thry Topo
63. Gacusan, L., Kwiatkowski, S., Sullivan, B., and Snyder, J., Coherent Heterodyne Scatterometer, SPIE Proceedings, **967** (1988).
Aprt Coh
64. Geikas, G. I., Scattering Characteristics of Etched Electroless Nickel, SPIE Proceedings, **257** (1980).
Expt Matl
65. Gillespie, C. H., Edwards, D. F., and Stover, J. C., The Application of Angular Resolved Scatter to the Documentation of Damage to Smooth Mirrors, SPIE Proceedings, **675** (1986).
Aprt Prof Surv

66. Gilliam, L. E., and Osiecki, R. A., An In-Vacuum BR/TDF Measurement Apparatus, SPIE Proceedings, **675** (1986) .
Aprt Desn
67. Grammer, J. R., Bailin, L. J., Blue, M. D., and Perkowitz, S., Absorbing Coatings for the Far-Infrared, SPIE Proceedings, **257** (1980) .
Expt Matl
68. Greninger, C. E., Reflective Device for Polarization Rotation, Appl. Opt., **27**, 4 (1988) p. 774.
Desn
69. Greynolds, A. W., Simple Formulas for Calculating Near-Field Diffraction Profiles, SPIE Proceedings, **818** (1987) .
Desn Diff Stra Thry
70. Greynolds, A. W., Method for Calculating Diffraction Effects in Opto-Mechanical Systems of Arbitrary Geometry, SPIE Proceedings, **257** (1980) .
Diff Thry
71. Greynolds, A. W., Formulas for Estimating Stray-Radiation Levels in Well-Baffled Optical Systems, SPIE Proceedings, **257** (1980) .
Desn Stra Thry
72. Haas, R. A., Theory of Laser Beam Apodization with a Graded Random Phase Window, Appl. Opt., **27**, 13 (1988) p. 2708.
Diff Thry
73. Harris, F. S., Jr., Sherman, G. C., and Morse, F. L., Experimental Comparison of Scattering of Coherent and Incoherent Light, IEEE Trans. Antennas and Propag., **AP-15**, 1 (1967) p. 141.
Coh Expt
74. Harvey, J. E., Light-Scattering Characteristics of Optical Surfaces, SPIE Proceedings, **107** (1977) p. 41.
Surv Thry Topo
75. Hoenders, B., Jakeman, E., Baltes, H., and Steinle, B., K Correlations and Facet Models in Diffuse Scattering, Opt. Acta, **26**, 10 (1979) p. 1307.
Thry Topo
76. Hsia, J., and Richmond, J., A High Resolution Laser Bidirectional Reflectometer with Results on Several Optical Coatings, J. Res. Natl. Bur. Stand. (U.S.), **80A**, 2 (1976) p. 189.
Aprt Desn Expt Inst Matl Surv
77. Hsia, J. J., and Weidner, V. R., NBS 45°/Normal Reflectometer for Absolute Reflectance Factors, Metrologia, **17** (1982) p. 92.
Aprt Inst Surv Thry
78. Hubbs, J. E., Brooks, L. D., Nofziger, M. J., Bartell, F. O., and Wolfe, W. L., Bidirectional Reflectance Distribution Function of the Infrared Astronomical Satellite Solar-Shield Material, Appl. Opt., **21**, 18 (1982) p. 3323.
Expt Matl Stra
79. Iafelice, V. J., and Bickel, W. S., Polarized Light-Scattering Matrix Elements for Select Perfect and Perturbed Optical Surfaces, Appl. Opt., **26**, 12 (June 15, 1987) p. 2410.
Aprt Expt Pol Thry
80. Jannson, J., Jannson, T., and Wolf, E., Spatial Coherence Discrimination in Scattering, Opt. Lett., **13**, 12 (1988) p. 1060.
Coh Thry
81. Janeczko, D. J., Power Spectrum Standard for Surface Roughness: Part 1, SPIE Proceedings, **1165** (1989) .
Surv Thry
82. Judd, Deane, Terms, Definitions, and Symbols in Reflectometry, J.Opt. Soc. Am., **57**, 4 (1967) p. 445.
Surv Thry
83. Erb, W., Requirements for Reflection Standards and the Measurement of Their Reflection Values, Appl. Opt., **14**, 2 (Feb. 1975) p. 493.
Aprt Calb Expt Matl Stnd
84. Kepros, J., and Davis, L., Comparison of Two BRDF Measuring Systems, SPIE Proceedings, **675** (1986) p. 34.
Aprt
85. Klicker, K. A., Stover, J. C., Cheever, D. R., Cady, F. M., Practical Reduction of Instrument Signature in Near Specular Light, SPIE Proceedings, **749** (1987) .
Desn Inst
86. Klicker, K. A., Stover, J. C., and Wilson, D. C., Near Specular Scatter Measurement Techniques for Curved Samples, SPIE Proceedings, **967** (1988) .
Desn Inst
87. Kung, G. C., Scattering of Baffle Vane Edges, SPIE Proceedings, **511** (1984) .
Aprt Desn Stra
88. Lange, S. R., and Parks, R. E., Characterization of Scattering from Diamond-Turned Surfaces, SPIE Proceedings, **257** (1980) .
Expt Prof Topo
89. Lastovka, J. B., An Optical Apparatus for Very-Small-Angle Light Scattering-Design, Analysis and Performance, Bell Syst. Tech. J., **55**, 9 (1976) p. 1225.
Aprt Calb Desn Diff Surv
90. Lee, W. W., Scherr, L. M., and Barsh, M. K., Stray Light Analysis and Suppression in Small Angle BRDF/BTDF Measurement, SPIE Proceedings, **675** (1986) .
Aprt Desn Inst Stra Thry
91. Leonard, T. A., Introduction to the Relationship Between Surface Roughness and BRDF, (April 1989) (Available from author) .
Expt Prof Stnd Surv
92. Leonard, T.A., BRDF Round Robin, SPIE Proceedings, **967** (1988) .
Expt Matl Stnd Surv
93. Leonard, T., The Art of Optical Scatter Measurement, 20th Symposium on Optical Materials for High Power Lasers, Boulder, CO, (1988) .
Aprt Desn
94. Locke, B. R., and Donovan, R. P., Particle Sizing Uncertainties in Laser Scanning of Silicon Wafers, J. Electrochem. Soc., (July 1987) p. 1763.
Aprt Desn Expt Matl Thry
95. Lovik, M., and Scheeline, A., Active Polarization Compensation and Goniometer for Angularly Resolved Light Scattering Measurements, Appl. Opt., **27**, 23 (1988) p. 4931.
Aprt Desn Pol
96. Mahahan, V. N., Uniform Versus Gaussian Beams: A Comparison of the Effects of Diffraction, Obsuration, and Aberrations, J. Opt. Soc. Am, **3**, 4 (1986) p. 470–485.
Abs Diff Thry
97. Marchand, E., and Wolf, E., Radiometry with Sources of Any State of Coherence, J. Opt. Soc. Am., **64**, 9 (1974) p. 1219.
Coh Thry
98. Marron, J., and Schroeder, K., Speckle from Rough Rotating Objects, Appl. Opt., **27**, 20 (1988) p. 4279.
Coh Thry
99. McGary, D. E., Stover, J. C., Rifkin, J., Cady, F. M., and Cheever, D. R., Separation and Measurement of Surface Scatter and Volume Scatter from Transparant Optics, SPIE Proceedings, **967** (1988).
Expt Matl

100. McNeil, J. R., and Al-Jumaily, G. A., Optical Scatter Characteristics and Surface Effects in Coated Metal Surfaces, SPIE Proceedings, **675** (1986) .
Expt Matl Prof Topo
101. Metwalli, S., Kamel, A., and Saheb, A., Surface Roughness Effect on Laser Speckle Density, SPIE Proceedings, **645** (1986) p. 120.
Coh Expt Thry
102. Mielenz, K., Aberrations of Ellipsoidal Reflectors for Unit Magnification, Appl. Opt., **113**, 12 (1974) .
Abs
103. Munis, R. H., and Finkel, M. W., Goniometric Measurements of Infrared Transmitting Materials, Appl. Opt., **7**, 10 (October 1968) p. 2001.
Aprt Expt Thry Tran
104. Nahm, K., and Wolfe, W., Light Scattering by Polystyrene on a Mirror, SPIE Proceedings, **675** (1986) .
Expt Matl
105. Nicodemus, F., Reflectance Nomenclature and Directional Reflectance and Emissivity, Appl. Opt., **9**, 6 (1970) p. 1474.
Surv Thry
106. Nicodemus, F., Directional Reflectance and Emissivity of an Opaque Surface, Appl. Opt., **4**, 7 (1965) p. 767.
Surv Thry
107. Nicodemus, F., Comment on Current Definitions of Reflectance, J. Opt. Soc. Am., **66**, 3 (1976) p. 283.
Surv Thry
108. Nicodemus, F. E., Richmond, J. C., Hsia, J. J., Ginsberg, I. W., and Limperis, T., Geometrical Considerations and Nomenclature for Reflectance, NBS Monograph 160 (October 1977) .
Calb Desn Stnd Surv Thry
109. Noll R., and Glenn, P., Mirror Surface Autocovariance Functions and Their Associated Visible Scattering, Appl. Opt., **21**, 10 (1982) p. 1824.
Expt Matl Prof Thry Topo
110. Noll, R. J., Effect of Mid- and High-Spatial Frequencies on Optical Performance, Opt. Eng., **18**, 2 (1979) p. 137.
Expt Matl Thry Topo
111. O'Donnell, K., and Mendez, E., Experimental Study of Scattering from Characterized Random Surfaces, J. Opt. Soc. Am., A., **4**, 7 (1987) p. 1194.
Aprt Expt Prof Thry Topo
112. Orazio, F., Jr., Stowell W., and Silva, R., Instrumentation of a Variable Angle Scatterometer (VAS), SPIE Proceedings, **362** (1986) p. 165.
Aprt Desn
113. Pompea, S. M., Bergener, D. W., Shepard, D. F., Russak, S., and Wolfe, W. L., Reflectance Measurements on An Improved Optical Black for Stray Light Rejection from 0.3 to 500 μm, Opt. Eng., **23**, 2 (1984) p. 149.
Aprt Expt Matl Stra
114. Pompea, S. M., Shepard, D. F., and Anderson, S., BRDF Measurements at 6328 Angstroms and 10.6 Micrometers of Optical Black Surfaces for Space Telescopes, SPIE Proceedings, **967** (1988).
Expt Matl
115. Pompea, S. M., Bergener, D. W., Shepard, D. F., and Williams, K., The Effects of Atomic Oxygen on Martin Black and Infrablack, SPIE Proceedings, **511** (1984).
Expt Matl
116. Porteus, J. D., Relation Between the Height Distribution of a Rough Surface and the Reflectance at Normal Incidence, J. Opt. Soc. Am, **53**, 12 (1963) p. 1394.
Thry Topo
117. Richmond, J., and Hsia, J., Bibliography on Scattering by Reflection from Surfaces, J. Res. Natl. Bur. Stand. (U.S.), **80A**, 2 (1976) p. 207.
Surv
118. Rifkin, J., Klicker, K. A., Bjork, D. R., Cheever, D. R., Schiff, T. F., Stover, J. C., Cady, F. M., Wilson, D. J., Chausse, P. D., and Kirchner, K. A., Design Review of a Complete Angle Scatter Instrument, SPIE Proceedings, **967** (1988).
Aprt Desn
119. Rifkin, J., Stover, J. C., McGary, D. E., Kirchner, K. H., and Wilson, D. J., Raster Area Scatter Measurements and Sample Uniformity, SPIE Proceedings, **967** (1988).
Desn Expt
120. Roche, P., and Pelletier, E., Characterization of Optical Surfaces by Measurement of Scattering Distribution, Appl. Opt., **23**, 20 (October 15, 1984) p. 3561.
Aprt Expt Inst Thry Topo
121. Rowe, T. S., Comparison of Scatter from Diamond Turned Optics to Conventionally Formed Optics in the Visible Wavelengths, SPIE Proceedings, **818** (1988).
Expt Matl Topo
122. Scheels, S. F., Scattering from Infrared Transparent Materials, SPIE Proceedings, **107** (1977) p. 48.
Aprt Expt Matl Tran
123. Scherr, L. M., Schmidt, J. H., and Sorensen, K., BRDF of Silicon Carbide and Aluminum Foam Compared to Black Paint at 3.39 Microns, SPIE Proceedings, **1165** (1989).
Expt Matl Stra
124. Schiff, T. F., Stover, J. C., Cheever, D. R., and Bjork, D. R., Maximum and Minimum Limitations Imposed on BSDF Measurements, SPIE Proceedings, **967** (1988).
Desn Inst Thry
125. Shirley, L., and George, N., Diffuser Radiation Patterns Over a Large Dynamic Range. I. Strong Diffusers, Appl. Opt., **27**, 9 (1988) p. 1850.
Coh Thry Topo
126. Shirley, L., and George, N., Wide-Angle Diffuser Transmission Functions and Far-Zone Speckle, J. Opt. Soc. Am., A, **4**, 4 (1987) p. 734.
Coh Thry Tran
127. Silva, R., Orazio, F., Jr., and Stowell, W., Scatter Evaluation of Supersmooth Surfaces, SPIE Proceedings, **362** (1986) p. 71.
Expt Topo
128. Silva, R., Orazio, F., and Sledge, R., A New Instrument for Constant $(\beta - \beta_0)$ Scatter Mapping of Continuous Optical Surfaces of up to 25 Square Inches, SPIE Proceedings, **511** (1984).
Aprt Desn Expt
129. Smith, S., Far-Infrared (FIR) Optical Black Bidirectional Reflectance Distribution Function (BRDF), SPIE Proceedings, **257** (1980).
Aprt Expt Matl Thry
130. Smith, S., and Wolfe, W., Comparison of Measurements by Different Instruments of the Far-Infrared Reflectance of Rough, Optically Black Coatings, SPIE Proceedings, **362** (1986) p. 46.
Desn Expt Inst Matl Stnd Surv
131. Smith, S. M., Far-Infrared Reflectance Spectra of Optical Black Coatings, SPIE Proceedings, **362** (1986) p. 57.
Expt Matl Thry
132. Spyak, P., and Wolfe, W., Cryogenic Scattering Measurements, SPIE Proceedings, **967** (1988).
Aprt Desn Expt

133. Stierwalt, D. L., Infrared Absorption of Optical Blacks, Opt. Eng., **18**, 2 (1979) p. 147.
Expt Matl
134. Stover, J. C., Roughness Characterization of Smooth Machined Surfaces by Light Scattering, Appl. Opt., **14**, 8 (1975) p. 1796.
Expt Prof Thry Topo
135. Stover, J. C., Bernt, M. L., McGary, D. E., and Rifkin, J., An Investigation of Anomalous Scatter From Beryllium Mirrors, Report prepared for Manufacturing Operation Development and Integration Laboratory (MODIL) Engineering Technology Division, Oak Ridge National Laboratory (February 1990).
Expt Matl Topo
136. Stover, J. C., Cady, F. M., and Sklar, E., Measurement of Low Angle Scatter, Opt. Eng., **24**, 3 (May/June 1985) p. 404.
Aprt Desn Inst
137. Stover, J., and Gillespie, C., Design Review of Three Reflectance Scatterometers, SPIE Proceedings, **362** (1983).
Aprt Inst Prof
138. Stover, J., Gillespie, C., Cady, F., Cheever, D., and Klicker, K., Comparison of BRDF Data From Two Scatterometers, SPIE Proceedings, **818** (1987).
Aprt Expt Matl
139. Stover, J. C., and Hourmand, B., Some Deviations Associated with Vector Perturbation Diffraction Theory, SPIE Proceedings, **511** (1984).
Diff Expt Inst Thry Topo
140. Stover, J. C., Hourmand, B., Kahler, J., and Gillespie, C., Comparison of Roughness Measurements by Differential Scatter and TIS, SPIE Proceedings, **362** (1983).
Aprt Expt Prof Surv
141. Stover, J. C., Klicker, K. A., Cheever, D. R. and Cady, F. M., Reduction of Instrument Signature in Near Angle Scatter Measurements, SPIE Proceedings, **749** (1987) p. 46.
Desn Inst
142. Stover, J. C., McGary D. E., and Rifkin, F., Inspection of Large Area and Large Volume Optics by Raster Scanning, SPIE Proceedings, **967** (1988).
Desn Expt Topo
143. Stover, J., Rifkin, J., Cheever, D., Kirchner, K., and Schiff, T., Comparison of Wavelength Scaling Data to Experiment, SPIE Proceedings, **967** (1988).
Expt
144. Stover, J. C., Serati, S. A., and Gillespie, C. H., Calculation of Surface Statistics From Light Scatter, Opt. Eng., **23**, 4 (July/Aug 1984) p. 406.
Pol Topo Thry
145. Stuhlinger, T., Dereniak, E., and Bartell, F., Bidirectional Reflectance Distribution Function of Gold-Plated Sandpaper, Appl. Opt., **20**, 15 (1981) p. 2648.
Aprt Calb Expt Matl Stnd
146. Thompson, C., and Wolfe, W., An Interferometric Approach to Suppression of Scattered Radiant Energy, SPIE Proceedings, **511** (1984).
Aprt Stra Thry
147. Torrance, K., Sparrow, E., and Birkebak, R., Polarization, Directional Distribution, and Off-Specular Peak Phenomena in Light Reflected from Roughened Surfaces, J. Opt. Soc. Am., **56**, 7 (1966) p. 916.
Expt Pol Thry Topo
148. Venable, W., Jr., and Johnson, N., Unified Coordinate System for Retroreflectance Measurements, Appl. Opt., **19**, 8 (1980) p. 1236.
Surv Thry
149. Viehman, W., and Predmore, R. E., Ultraviolet and Visible BRDF Data on Spacecraft Thermal Control and Optical Baffle Materials, SPIE Proceedings, **675** (1986).
Expt Matl Stra
150. Vorburger, T., and Teague, E., Optical Techniques for On-Line Measurement of Surface Topography, Prec. Eng., (1981) p. 61.
Prof Thry Topo
151. Vorburger, T., Teague, E., Scire, F., McLay, M., and Gilsinn, D., Surface Roughness Studies with DALLAS-Detector Array for Laser Light Angular Scattering, J. Res. Natl. Bur. Stand. (U.S.), **89**, 1 (1984) p. 3.
Aprt Expt Inst Prof
152. Wang, H., and Mi, H., Light Scattering Method, Inspection of Diamond Turning Process, Proceedings from In Process Optical Measurements and Industrial Methods at the International Congress on Optical Science and Engineering in the Netherlands (March 1990).
Expt Thry Topo
153. Wang, Y., Scattering From Mirrors Contaminated By Particulates-II: An Extended Model, NASA Tech Brief, **13**, 11 (November 1989).
Thry Topo
154. Wang, Y., and Wolfe, W., Scattering from Microrough Surfaces: Comparison of Theory and Experiment, J. Opt. Soc. Am., **73** (1983) p. 1596.
Expt Thry Topo
155. Wang, Y., Scattering from Mirrors Contaminated by Particulates: A Model, Appl. Opt., **25**, 23 (1986) p. 4222.
Thry Topo
156. Warren, A., Simplified Techniques for Estimating Out-of-Field Radiation, SPIE Proceedings, **257** (1980).
Desn Thry Stra
157. Warren, A. D., Analysis of Out-of-Field Radiation in Reimaging Optical Systems, SPIE Proceedings, **107** (1977) p. 111.
Desn Thry Stra
158. Weidner, V., Hsia, J., and Adams, B., Laboratory Intercomparison Study of Pressed Polytetrafluoroethylene Powder Reflectance Standards, Appl. Opt., **24**, 14 (1985) p. 2225.
Calb Expt Matl Stnd
159. Wein, S., and Wolfe, W., Small-Angle Scatterometer, SPIE Proceedings, **967** (1988).
Abs Aprt Desn Diff Inst
160. Wein, S. J., and Wolfe, W., Gaussian-Apodized Aperatures and Small-Angle Scatter Measurement, Opt. Eng., **28**, 3 (1989) p. 273.
Abs Aprt Desn Diff Inst
161. Williams V., and Lockie, R., Optical Contamination Assessment by Bidirectional Reflectance-Distribution Function (BRDF) Measurement, Opt. Eng., **18**, 2 (1979) p. 152.
Aprt Expt Thry Topo
162. Wojcik, G. L., Vaughan, D. K., and Galbraith, L. E., Calculation of Light Scatter from Structures on Silicon Surfaces, SPIE Proceedings, **774** (March 1987).
Desn Inst Matl Thry Topo
163. Wolfe, W. L., Scattered Thoughts on Baffling Problems, SPIE Proceedings, **256** (1980).
Desn Stra

164. Wolfe, W., Bartell, R. O., and Brooks, L. D., Description and Limitations of an Automated Scatterometer, SPIE Proceedings, **362** (1986).
Inst Stnd
165. Wolfe, W., Hubbs, J., and Bartell, F., Scatter Measurements on LAK9 and SF1 Glasses at 0.915 Micrometers, SPIE Proceedings, **429** (1983).
Expt Matl
166. Wolfe, W., Magee, K., and Wolfe, D., A Portable Scatterometer for Optical Shop Use, SPIE Proceedings, **525** (1985) p. 160.
Aprt Desn Inst
167. Wolfe, W., and Wang, Y., Comparison of Theory and Experiments for Bidirectional Reflectance Distribution Function (BRDF) of Microrough Surfaces, SPIE Proceedings, **362** (1986) p. 40.
Expt Pol Thry Topo
168. Wong, W., Small Angle Bidirectional Reflectance Distribution Function (BRDF) at 10μm, SPIE Proceedings, **430** (1983).
Aprt Desn Expt Inst
169. Young, R. P., Degradation of Low Scatter Mirrors By Particle Contamination, AIAA Paper No.A75-32905 (1975).
Aprt Expt Thry Topo
170. Young, P. J., Noll, R., Andreozzi, L., and Hope, J., Particle Contamination from Martin Optical Black, SPIE Proceedings, **257** (1980).
Desn Expt Matl Stra Thry
171. Young, R. P., Mirror Scatter Measurements Facility Comparison, report no. AEDC-TR-75-68 (1975).
Inst Surv

About the Author: *Clara Asmail is a physicist in the Radiometric Physics Division, National Institute of Standards and Technology.*

Volume 96, Number 2, March–April 1991
Journal of Research of the National Institute of Standards and Technology

[J. Res. Natl. Inst. Stand. Technol. 96, 225 (1991)]

A Limited International Intercomparison of Responsivity Scales at Fiber Optic Wavelengths

Volume 96 Number 2 March–April 1991

R. L. Gallawa

National Institute of Standards and Technology,
Boulder, CO 80303

J. L. Gardner

National Measurement Laboratory,
Lindfield, Australia

D. H. Nettleton

National Physical Laboratory,
Teddington, Middlesex, United Kingdom

K. D. Stock

Physikalisch-Technische Bundesanstalt,
Braunschweig, Germany

T. H. Ward

National Physical Laboratory,
Teddington, Middlesex, United Kingdom

and

Xiaoyu Li

National Institute of Standards and Technology,
Boulder, CO 80303

We report here on a recent limited international intercomparison of responsivity scales at wavelengths of interest to the optical communications community. Participants in the comparison were the national laboratories in the United States, the United Kingdom, Germany, and Australia. The wavelengths tested were 1300 and 1550 nm. Data taken at 850 nm are only briefly discussed. The disagreement between the national laboratories' responsivity scale is comfortably within the uncertainty claimed by each laboratory.

Key words: germanium detectors; international intercomparison; national standards; optical communications; optical detectors; optical power; responsivity.

Accepted: February 28, 1991

1. Introduction

The precise measurement of optical power is of fundamental importance to the proper performance of modern optical communications systems. Power measurements should therefore be traceable to national standards and national responsivity scales should be in reasonable agreement between countries [1]. There have been informal tests of this agreement from time to time but, until now, a formal intercomparison has not been carried out.

We report here on a limited intercomparison that was designed to determine the level of agreement between the responsivity scales of four national standards laboratories whose responsibilities include the calibration of optical power meters for the optical communication community. To that end, we have intercompared the responsivity at 1300 and 1550 nm. The participants were the National Physical Laboratory (NPL), United

Kingdom, the Physikalisch-Technische Bundesanstalt (PTB), Germany, the Commonwealth Scientific and Industrial Research Organization (CSIRO), Australia, and the National Institute of Standards and Technology (NIST), USA. In presenting the results, we will refer to these laboratories anonymously as Laboratories A, B, C, and D.

2. Background

Various limited round robin experiments have been conducted [2] to determine how best to improve metrology service to the optical community and to understand the sources of error in power measurements [3], [4]. As sources of calibration and measurement error become better understood [5] the uncertainty reported by vendors becomes more dependent on the uncertainty of scales of the national standards laboratories. While it was expected that the agreement between these scales is good, the international nature of the optical communications industry has suggested that a substantiation of this agreement was needed.

The Comité International des Poids et Mesures (CIPM) recognized this need and recommended an international intercomparison of responsivity scales at wavelengths of interest to the optical fiber community. The intercomparison that was to be undertaken as a result of that recommendation is quite ambitious, involving a total of fourteen national laboratories. It seemed prudent, therefore, to take preliminary and precautionary steps to minimize the potential for error and to provide guidance for this ambitious undertaking. This preliminary step took the form of a limited international intercomparison, a pilot study between a limited number of participants. The results of that preliminary intercomparison are reported here. The global intercomparison, involving the 14 laboratories, will be reported in due course.

The purpose of the pilot study was to assess the robustness of the transfer standard and identify problem areas and potential sources of error, and thus to guide the more global experiment. In this experiment, each of the participating laboratories calibrated two detectors at the two wavelengths of most interest, in each case using a power level that gives good signal-to-noise ratio and is commensurate with conditions encountered in the field. Additional measurement conditions are given later.

3. Measurement Conditions

Specially selected commercial germanium detectors without coolers and of 5 mm diameter were chosen for the intercomparison. They were selected in advance for linearity, spatial uniformity, and shunt resistance. Launch onto the detector was by open beam with half-angle divergence not exceeding 10 degrees. Incident power of 10 to 50 μW was in a 3 mm diameter spot and centrally positioned to avoid edge effects. The detectors have a window but not an aperture. Measurements were made at 1300 and 1550 nm. A preamplifier was circulated with the diodes.

4. Procedure

All reasonable precautions were taken to protect the detectors from the environment during the course of this test. The detectors were handled with reasonable care and shipped in a special shipping carton. The detectors traveled by commercial air transport.

4.1 National Laboratory Procedures

4.1.1 NPL The instrumentation used at NPL is a spectroradiometer comprised of a high stability tungsten filament lamp imaged with a concave mirror onto the entrance slit of a double grating monochromator. The radiation from the monochromator is imaged via an intermediate field stop onto the center of the germanium photodiodes using another concave mirror. The image is circular with a diameter of 3 ± 0.2 mm and is centered to within 0.2 mm. The incident radiation is within 6 degrees of the normal to the detector surface. The spectral bandwidth is 6 nm. The detector electric current output is recorded using a digital voltmeter with a high quality current-to-voltage converter which has an input offset voltage of less than 2 μV. The detectors are compared directly with NPL standards using a translation slide. The spectroradiometer and data collection are under computer control. Laboratory temperature was 20–21 °C and photocurrent was between 0.5 and 8 μA.

The traceability route at NPL is as follows:

1. Optical power in a laser beam at 800 nm is measured with the NPL cryogenic radiometer, the NPL primary standard for optical power measurements.

2. The data are converted to absolute spectral responsivity of silicon photodiodes at 800 nm using the same laser beam.
3. Conversion is then to absolute spectral responsivity of the germanium photodiodes at 900 nm using dispersed radiation and the NPL relative spectral responsivity scale maintained with a vacuum thermopile. The relative spectral responsivity of this detector has been calibrated from 240 nm to 1 μm from reflectance measurements.
4. Conversion of the data are then to the absolute spectral responsivity of the germanium photodiodes at 1300 and 1550 nm using dispersed radiation and the NPL near infrared relative spectral responsivity scale established with pyroelectric detectors. The relative spectral responsivity of this detector has been calibrated from 800 nm to 1700 nm from reflectance measurements.

4.1.2 PTB

1. The absolute calibration is at $\lambda = 1047$ nm. The primary standard is an electrically calibrated thermal cone detector [6]. The calibration is transferred to a secondary thermopile standard at $\lambda = 1047$ nm (Nd:YLF-laser). Transfer is then to the germanium diodes ($\lambda = 1047$ nm) using a laser spot of 3 mm diameter. The nonlinearity and the temperature coefficient of the thermopile are accounted for [7]. The spot position, size and homogeneity are monitored using a CCD camera which is sensitive at 1047 nm. The power level is from 820 to 880 μW.
2. To determine the calibrations at 1300 and 1550 nm relative to 1047 nm, the relative spectral measurements are performed with a 0.3 m flint-glass prism double monochromator [8]. The secondary standard for the relative measurements is another thermopile whose relative responsivity is constant within $\pm 5 \times 10^{-4}$, as determined by a comparison with a thermal cavity detector [9]. The current levels ranged from 0.4 to 2.7 μA and the spectral bandwidths from 9 to 16 nm. Laboratory temperature was 22 ± 3 °C.

4.1.3 CSIRO The primary standard for radiometric power (and hence responsivity) is determined at 633 nm using inversion layer silicon photodiodes operated under conditions of unity internal quantum yield. The technique is described in reference [10]. An integrating sphere reflectometer [11] is now used. A gold-black bolometer is used [12] as a standard of relative spectral responsivity. For these measurements, a 3 mm diameter InGaAs photodiode is used as a working standard; its absolute responsivity was measured at 633 nm against the inversion layer photodiodes. The InGaAs photodiode was then compared with the bolometer at 633, 1300, and 1550 nm. Finally, the test detectors are compared to the InGaAs detector. A 0.5 m monochromator with prism predisperser is used for wavelength selection with a bandwidth of 8 nm. Supplementary filters are required at 1300 and 1550 nm to reduce the second-order to negligible levels. Dual concave spherical mirrors direct the light from the monochromator onto the test and reference detector in turn, rotating the second mirror symmetrically about the beam from the first. Apertures placed between the mirrors, both filled, are imaged with different magnifications, onto the two detectors being compared. Measurements were made at a laboratory temperature of 21 ± 1 °C. The diodes were temperature controlled at 22 ± 1 °C.

4.1.4 NIST The calibration of optical power at NIST is based on a standard reference instrument called the C-series calorimeter. Details are given in reference [13]. The calorimeter is a national reference standard for measuring absolute energy or power of cw laser sources over a wide range of wavelengths. Infrared laser sources and calibrated beamsplitter measurement systems are used to compare an electrically calibrated pyroelectric radiometer (ECPR) to the C-series calorimeter. The calibrated ECPR is then used as a laboratory standard for the calibration of optical power meters at the wavelengths of interest to the fiber community.

The ECPR was selected as the reference standard because it has a large absorbing surface (about 8 mm diameter), high absorptivity over a wide range of wavelengths and angles of incidence, and it is spectrally quite flat over the wavelength range of interest.

Stabilized laser diode sources provide laser power at the desired wavelengths through a fiber pigtail that traverses a mandrel wrap intended to eliminate cladding modes and induce power stability. The mandrel wrap also produces a beam that has a uniform spatial distribution. The beam that exits from the fiber is collimated by lenses whose focal lengths are such that the collimated beam has nominal diameter of 3 mm. The laser sources, associated fibers, and lenses are configured on a computer controlled positioning table.

The ECPR and the meter to be calibrated (the test meter or detector) are placed in close proximity on the test bench and oriented to allow the beam to be incident, in turn, on the ECPR and then on the test meter, each of which is allowed to reach steady state before a number of readings are taken and averaged. This comparison is repeated

ten to twenty times. A computer is used to control the entire process and to calculate the results. The comparison is facilitated by moving the source, pigtail, mandrel wrap, and lenses, as one unit, thus avoiding the variations that might result when the fiber or associated paraphernalia are moved, even slightly. Measurements were at 22 ± 1 °C.

5. Calibration Results

The results of the calibration test are given in table 1 and in figures 1 and 2, which give the data in graphical form for the two wavelengths. The figures show the normalized data according to laboratory (Laboratories A, B, C, and D, positioned left to right in the figures), and detector number. The data are normalized to the average value for all laboratories in each figure (i.e., at each wavelength). The data are presented anonymously because these calibrations were intended primarily to determine the feasibility of using germanium photodiodes as transfer standards and to circumscribe the problems associated with an international intercomparison.

Table 1. International intercomparison spectral responsivity (A/W)

1300 nm							
Uncertainty (%)	Lab A 1.2	Lab B 0.9	Lab C 0.6	Lab D 0.84	Av.	Max. dev. from av. (%)	Max. diff. (%)
Det. 71468	0.6869	0.6886	0.6876	0.6901	0.6883	0.26	0.46
Det. 71663	0.6898	0.6874	0.6873	0.6891	0.6884	0.20	0.36
1550 nm							
Uncertainty (%)	Lab A 1.2	Lab B 0.9	Lab C 0.6	Lab D 0.97	Av.	Max. dev. from av. (%)	Max. diff. (%)
Det. 71468	0.9055	0.9058	0.9025	0.9048	0.9047	0.24	0.36
Det. 71663	0.9061	0.9094	0.9061	0.9092	0.9077	0.19	0.36

[a] Uncertainty is given at three sigma or 99% confidence level.

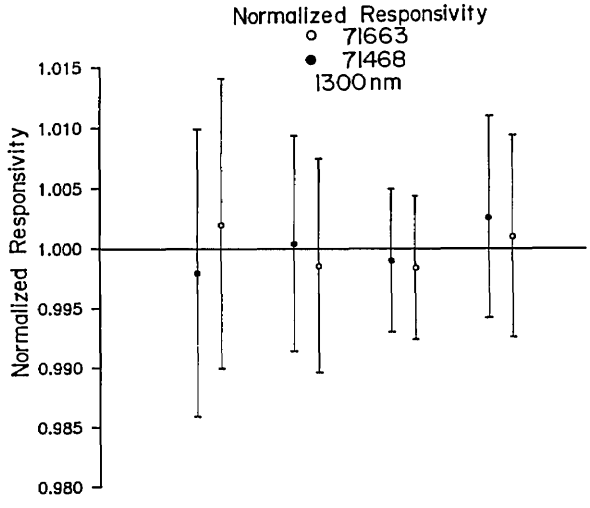

Figure 1. Normalized responsivity at 1300 nm, according to laboratory (Laboratories A, B, C, and D, positioned left to right in the figure) and detector.

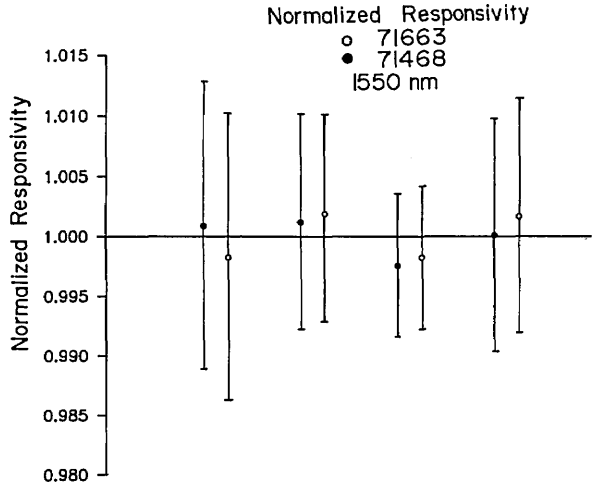

Figure 2. Normalized responsivity at 1550 nm, according to laboratory (Laboratories A, B, C, and D, positioned left to right in the figure) and detector.

Table 1 shows that the maximum difference between any two of the measured responsivities is always less than 0.5%. The maximum deviation by any one laboratory from the average of the calibration factors is 0.36% in three of the four measurements. All data are within the uncertainties of each of the national laboratories.

There is no indication of systematic differences in the data. One laboratory is not consistently lower or consistently higher than the others, thus indicating that random errors are being encountered. In fact, each laboratory has exactly one entry in the column of table 1 that is labeled "maximum deviation from the average." That is, each of the laboratories is furthest from average value exactly once.

It is encouraging to note that the agreement in the calibration is slightly better at 1550 nm (the likely wavelength of future systems) than it is at 1300 nm.

Three of the four laboratories took responsivity data at 850 and 800 nm as well. Since gemanium detectors were used as transfer standards, there was more variability amongst the laboratories than at the long wavelengths, but this can be attributed to higher reflectances, aging [1], and inhomogeneities [14] at the shorter wavelengths. The maximum discrepancy between any two laboratories was 1.2% at 850 nm using detector 71663. We conclude that germanium detectors are probably not suitable at 850 nm; silicon is more appropriate and should be used as transfer standards for the shorter wavelengths. Data for the short wavelengths are not included here because the global international intercomparison will not use the shorter wavelengths. Furthermore, germanium is not the material of choice at the 850 nm window.

Table 1 includes the uncertainty reported by each laboratory. The uncertainty is determined, in each case, according to the rules recommended by BIPM [15]. Each laboratory included Type A uncertainty and Type B uncertainty, which correspond, respectively, to what was once called random and systematic uncertainties (or errors, as they are sometimes called). Type A uncertainties are taken to be normally distributed whereas Type B uncertainties are assumed to be uniformally distributed (sometimes referred to as a rectangular or "top hat" distribution). The width of the Type B uncertainties distribution is difficult to determine in most cases, since they are not based on statistical methods. Each of the participating laboratories determines the width for each contributor according to his own experience.

These and other nuances of the statement of uncertainties have received a lot of attention by the BIPM and the details are beyond the scope of this paper. For our purposes, suffice it to say that each of the participating laboratories reports a total uncertainty, given in the table, that is composed of Type A and Type B uncertainties, combined in quadrature and multiplied by a constant (in our case the constant is 3) to determine a number that is thought of as the uncertainty in the measurement. If the constant is 3, the uncertainty is stated as being at the three sigma (or the 99%) confidence level. It is this uncertainty that is given in table 1.

6. Conclusions

There was good agreement between the responsivity scales of the national laboratories that participated in this intercomparison. Only the wavelengths of interest to the optical fiber community were considered. The data show an encouraging consistency, showing 0.36% maximum difference between any two laboratories. The maximum deviation of any one laboratory from the average was only 0.19 to 0.26%. It seems clear that a transfer standard calibrated by any one of these four laboratories could be used interchangeably with one calibrated by any one of the other three laboratories without loss of accuracy, provided the standards are well characterized and carefully selected.

From these results, we conclude that the germanium detectors that were used here are robust enough to survive the rigors of international comparison when suitable care is taken. The experience gained here will guide us in proceeding to the more global round robin intercomparison that is now underway. In that intercomparison, approximately 14 national laboratories will participate using similar but different detectors.

7. References

[1] Stock, K. D., J. Measurements **8**, 31 (1990).
[2] Gallawa, R. L., and Yang, Shao, Appl. Opt. **25**, 1966 (1986).
[3] Gallawa, R. L., and Li, Xiaoyu, Appl. Opt. **26**, 1170 (1987).
[4] Li, Xiaoyu, and Gallawa, R. L., Fiber Integrated Opt. **7**, 241 (1988).
[5] Fox, N. P., and Nettleton, D. N., eds., New Developments and Applications in Optical Radiometry, Proc. Int. Conf. Optical Radiometry (1989).

[6] Möstl, K., Laser Power and Energy Radiometry, New Developments and Applications in Optical Radiometry, Fox, N. P., and Nettleton, D. N., eds., Proc. Int. Conf. Optical Radiometry, Inst. Phys. Conf. Ser. 92 (1989) pp. 11–18.
[7] Brandt, F., Möstl, K., and Stock, K. D., Temperatur-und Leistungsabhangigkeit der Empfindlichkeit einer Strahlungsthermosaule, PTB-Jahresbericht 1989, pp. 158–159.
[8] Stock, K. D., Calibration of Fiber Optical Power Meters at PTB, New Developments and Applications in Optical Radiometry, Fox, N. P., and Nettleton, D. N., eds., Proc. Int. Conf. Optical Radiometry (1989), Inst. Phys. Conf. Ser. 92, pp. 159–166.
[9] Bischoff, K., Optik **21**, 521 (1964).
[10] Gardner, J. L., and Brown, W. J., Appl. Opt. **26**, 2431 (1987).
[11] Gardner, J. L., A Reflectometer for Absolute Silicon Radiometry, submitted to Applied Optics.
[12] Gardner, J. L., Absolute Spectral Responsivity at 0.2 to 2.5 μm, New Developments and Applications in Optical Radiometry, Fox, N. P., and Nettleton, D. N., eds., Proc. Int. Conf. Optical Radiometry, Inst. Phys. Conf. Ser. 92 (1989) pp. 63–70.
[13] Scott, Thomas R., Optical Power Measurements at the National Institute of Standards and Technology, Proc. Measurements Science Conference, Anaheim, California (1989).
[14] Stock, K. D., Appl. Opt. **27**, 12 (1988).
[15] Comite International des Poids et mesures Proces-Verbaux des Seances, Vol. 49, 70e Session, 1981.

About the authors: *Robert Gallawa is a member of the technical staff of the Electromagnetic Technology Division, National Institute of Standards and Technology, Boulder, Colorado. James Gardner is the leader of the Optics and Radiometry Project in the CSIRO Division of Applied Physics, Lindfield, Australia. David Nettleton is Section Head of the Radiometry and Fibre Optics Section in the Division of Quantum Metrology of the National Physical Laboratory, Teddington, UK. Klaus Stock is a member of the Radiometry Section of the Physikalisch-Technische Bundesanstalt, Braunschweig, Germany. T.H. Ward is a member of the scientific staff of the Radiometry and Fibre Optics Section in the Division of Quantum Metrology of the National Physical Laboratory, Teddington, UK. Xiaoyu Li is a Guest Researcher doing research on optical power metrology in the Electromagnetic Technology Division, National Institute of Standards and Technology, Boulder, Colorado.*

Volume 96, Number 2, March–April 1991
Journal of Research of the National Institute of Standards and Technology

Conference Report

SIXTH BIENNIAL SYMPOSIUM ON OPTICAL FIBER MEASUREMENTS Boulder, CO September 11–12, 1990

Report prepared by

G. W. Day and D. L. Franzen

Electromagnetic Technology Division,
National Institute of Standards and Technology,
Boulder, CO 80303

The development of lightwave communications over the last 2 decades has been particularly dependent on careful metrology to support product specification and standardization. Some estimates have suggested that as much as 20% of the selling price of a fiber is associated with measurements. This perhaps explains the continuing success of the biennial Symposium on Optical Fiber Measurements as an international forum for the discussion of lightwave measurement problems.

The sixth in this series of symposia sponsored by the National Institute of Standards and Technology (NIST) in cooperation with the Institute of Electrical and Electronics Engineers (IEEE) and the Optical Society of America (OSA) was held September 11–12, 1990 at NIST in Boulder. The 2 day meeting drew about 250 attendees; 30 percent came from 16 countries outside of the United States. In addition, several committees of the International Electrotechnical Commission (IEC) and the Telecommunications Industry Association (TIA) concerned with standards for optical fiber measurements took the opportunity to hold meetings on the day before and the 2 days following the Symposium.

Attendees saw and heard a total of 45 papers, 9 invited and 36 contributed, slightly more than half from abroad. As a result of the large number of papers submitted, the committee elected for the first time to schedule a poster session.

The topics of contributed papers at the Symposium have historically been a good measure of current problems facing the industry. At the 1990 meeting there were enough papers on each of three topics to require separate sessions.

One of those was geometric measurements on single mode fiber. Maintaining a high degree of circularity in the cladding of a fiber, an accurate cladding diameter, and good concentricity between the core and cladding are essential in achieving low connector losses. Current measurement agreement for cladding diameter as determined by international comparisons is about 0.4 μm (1 standard deviation). For manufacturers to further reduce geometric tolerances on fiber, primary standards and measurement methods with uncertainties approaching 0.1 μm are needed. To achieve that accuracy it has become necessary to revisit the capabilities of existing methods and to investigate new approaches.

Keith Emig of Corning, Inc. presented data indicating that transverse interferometric techniques, based on Fizeau and Michelson interferometers, could achieve the required 0.1 μm accuracies in cladding diameter measurements. He regards these techniques as suitable for measuring samples to be used for calibrating measurement systems based on microscopic end-viewing. End-viewing is an easy and popular technique, but suffers from difficulty

in edge definition. A team from the National Physical Laboratory (NPL) in England described their experiments with various metal-on-glass artifact standards for the calibration of end-viewing measurement systems and reported that with sufficient care, calibration to the required level can be achieved. However, Matt Young, of NIST, reported systematic errors between 0.1 and 0.2 μm using metal-on-glass standards for calibration. He also reported difficulties in contact micrometer methods related to deformations of the fiber by the measurement device. Scanning confocal microscopy, in which the object is illuminated "point by point by a laser, as the object scans past the focal point of a microscope," is also being investigated at NIST in the hope that it can avoid edge definition problems.

A second area requiring a full session was measurements in integrated optics. Guide attenuation and effective indices remain important problems. Workers at the Centro Studi e Laboratori Telecommunicazioni (CSELT), in Italy, reported that it is possible to measure both of these parameters simultaneously by examining the Fabry-Perot fringes of the cavity formed by the guide while scanning the optical frequency. A paper from the University of Florida described another method of obtaining mode indices, based on a Mach-Zehnder interferometer. Workers at NIST demonstrated that the photothermal deflection technique can be used to obtain loss measurements over an extremely large dynamic range: from less than 0.5 dB/cm in an ordinary waveguide, to 760 dB/cm in a high quality polarizer. There were, in addition, several papers on the characterization of integrated optic modulators.

The third single-topic session was devoted to various techniques of reflectometry. Optical time domain reflectometry has, for 15 years, been essentially the only nondestructive method for obtaining measurements of any parameter in the fiber as a function of length. Now, other versions of reflectometry are being investigated. These include frequency domain techniques and white light interferometric techniques. The motivation for this work is better parameter estimation and, especially, better spatial resolution. In some cases, spatial resolutions on the order of a micrometer are contemplated.

A particularly interesting new approach to obtaining distributed strain measurements, reported in an invited paper from the Nippon Telegraph and Telephone Transmission Systems Laboratories (NTT-Ibaraki) is Brillouin optical time domain reflectometry. This technique uses the fact that the Brillouin shifted lines are stress dependent, and has been successfully used for *in situ* measurements of the strain in undersea cables.

A Technical Digest containing summaries of all of the papers presented at the Symposium is available from the Superintendent of Documents, U.S. Government Printing Office, Washington, DC 20402. Order NIST Special Publication 792, September 1990, stock number SN-003-003-03025-2. The price is $11.00.

Volume 96, Number 2, March–April 1991
Journal of Research of the National Institute of Standards and Technology

News Briefs

General Developments

NSA AND NIST COMPUTER SECURITY PROJECT ANNOUNCED

The National Security Agency's (NSA) National Computer Security Center and NIST will jointly develop new criteria for evaluating the security of computer systems. Expected to last at least 2 years, this effort will lead to a new Federal Information Processing Standard, or FIPS, to specify computer security requirements for federal systems that process unclassified information. NIST and NSA will examine the applicability of the well-established U.S. Department of Defense Trusted Computer System Evaluation Criteria for the systems networking environment and will take into account the migration toward an open systems distributed environment. User and vendor experiences with existing trusted systems will be studied and will influence the direction of the new criteria. Also to be examined are various alternatives for evaluating products and determining their conformance to specified requirements.

COMPUTER SECURITY REVIEW REPORT ISSUED

A new report issued by NIST describes the computer security and privacy plan review effort conducted jointly by NIST and the National Security Agency's National Computer Security Center in response to the Computer Security Act of 1987 (Public Law 100-235). The act requires federal agencies to prepare and submit to NIST and NSA, for review and comment, security plans for all computer systems that contain sensitive information. The report, 1989 Computer Security and Privacy Plans (CSPP) Review Project: A First-Year Federal Response to the Computer Security Act of 1987 (Final Report), also discusses future directions for implementing the act. The goal of the act is to prompt federal agencies to take measures to improve the security and privacy of sensitive information in federal computer systems. Copies of the 189-page report (NISTIR 4409) are available from the National Technical Information Service, Springfield, VA 22161. Order by PB# 91-107540/AS for $23 prepaid.

CRYOGENIC PROPERTIES OF COPPER

NIST and the International Copper Association (ICA) have developed a new wall chart presenting technical data on the properties of copper at cryogenic (super-cold) temperatures. Copper's excellent low-temperature resistivity, thermal conductivity, and reasonable mechanical properties have made it the metal of choice for numerous low-temperature applications in high-energy physics, fusion energy devices, and space experiments. As a result, the initial wall chart, produced in 1979, received wide distribution. The new chart is larger and contains more information, particularly on copper alloys and magnetic properties. Other properties presented include electrical resistivity, thermal conductivity, thermal diffusivity, fatigue, and specific heat/thermal expansion coefficient. Free copies of the chart are available from Fred Fickett, Div. 724.05, NIST, Boulder, CO 80303, or ICA, 708 Third Ave., New York, NY 10017.

PATENT ISSUED FOR "STANDARD CRACK"

NIST researchers have received a patent for a reference standard and a method for manufacturing that standard for use in calibrating eddy current testing systems. These systems are used by the airline industry, among others, to detect cracks and other signs of metal fatigue in aircraft. Until now, a difficulty of the eddy current technique has been the lack of well-defined "flaws" that accurately simulate fatigue cracks. NIST scientists have

produced a reference standard from a block of metal that is deformed by an indentation tool to provide a notch of prescribed dimensions. The reference standard is compressed to close the notch and can then be used to calibrate an eddy current measurement system. For licensing information contact Bruce Mattson, Office of Technology Commercialization, A343 Physics Building, Gaithersburg, MD 20899. For more information on the standard, contact Thomas Capobianco, Division 724.05, NIST, Boulder, CO 80303, 303/497-3141.

NEW TECHNIQUE MEASURES FIBER MATRIX IN COMPOSITES

A NIST researcher has been awarded a patent for a new technique to estimate the strength of the bonding between polymer matrix resin and reinforcements in polymer composites. The mechanical properties of composite materials are strongly influenced by the bonding of resins and fiber reinforcements. This method uses a laser to heat a very small, localized region of the sample. The thermal expansion between the fiber and resin produces an acoustical emission, which can be measured. The stronger the interface, the lower the acoustical signal. Previous methods to evaluate strength require highly trained personnel, are tedious to perform, and require special test specimens or destruction of the composite. The new technique is simple to use and nondestructive. The invention addresses one of the technical barriers to improved polymer composite processing identified by industry at two NIST workshops. For further information, contact Wen-li Wu, B320 Polymer Building, NIST, Gaithersburg, MD 20899, 301/975-6839.

DIAGRAM ADOPTED AS PART OF CODE

A ferrite prediction diagram, developed in a cooperative program between NIST and the Colorado School of Mines, has been adopted as part of the American Society of Mechanical Engineers' Boiler and Pressure Vessel Code, fall 1990 addendum. This is one of the most important safety codes in the world as it controls much of the construction of large and complex vessels for applications such as petroleum and chemical processing. Many severe environments require the use of stainless steel vessels, and the code contains guidance on their construction. The amount of ferrite in these vessels is important because it controls the cracking resistance and corrosion resistance in the welds. The NIST-School of Mines diagram is considered to be a substantial improvement over the 1974 diagram, which it replaces. More information can be obtained from Thomas Siewert, Division 430, NIST, Boulder, CO 80303, 303/497-3523.

NEW METHOD PREDICTS PRODUCT FIRE RISK

Combining traditional methods of analyzing a product's fire risk with powerful new computing tools, a team of researchers from NIST and private industry has developed a new way to measure the life-safety risk of a combustible product. The method can predict whether fire fatalities would increase or decrease if a product's fire performance characteristics were changed. The new technique uses HAZARD I, a computer model developed by NIST, together with statistics on past fires and information from fire tests. Combining all of these methods allows researchers and others to predict not only the probability and outcome of an individual fire, but also to sketch a picture of fires involving a particular product on a national scale. A series of reports describing the method and ways to use it is available from the National Fire Protection Research Foundation, 1 Batterymarch Park, Quincy, MA 02269.

BARRIERS IDENTIFIED FOR USE OF POLYMER COMPOSITES

The most important technical barrier to improved polymer composite processing for the next 5 to 15 years is industry's inability to control resin flow and fiber orientation, said a group of 24 leading composite users, suppliers, and fabricators in a 1990 workshop at NIST. The workshop was the second meeting at NIST in which representatives from industry were asked to target the most critical scientific and technical barriers in composite processing and to identify the serious performance issues that producers must address to meet increasing international competition. The industry group strongly supported conclusions from an earlier meeting, which ranked pressure molding and liquid molding as the two most important polymer processing methods for the future. Process monitoring and the measurement and control of fiber-matrix adhesion also were given high priority. Impact damage and environmental attack were selected as critical performance issues for all industry sectors. For a copy of the report, Second Industry Workshop on Polymer Composite Processing (NISTIR 4461), send a self-addressed mailing label to A209 Polymer Building NIST, Gaithersburg, MD 20899, 301/975-6837.

MANUFACTURING TECHNOLOGY CENTERS HELPING BUSINESS

NIST's Manufacturing Technology Centers program is off to a promising start toward improving the technological competitiveness of small and mid-sized businesses, the NIST Visiting Committee on Advanced Technology said in a report to Commerce Secretary Robert A. Mosbacher. The centers are intended to bridge the gap between sources of manufacturing technology and the companies that need it. The nine-member committee praised the technology-transfer efforts of the New York, Ohio, and South Carolina centers, noting local business support for such efforts as direct project assistance, technical training courses, and demonstrations of hardware and software. The report, Manufacturing Technology Centers Program, looks at the program strategies, operations, and financial support of the three centers. It is available from Dale E. Hall, A527 Administration Building, NIST, Gaithersburg, MD 20899, 301/975-2158.

FIPS REVISIONS OF I/O INTERFACE STANDARDS APPROVED

The Secretary of Commerce has approved revisions to the Federal Information Processing Standards (FIPS) family of input/output (I/O) interface standards to make them non-mandatory. He also has approved discontinuation of the exclusion and verification lists for these standards. Included in the revisions are I/O Channel Interface (60-2), Channel Level Power Control Interface (61-1), Operational Specifications for Magnetic Tape Subsystems (62), Operational Specifications for Variable Block Rotating Mass Storage Subsystems (63-1), Operational Specifications for Fixed Block Rotating Mass Storage Subsystems (97), Storage Module Interfaces (111), Intelligent Peripheral Interface (IPI) (130), and Small Computer System Interface (SCSI) (131). Technical information is available from Shirley Radack, 301/975-2833. Interested parties may obtain copies of the FIPS publications from the National Technical Information Service, U.S. Department of Commerce, Springfield, VA 22161.

CURRENT SUPPLY DESIGNED FOR HIGH-T_C TESTING

Precise and accurate measurements of the DC critical current of high-critical-temperature (high-T_c) superconductors often put stringent demands on the current supply. A simple and inexpensive design for such a current supply has been developed by NIST, based on a common deep-cycle, 12 V, wet-cell battery of the type used in boats and recreational vehicles. A description of the circuit, including diagram, was published in Measurement Science and Technology, Vol. 1 (1990). Reprints are available from Steven Bray, Mail Code 814.05, NIST, Boulder, CO 80303, 303/497-5631.

NEW LIBRARY FOR ALTERNATIVE REFRIGERANT ANALYSIS

Intensive efforts are under way to evaluate environmentally acceptable alternatives to fully halogenated chlorofluorocarbon fluids for air conditioning and refrigeration equipment and aerosol propellants. The evaluation process requires a complete set of thermophysical property data so relevant engineering properties can be mathematically modeled or correlated. Also, thermophysical measurements often are carried out at elevated temperatures and pressures, where decomposition and chemical reactions may occur. Thus there is a need for reliable identification of contaminants and reaction products in these fluids. Spectroscopic Library for Alternative Refrigerant Analysis (NIST SP 794) assembles a collection of infrared and mass spectra on chloro-fluoro-bromo ethanes and ethylenes to assist in this identification. The library also includes other physical properties where possible. Available from the Superintendent of Documents, U.S. Government Printing Office, Washington, DC 20402. Order by stock no. 003-003-03036-8 for $12 prepaid.

U.S. SPEED SKIERS TO GAIN COMPETITIVE EDGE

Six computer software and hardware companies and a sports helmet firm have combined forces at NIST to give America's top speed skiers and small machine shop operators a competitive edge. The companies used NIST's Shop of the 90s facility to design an aerodynamic helmet for athletes that flash down slopes at speeds up to 224 km/h (139 mph). The facility is used to research and demonstrate how small machine shops can rapidly produce sophisticated, competitive products with commercially available technology. The firms donated material and personnel to the helmet project under a cooperative research agreement with NIST.

ACC, NIST TO IMPROVE POLYMER COMPOSITES PROCESSING

NIST and the Automotive Composites Consortium (ACC) have agreed to improve the processing of structural polymer composite materials. The ACC partnership is aimed at developing the technology industry needs for processing reliable, cost-effective structural polymer composite materials. The cooperative project will focus on composites made by resin transfer molding and structural reaction injection molding. NIST researchers will develop and use computer models for both processing methods to simulate the fabrication of a complex demonstration part made by the ACC using the latest processing and performance technologies. The NIST computer models are designed to predict flow patterns and pressures during processing. For information, contact Donald L. Hunston, A209 Polymer Building, NIST, Gaithersburg, MD 20899, 301/975-6837.

NEW SUPERCONDUCTOR POLYMER COMPOSITES DEVELOPED

Composites made by mixing powdered ceramic superconducting materials with a polymer may be a practical way to fabricate a new generation of materials with the magnetic levitation properties of superconductors, even though they do not conduct electric current, say NIST researchers. The superconductor-polymer composites were developed by NIST scientists, who have received a patent for their innovation. Laboratory work has demonstrated that a ceramic superconductor placed in a matrix of polyvinylidene fluoride displays the magnetic levitation properties of a superconductor. When a magnetic field is applied to the composite at superconducting temperatures, an electric current flows around the surface of each particle, creating a counter-magnetic field that gives the composite its levitating properties. The polymer acts as a binder and shields the particles from exposure to moisture and other chemically active substances that can destroy superconductivity. For information, contact Aime S. DeReggi, B320 Polymer Building, NIST, Gaithersburg, MD 20899, 301/975-6725.

MATERIALS FOR MAGNETIC FUSION ENERGY

NIST has published the 13th report in a series on research to determine the properties of materials that may be used in cryogenic structures for superconducting magnets for fusion energy power plants. Materials Studies for Magnetic Fusion Energy Applications at Low Temperatures—XIII (NISTIR 3944) presents research results for 1989-90 under four headings: structural alloys, welding, test standards, and technology transfer. The research is managed by NIST, sponsored by the Department of Energy's Office of Fusion Energy, and conducted at NIST and other laboratories through cooperative agreements. Available from the National Technical Information Service, Springfield, VA 22161. Order by PB# 91-107086/AS for $39 prepaid.

USE OF IRDS STANDARD IN CALS PUBLICATION ISSUED

Use of the IRDS Standard in CALS (NISTIR 89-4169), a paper authored by NIST scientists, shows how the Information Resource Dictionary System (IRDS) can fulfill critical design and operational requirements for CALS (Computer-aided Acquisition and Logistic Support program of the Department of Defense) Phase II. The authors provide examples as well as a schedule to illustrate that the IRDS and other data management standards will be available when needed to meet the immediate requirements of CALS. An architecture is presented to show additional standards required to achieve longer-range goals of distributed database, and development tasks are recommended. Available from the National Technical Information Service, Springfield, VA 22161. Order by PB# 90-130295 for $23 prepaid.

SYMPOSIUM DIGEST PUBLISHED

The digest of papers presented at the sixth biennial Symposium on Optical Fiber Measurements (Boulder, CO, Sept. 11-12, 1990) is now available. Topics discussed in the 45 papers include optical time domain reflectometry, fiber geometry measurements, integrated optics, laboratory intercomparisons, refractive index measurements, fiber amplifiers and sensors, and connector measurements. Available from the Superintendent of Documents, U.S. Government Printing Office, Washington, DC 20402. Order by stock no. 003-003-03025-2 for $11 prepaid.

CONSORTIUM TO DEVELOP NEW WAY TO FIND PAINT FLAWS

A government-industry consortium is being explored by NIST to develop an automated non-destructive process to detect and evaluate defects in paints on metal products such as automobiles. An automated detection system using computer image processing and robotics along with techniques to

"map" the surface of a product would be faster and more precise than current detection systems, says a materials research engineer at NIST. Research on coating defects, robotics, and non-destructive evaluation techniques currently being conducted by researchers at NIST could provide the basis for the new inspection technique. NIST is sponsoring a workshop at its Gaithersburg, MD, headquarters on May 9 and 10 to get industry reaction to the consortium idea. Organizations interested in attending the workshop should contact Jonathan Martin at 301/975-6717 or Theodore Vorburger at 301/975-3493.

MICROSTRIP PATCH ANTENNA DEVELOPED

Calibration laboratories will be interested in a new development from NIST that makes certain antenna measurements and electro-magnetic interference/compatibility tests more convenient. NIST researchers have developed a small (20 cm^2) microstrip patch antenna that can be used as a standard transmitting and receiving antenna at frequencies below 500 MHz in an anechoic chamber. Up to now, well-characterized pyramidal horns and open-ended waveguides have been used, but at frequencies below 500 MHz, these instruments become very large and impractical. NIST researchers proved that the resonant frequency, driving point impedence, antenna radiation pattern, and radiated field strength of the microstrip patch antenna could be calculated theoretically from its geometry and are accurate to within 3 percent. Paper No. 2-91 describes the antenna in detail and is available from Jo Emery, Division 104, NIST, Boulder, CO 80303, 303/497-3237.

OBTAINING LIQUID NEON AT LOWER COSTS

NIST researchers have designed and constructed a small-scale plant capable of recycling liquid neon for about $20 per liter, $150 per liter less than liquid neon can be obtained commercially. The plant was designed to capture, purify, and refrigerate neon boiling off from calorimetry experiments in the low-temperature measurement of the thermal conductivity of insulating materials. The recycling plant consists of a purification section, a heat exchanger, liquid neon and liquid hydrogen storage dewars, and a fully automated control system. After purification, neon is liquefied in the heat exchanger by liquid hydrogen flowing countercurrently through stainless steel cooling coils. Hydrogen flow is automatically adjusted to keep the neon at its normal saturation temperature of 27 K. The liquefied neon is stored in a dewar directly below the heat exchanger; a low-temperature refrigerator provides cooling during extended storage or low-flow applications. Paper No. 4-91 describes the plant in more detail and is availabale from Jo Emery, Division 104, NIST, Boulder, CO 80303, 303/497-3237.

USDA ADOPTS HANDBOOKS 133 AND 44

The Food Safety and Inspection Service of the U.S. Department of Agriculture (USDA) has adopted new rules that amend federal meat and poultry products inspection regulations. The rules incorporate NIST Handbook 133, Checking the Net Contents of Prepackaged Goods, and NIST Handbook 44, Specifications, Tolerances, and Other Technical Requirements for Weighing and Measuring Devices, by reference. The rules are intended to establish federal uniformity with state and local net weight requirements. As of May 1991, meat and poultry plants will be required to follow sampling and testing procedures as provided in Handbook 133 to demonstrate compliance with federal regulations. Operators of federally inspected establishments will be required to have their scales tested at least annually and to maintain accuracy as defined by applicable tolerances in Handbook 44. State weights and measures officials, USDA officials, and state-licensed or registered scale repair firms will be able to inspect and test scales within the plant. Approximately 12,000 meat and poultry plants in the United States and abroad operate under USDA inspection criteria, and there are approximately 7,000 USDA meat and poultry inspectors.

CHARPY IMPACT TESTS NEAR ABSOLUTE ZERO

Research initiated by NIST with the cooperation of the Massachusetts Institute of Technology and the Japan Atomic Energy Research Institute has led to the re-evaluation of Charpy impact test procedures at extreme cryogenic temperatures. The conventional approach does not work for tests at liquid helium temperature (4 K) because excessive adiabatic heating occurs during impact. Thermocouple measurements reveal that austenitic steel specimens actually heat to about 130 K upon impact. NIST has presented the findings to the appropriate American Society for Testing and Materials (ASTM) subcommittee. Based on this research the existing standard, ASTM Methods for Notched Bar Impact Testing of Metallic Materials (E 23-88), is currently being revised to limit its applicability to test temperatures of 77 K and higher.

JOHNS HOPKINS TO PARTICIPATE IN NEUTRON RESEARCH AND INSTRUMENTATION

The Department of Physics and Astronomy at The Johns Hopkins University has agreed to participate with NIST in the development of a cold neutron scattering spectrometer for materials research at the NIST Cold Neutron Research Facility (CNRF), as part of a new cooperative research effort in the area of condensed matter physics and magnetic material characterization, including heavy fermion systems.

The instrument is the new cold neutron triple-axis spectrometer to be installed at guide NG-5 of the CNRF. The instrument will have state-of-the-art capabilities in resolution and data collection efficiency, and will have several unique features which will place it among the most versatile in the world. Initial measurements will be devoted to fundamental studies of the microscopic properties of new magnetic materials.

CRITERIA FOR ACCREDITING FASTENER TESTING LABORATORIES

Public Law 101-592, the Fastener Quality Act, was signed into law by President Bush on November 16, 1990. The law requires that critical fasteners (e.g., high-strength aircraft bolts and nuts) conform to the specifications to which they are represented, and provides for the accreditation of testing laboratories to certify this conformance. NIST, through its National Voluntary Laboratory Accreditation Program (NVLAP), is charged with developing and administering the accreditation program for fastener testing laboratories. NIST has accepted the responsibility for establishing the technical criteria which NVLAP will use to assess candidate laboratories. NIST scientists will review the current specifications for the many categories of fasteners that are covered by the act and will draft procedures for evaluating the capabilities of laboratories for carrying out the standard mechanical test methods cited in these specifications. They will also design proficiency test programs to serve as part of the evaluation procedures. Regulations governing the accreditation of fastener testing laboratories are expected to be announced in May 1991.

NEW PUBLICATION PRESENTS GUIDELINES FOR REALIZING THE NEW INTERNATIONAL TEMPERATURE SCALE

NIST Technical Note 1265, Guidelines for Realizing the International Temperature Scale of 1990 (ITS-90), is available to those who need information on the ITS-90. This technical note describes the ITS-90, the techniques by which the ITS-90 can be realized, and the uncertainties associated with its realization. It instructs the user on how to convert calibrations of thermometers recently calibrated on the International Practical Temperature Scale of 1968 (IPTS-68) to approximate calibrations on the ITS-90. The publication gives details of the changes of the ITS-90 from the IPTS-68 and describes the extension of the ITS-90 from the lower limit of the IPTS-68 at 13.81 K to the newer lower limit of 0.65 K.

Several improvements to the new scale enhance the reproducibility of measurements: replacing the use of the thermocouple as a standard instrument of the scale; extending the range of the precision platinum resistance thermometer upward to the silver freezing-point temperature (961.78 °C); and extending the radiation thermometry range downward to the silver freezing-point temperature. Several new defining fixed points have been adopted for the ITS-90 in order to reduce the non-uniqueness of the scale, i.e., the disagreement of temperature values indicated by different standard thermometers at temperatures intermediate to the defining fixed points of the scale. Alternative definitions were incorporated for certain ranges of the ITS-90 so that the use of the scale would be more convenient.

PRECISION LASER SPECTROSCOPY REVEALS UNEXPECTED WAVELENGTH SHIFT

In a recent experiment, NIST physicists were able to measure a particular atomic transition wavelength in helium 10 times more accurately than ever before. This improvement allowed a precision test of subtle quantum effects and yielded surprising results that may have a fundamental impact on our understanding of quantum interactions.

The NIST team used an atomic beam and laser interferometers to measure the singlet 2S-3P helium wavelength with an error of less than 10 millionths of an atomic diameter. At this level of accuracy, ordinary quantum mechanics breaks down and one needs a quantum field theory known as "quantum electrodynamics," or "QED" in order to explain the observations.

The new NIST measurement is of interest because it was carried out on an atomic system that is both simple enough to be treated rigorously from first principles and complicated enough to show how the effect of QED on one electron can be influenced by the presence of another nearby electron. Such effects are only beginning to be treated accurately at the quantum level. Previous high-precision

measurements on triplet transitions in helium had shown good agreement with theoretical prediction, leading researchers to believe that a firm theoretical understanding was at hand. For the singlet transition studied by the NIST team, however, the Pauli exclusion principle allows the two electrons to spend more time close together, thereby amplifying the effects of interest. When the NIST measurement was complete, it showed that the wavelength for the helium single transition was significantly different from the theoretical prediction. This finding has been recently confirmed in an independent laboratory at Yale University. Further theoretical work will be needed to explain these results.

YALE MEDICAL SCHOOL AND NIST PIONEER NEW METHOD OF MAPPING RADIATION DOSE FROM GAMMA-RAY BRACHYTHERAPY SOURCES

Researchers in the Department of Therapeutic Radiology at Yale and NIST have developed a novel technique of mapping radiation doses to tissue in two and three dimensions using radiochromic films. In a paper submitted to Medical Physics, these investigators describe the method of mapping the dose from a gamma-ray brachytherapy source of the radionuclide iridium-192. ("Brachy-" is from the Greek meaning "near.") Because of its ideal low-energy spectrum, iridium-192 has largely replaced radium for intracavitary therapy. Improved methods are needed for routine quality assurance for this therapy.

Radiochromic films, which have a reproducible color response to ionizing radiation, are superior to photographic silver halide films in that they have a fairly flat energy response and can be calibrated at NIST for absorbed dose measurement. By scanning the autoradiographs with a laser-scanning densitometer, a high-resolution digital image is obtained. The digital information (optical density) is then converted to absorbed dose using the film calibration. The medical uses of these films present the most demanding accuracy requirement yet encountered. The goal of this work will be to determine absorbed dose to tissue to within ± 5 percent.

INTEROPERABILITY TESTS PUBLISHED

Two new NIST publications describe the interoperability test suites of Open Systems Interconnection (OSI) applications covered by Federal Information Processing Standard (FIPS) 146, Government OSI Profile (GOSIP), Version 1. NISTIR 4435, FTAM Interoperability Test, contains the file transfer, access, and management (FTAM) interoperability test suite, while NISTIR 4452, Message Handling Systems Interoperability Tests, presents the X.400 interoperability test suite. GOSIP, Version 1, became effective in federal procurements on August 15, 1990. Future versions of the GOSIP standard will incorporate additional OSI applications.

NIST ESTABLISHES GRAPHICS IN GOVERNMENT (GIG) USERS GROUP

NIST recently hosted the first meeting of the newly formed GIG Users Group. Sponsored by the graphics software group of the Information Systems Engineering Division, the GIG Users Group provides a forum for federal government colleagues to exchange ideas on computer graphics and to increase NIST's understanding of the specific and unique graphics technology needs of federal agencies. The GIG Users Group attracted about 40 participants. The next meeting is planned for the spring or summer of 1991.

ASTM ACCEPTS NIST-DEVELOPED INTERLABORATORY TEST SOFTWARE

Interlaboratory results are the ultimate test of a standard method of analysis. Unfortunately, the measurement data and associated statistics required to evaluate an interlaboratory test tend to be lengthy. NIST researchers have developed a PC-computer program to perform this task, which should lead to greater uniformity in the evaluation and reporting of different standard methods.

Working with the ASTM Subcommittee E-11.04 on Development and Evaluation of Test Methods, NIST researchers designed a computer package which consists of the PC software, a 40-page user's manual, and a reprint of the parent ASTM standard E691-87 for evaluating interlaboratory results. The package is available for purchase from ASTM at a nominal cost. The software package has been well received during the 6 months that it has been available. It is hoped that most ASTM standard test methods will eventually use the E691-87 standard and computer program for development and documentation.

For each material of the interlaboratory study, the program examines both the individual data points for within- and between-laboratory variabilities, and derives summary within- and between-laboratory components of precision for the complete study. Computer graphics play a prominent role in the evaluation and reporting of the data. The program produces both tables and graphs for screen or hard copy.

INADVERTENT TEMPERATURE RISES MAY CAUSE POOR MAGNET PERFORMANCE

NIST scientists have carried out experiments that point to enhanced flux creep driven by inadvertent increases in operating temperature of large superconducting magnets as a cause of an heretofore unexplained degradation in the magnetic fields produced by the magnets. Flux creep is a thermally driven phenomenon that results in a slow decay in the magnetization of superconducting cables and a concomitant decrease in their magnetic field. Since 1988, researchers have been confronted with a significant difference between magnetization decay rates measured in specimens of superconductor cable and decay rates observed in accelerator magnets made from the same kind of cable. The difference can be important. For example, in the superconducting super collider (SSC) the reduced performance could cause loss of the accelerator's proton beam.

The NIST work examines magnetization decay rates in specimen SSC cables and attributes the enhanced decay rate, not accounted for by simple thermal activation, to a supercritical state in which shielding currents temporarily flow at a density greater than the new critical current density at the higher temperature.

CAPABILITY ESTABLISHED FOR QUANTIZED HALL RESISTOR FABRICATION AT NIST

NIST has completed a fabrication and test laboratory for quantized Hall resistors and has fabricated structures that appear to be of standards quality. These Hall-bar structures were etched from gallium arsenide wafers having gallium arsenide-aluminum gallium arsenide heterostructures grown by the NIST molecular beam epitaxy system. Thus NIST now has the capability to produce its own high-quality QHR structures, both to implement the national QHR resistance standard and for research. Although NIST counterpart laboratories and others are taking steps to address the supply issue, heretofore there have been relatively few high-quality QHR specimens available. The new laboratory provides a cleanliness level of class 10 and incorporates a mask aligner, an alloying station for etching and forming low-resistance indium or tin-alloyed contacts, and a probe station and related equipment for evaluating specimens as they are made.

AC IMPEDANCE METHOD MEASURES HIGH-RESISTIVITY SILICON INGOTS AND SLICES

NIST researchers have developed an ac impedance method for measuring the bulk resistivity of high-resistivity silicon ingots and slices. The method is non-destructive in character and only requires that easily removable contacts, such as may be formed from silver paint, be applied to the end faces of the specimen crystal.

In the method, the impedance of the paint-crystal-paint capacitive sandwich is measured as a function of frequency from 100 Hz to 40 MHz. The resistivity is then calculated from the frequency at which the negative peak occurs in a plot of the imaginary component of the impedance and from the absolute values of the real and imaginary components of the impedance at that frequency. In addition to its intended application for measuring bulk resistivity, the method is useful for determining the quality of applied contacts and the effect of surface treatments which result in a significant depletion layer.

The NIST scientists have made extensive measurements of the resistivity of high-resistivity silicon in order to compare the results of the new method with existing dc resistance, van der Pauw, and four-probe methods. The typical agreement between these methods and the new method is within 5 percent for slices and ingot sections greater than 1 mm in length and resistivity above 5000 ohm-cm. The method is applicable to any high-resistivity material, and measurements have also been made on semi-insulating gallium arsenide.

COLLABORATIVE STUDIES USING SYNCHROTRON RADIATION UNLOCK ATOMIC BOND SECRETS

NIST scientists have shown for the first time how the atoms in a GeSi crystal arrange themselves when GeSi is grown epitaxially on the slightly smaller crystal lattice of silicon. The scientists are using synchrotron radiation to study the bonds between atoms in strained GeSi layers and between antimony and silicon atoms on silicon surfaces; the synchrotron radiation is generated at the National Synchrotron Light Source at Brookhaven National Laboratory by electrons traveling around an evacuated ring at relativistic velocities.

Understanding the physical arrangement of atoms of GeSi on silicon is prerequisite to exploiting the potential use of heterojunctions of this type

for high-speed bipolar transistors. The advantage of using GeSi alloys is that the energy bandgap can be tuned by controlling the concentration of germanium in the alloy; at the same time, devices using this technology can be fabricated using the highly developed silicon processing technology available. The studies of antimony on silicon illuminate the complementary role of surface geometry and electronic structure in determining how metal-semiconductor contacts are formed.

The measurement techniques employed in these studies include extended x-ray absorption fine structure, x-ray diffraction, and photoemission. A collaborating research team at Stanford Electronics Laboratory prepares test specimens, and a team at the University of Washington makes the x-ray diffraction measurements.

COLLABORATION WITH INDUSTRY ON THE DEVELOPMENT OF A FASTENER WORKSTATION

NIST has begun a joint R&D project with the Portsmouth Naval Shipyard and industry to develop an automated fastener workstation in the Automated Manufacturing Research Facility (AMRF). Precision fasteners used in such critical applications as aircraft and submarines must conform to federal and industrial standards for accuracy and performance. Besides meeting such criteria, the fasteners must meet material traceability requirements as well. The joint R&D effort involves the development of the technology, methodology, and computer control systems necessary for the production of highly accurate fasteners.

These fasteners are now manufactured from both k-monel and nickel copper material, which are excellent for their resistance to corrosion. However, this type of fastener is expensive to produce because the high tolerance specified for the parts requires frequent inspection at different stages of the production process. An automated fastener workstation would offer a significant reduction in production time as well as cost. These objectives can be achieved by using a multispindle, multiturret turning/machining center for the increase in production efficiency, while integrating statistical process control and in-process inspection into the overall manufacturing process, thus enhancing quality control.

NIST DEVELOPS TEST PROCEDURE FOR BUILDING GASEOUS FILTER EQUIPMENT

NIST staff have developed a laboratory test procedure for determining the performance of air filtration equipment that removes gaseous air contaminants from building air streams. The application of filtration equipment in commercial buildings has dramatically increased because of the concern for indoor air quality. Industry standards exist for testing and rating particulate filters but to date have not been developed for gaseous filtration. The laboratory procedure developed at NIST calls for the filtration equipment to be challenged with the contaminant at a fixed concentration and measurements made of the penetration of the contaminant over time. Results from testing with different contaminants and at different challenge concentrations are used for estimating the useful life of the air cleaning filter media. The procedure will be offered for adoption as a standard test method to the American Society of Heating, Refrigerating, and Air-Conditioning Engineers.

U.S. STANDARDS ORGANIZATIONS

NIST has issued Standards Activities of Organizations in the United States (NIST SP 806). This publication identifies and describes activities of more than 750 U.S. public- and private-sector organizations that develop, publish, and revise standards; participate in this process; or identify standards and make them available through information centers or distribution channels. NIST SP 806, a revision of NBS SP 681 (dated August 1984), provides expanded and updated coverage of activities regarding both mandatory and voluntary U.S. standards. It is designed to serve as a reference for all who need and use standards or who wish to identify organizations involved in standardization.

PATENT ISSUED ON NIST TRANSCONDUCTANCE AMPLIFIER DESIGN

The Commissioner of Patents and Trademarks has issued United States Patent 4,965,529 to a NIST scientist for his invention of a high current, very wide band transconductance amplifier. This patent has 14 claims, covering the inventions implemented in the design of the NIST model 20A-2 transconductance amplifier. The instrument can source currents up to 35 A rms at 100 kHz, with short-term instability of less than plus or minus 25 parts per million. This combination of output current and frequency exceeds by a factor of 15 the previous best for transconductance amplifiers. An important application of the amplifier is in calibrations of current-related quantities. For example, its extended current and frequency capabilities permit the calibration of current shunts, ammeters, and thermal current converters to be carried out over signifi-

cantly broader ranges of these quantities than heretofore. Several companies have expressed strong interest in the NIST amplifier; and one is finalizing a licensing agreement that will permit it to market a commercial product based on the NIST design. Details of the NIST instrument were published in the Institute of Electrical and Electronics Engineers Transactions on Instrumentation and Measurement, Vol. 39, No 1.

CONSORTIUM ON AUTOMATED ANALYTICAL LABORATORY SYSTEMS (CAALS) HOLDS WORKSHOP

A CAALS workshop on communication standards for remotely controlling analytical chemistry instrumentation was recently held at NIST. A presentation was made by a representative from one of the CAALS members on the work of the Consortium on Standard Commands for Programmable Instruments (SCPI), which is comprised of the major vendors in the U.S. electronic test and measurement community. The SCPI consortium has developed an open standard for test equipment commands primarily utilizing IEEE-488 control interfaces. The development of similar commands for analytical chemistry instrumentation is a primary goal of the CAALS Modularity Project.

The workshop was devoted mainly to developing both generic and specific models for analytical chemical instruments. Such models are built principally by defining instrument command sets and specifying how the instruments respond to those commands. A major effort was expended in culling generic commands (those that are mandatory on every standardized instrument) from common commands (those which may be active on most equipment) and specific commands (those which are pertinent to only certain instruments or techniques). Once the instrument models are constructed, future workshops will address the full content of messages needed for remote control of analytical chemistry instrumentation.

MOVING SHEET FACILITY FOR ON-LINE QUALITY MEASUREMENTS

NIST has collaborated with industry to develop a test bed to demonstrate the feasibility of measuring the formability of rapidly moving steel sheets. The test bed is a device which propels sheet specimens along a track at controlled, repeatable velocities that can be increased up to about 150 m/min. The device consists of: a pneumatic cylinder/piston arrangement, which is connected by cable to a sled; precision-machined track, which guides the sled; a bridge, which spans across the track and provides locations for mounting ultrasonic transducers; and a braking system, which stops the sled at the end of the track. The ultrasonic formability sensor developed by NIST will be mounted on the bridge. This system gives NIST a unique measurement facility of use to the producers and fabricators of sheet steel.

SOLDER: MATERIALS FOR ELECTRONIC PACKAGING

Although solder has been used since the time of the Egyptians, it was not until this century that its bulk properties were understood. More recently, it has been recognized that failure of solder joints often occurs at the joint interface where brittle intermetallics can form. This can lead to malfunction in critical applications such as aircraft and automobile electronic components, which are increasingly computerized. In an ongoing program NIST researchers have obtained detailed information on the mechanisms responsible for interface fracture, which may lead to the development of a realistic interface fracture model. One of three modes occurs, depending on the thicknesses of the intermetallic layers. For very thin layers (less than about 1 μm), classic ductile fracture occurs in the bulk solder. For thicker layers, fracture can occur on either side of the intermetallic zone. On the Cu_3Sn/Cu side, a brittle fracture occurs. On the Cu_6Sn_5/solder side, only the Pb phase of the solder adheres leading to the formation of ductile fracture ligaments of Pb. By using metallurgical techniques to limit the formation of brittle intermetallics at the interface, the researchers expect to double the strength of solder joints and bring an ancient material up to date.

INSTRUMENTS OPERATIONAL IN CNRF

Two experimental stations are now operational in NIST's Cold Neutron Research Facility (CNRF): the 8 m small-angle neutron scattering spectrometer (SANS) and the cold neutron depth-profiling instrument (CNDP).

The SANS, which had been installed on the cold source in the reactor hall, began operation in the guide hall on Oct. 18, 1990. Measured neutron intensity on the sample in the new configuration is greater than 85 percent of the intensity in the reactor hall with a signal-to-noise ratio more than four times better. A variety of experiments have already been conducted, including studies of colloidal mixtures under shear, temperature dependence of bonded phase structure in microporous silica, polymer conformations in blends, ultrathin films and solutions, microemulsions, and high T_c superconductors.

The CNDP instrument, which measures near-surface elemental composition vs. depth in semiconductors and thin films, is installed on the cold source in the reactor hall, and began operation Nov. 1, 1990. The new 61 cm diameter stainless steel depth-profiling chamber is capable of operating at UHV pressures and incorporates many design features that significantly enhance the capabilities that currently exist at the thermal depth-profiling instrument in the reactor hall. A measurement sensitivity approximately 20 times that of the present thermal neutron facility for the same efficiency particle detectors has been determined.

A profile of O^{17} in a Co-Ni-Oxide film was among the first obtained with the new facility, reported to be the first nondestructive determination of near-surface oxygen made anywhere in the world for this type of sample.

COLLABORATION WITH AUTOMOTIVE CONSORTIUM ON POLYMER COMPOSITES PROCESSING

NIST scientists will participate with the Automotive Composites Consortium in a program to improve structural polymer composites made by the resin transfer molding (RTM) process. The cooperative program aims at developing the technology that industry needs for processing reliable, cost-effective polymer composite materials. Under the cooperative agreement, NIST will develop and apply computer models that predict polymer flows and pressures in RTM processing to a complex structural automotive part. The part will be fabricated by the consortium. The RTM process involves injection of resin into a mold that already contains the fiber reinforcements. The technical challenge is to achieve the optimal resin flow so that the mold is completely filled in the shortest time while avoiding excess pressures or voids. The computer modeling will assist in the design of molds and processing conditions that optimize mold filling.

EFFECT OF FILAMENT GEOMETRY ON CVD DIAMOND FILMS

In order to increase the deposition area in hot filament chemical vapor deposition (CVD) of diamond films, one must understand how the filament geometry will affect the growth rate and morphology of the films. To address this question NIST researchers deposited a series of diamond films. Three factors were varied: the number of helical turns in a filament—5, 10, or 15; the number of filaments present—1 or 2; and the methane fraction in the methane/hydrogen feed gas mixture—0.25 percent, 0.5 percent, 0.75 percent, or 1 percent. While the general trend was an increase in growth rate with increasing methane fraction, increasing the number of filament turns and using dual filaments rather than single filaments sometimes resulted in lower than expected growth rates. In the case of 15 turn filaments, the growth rates were lower in the dual filament system than in the single filament system. In addition, the films that grew at lower than expected growth rates showed morphologies indicative of single filament depositions conducted at lower methane concentrations. These results suggest that there is a depletion of the carbon necessary for diamond film growth associated with using multiple filaments. It is possible that more carbon is necessary to maintain the carburization of the filament leaving less for diamond film growth. Further investigations are under way to confirm this explanation. The coverage with dual filaments, however, was double the coverage with single filaments.

NIST UPDATES FIRE HAZARD ASSESSMENT METHODOLOGY

A NIST scientist has produced a revised version (18.5) of FAST, a model of fire growth and smoke transport. This is in preparation for the first update of HAZARD I, scheduled for release early this summer. HAZARD I is a prototype methodology to assess the relative contributions of potentially flammable commercial products (e.g., furniture, beds) to deaths in building fires. The method helps the user define first the fire problem of concern and then the specific fire factors contributing to the problem. These factors include not only the flammable item(s), but also such important features as the building design, the people inside, the weather, and the time of day. NIST-developed (PC compatible) software then calculates the outcome of each of the fires, enabling the user to analyze the impact of making changes in the product or other features of the fire. The new modifications allow for more complex fuels, enable hydrogen chloride to deposit on walls, and include the effects of forced ventilation on smoke transport, as well as a number of improvements in the software. The documentation has been released as NIST Technical Note 1282.

NOVEL TURBULENCE DIAGNOSTIC DEVELOPED

A NIST scientist and university colleagues have produced a new technique for characterizing turbulent flow fields. This combines two unique instruments. The first is a line camera, which uses Rayleigh light scattering to measure species concentration. The second, located just downstream, is an array of fine hot wire anemometers. The combination enables simultaneous, real-time multipoint measurements of concentration and velocity along a line. Using this technique, the researchers have demonstrated the importance of organized large-scale motions to the turbulent mixing process. Their work also shows that there are periods during which the fluid near the perimeter of a turbulent jet is simply convected by an external coflow. A report of this work will appear in Applications of Laser Techniques in Fluid Mechanics (Springer-Verlag, 1991).

CH RADICALS MEASURED IN DIFFUSION FLAMES

NIST scientists have made the first quantitative measurements of CH· profiles in a diffusion flame. CH· is a highly reactive species that contributes to soot formation in flames and nitrogen oxide generation in engines. Using laser-induced fluorescence, the scientists showed that the peak CH· concentration appears on the fuel-rich side of the flame. Combined with profiles of other species in the same flame measured by the NIST researchers it was possible to derive a profile for the important triplet methylene radical $^3CH_2$. The work will be published in Combustion Science and Technology. This growing, systematic documentation of a methane/air diffusion flame has become a prime resource for modelers of flame chemistry worldwide.

NIST SCIENTISTS MEASURE EFFECT OF OXYGEN CONCENTRATION ON CO AND SOOT IN FLAMES

NIST scientists have collaborated with scientists from the Japanese Building Research Institute and the U.S. National Forest Products Association to measure vitiation effects on pollution formation. For the study, they used the cone calorimeter, a bench-scale device for measuring radiation-enhanced combustion. The fuels included were methane, propane, an ABS plastic, a polyethylene, and Douglas fir. The team found that decreasing the oxygen concentration in the combustion air from 21 to 14 percent increased the CO yields by at least a factor of 2. The soot yields from the solid materials were insensitive to the vitiation, changing less than 30 percent. Results for air vitiated alternatively by carbon dioxide and by nitrogen suggest that the CO yield is controlled mainly by the flame temperature. These results will be presented at the 3rd International Symposium on Fire Safety Science in July 1991 and will be published in the proceedings.

ASCE COMPLETES STANDARD ON STRUCTURAL CONDITION ASSESSMENT OF BUILDINGS

A standards committee of the American Society of Civil Engineers (ASCE) chaired by a NIST scientist has prepared ASCE 11-90 "Standard Guideline for Structural Condition Assessment of Existing Buildings." The standard provides information on the structural condition assessment procedure; assessment techniques for concrete, metals, masonry, and wood components; guidance on evaluation techniques; and the format of the assessment report. The need for the standard was identified by NIST researchers studying building rehabilitation who required a standardized procedure for assessing the condition of a building being considered for adaptive re-use, rehabilitation, or improvement.

COOPERATIVE RESEARCH AND DEVELOPMENT AGREEMENT FOR A BASIC TEST SUITE ESTABLISHED

NIST has established a Cooperative Research and Development Agreement with a private company to develop a test suite for evaluating BASIC implementations for conformance to FIPS 68-2, BASIC. This is the first time such an Agreement has been used to obtain the needed tests for federal programming language standards. Under the Agreement, NIST will provide administrative and scientific direction and the company will provide the research associate(s) for building and maintaining the test suite. The company will own and market the resulting BASIC test suite, while NIST will receive a nonexclusive, transferrable, irrevocable, paid-up license to use the test suite for any government purpose.

FEDERAL INFORMATION PROCESSING STANDARDS (FIPS) ACTIVITIES

On Dec. 27, 1990, the Secretary of Commerce approved FIPS 159, "Detail Specification for 62.5 μm Core Diameter/125 μm Cladding Diameter Class Ia Multimode, Graded-Index Optical Waveguide Fibers" (former Federal Standard 1070). FIPS 159 adopts for federal agency use the voluntary industry American National Standard/ EIA/TIA-492AAA33A-1989, dated February 1989.

To be effective July 1, 1991, FIPS 159 specifies standard characteristics for multimode optical fiber waveguides for use in electro-optical communications systems applications. The standard will facilitate interoperability among telecommunication facilities and systems of the federal government.

Also approved by Secretary Mosbacher, effective Dec. 18, 1990, were revisions to eight I/O interface FIPS to make them non-mandatory for federal agencies and to discontinue the exclusion and verification lists that NIST had been maintaining for these standards. The I/O interface standards family includes: FIPS 60-2, "I/O Channel Interface"; FIPS 61-1, "Channel Level Power Control Interface"; FIPS 62, "Operational Specifications for Magnetic Tape Subsystems"; FIPS 63-1, "Operational Specifications for Variable Block Rotating Mass Storage Subsystems"; FIPS 97, "Operational Specifications for Fixed Block Rotating Mass Storage Subsystems"; FIPS 111, "Storage Module Interfaces"; FIPS 130, "Intelligent Peripheral Interface"; and "FIPS 131, Small Computer System Interface (SCSI)."

COMPUTER SECURITY GUIDANCE PUBLISHED

Two new publications report on computer security studies and guidelines developed by federal and private-sector organizations. U.S. Department of Commerce Methodology for Certifying Sensitive Computer Applications (NISTIR 4451) describes a standard certification methodology employed to ensure that sensitive applications meet applicable federal policies, regulations, and standards. SRI International's Improving the Security of Your UNIX System (NISTIR 4453) provides various suggestions for improving the security of systems operating under the UNIX operating system. NIST published these documents as part of a continuing effort to assist federal agencies in improving the security of their information systems and to make useful information available to the federal community.

Standard Reference Materials

MEASURING FOOD COMPONENTS AIM OF NEW MATERIALS

Scientists studying health and disease aspects of food consumption depend on accurate measurements of nutrients and contaminants in food samples. But to ensure the reliability of instruments and analytical methods, they need standards—ideally standards containing a variety of foods representative of an average American diet. A standard reference material (SRM) now available from NIST offers a typical diet combined into a bottled freeze-dried powder. Foods such as eggs, pizza, hamburgers, and beer are all included. The material contains certified concentrations of 14 chemical elements as well as ash, fat, dietary fiber, cholesterol, and caloric content. Chemists can analyze these materials as they would any food sample and compare their analysis to the numbers provided. The U.S. Department of Agriculture prepared the SRMs for NIST from foods obtained through the Total Diet Study, an on-going Food and Drug Administration program that monitors foods from various U.S. regions for pesticides, toxins, and nutrients. Total Diet (SRM 1548) costs $251 for two 6.5 g bottles and is available from the Standard Reference Materials Program, Rm. 204 Building 202, NIST, Gaithersburg, MD 20899, 301/975-6776.

PRODUCTION OF ULTRA-PURE ^{242}Pu SOURCES AND SRMS FOR ENVIRONMENTAL AND PERSONNEL MONITORING

Ultra-pure reference samples and radiation sources of ^{242}Pu are now available from NIST.

For several years there has been a severe shortage of ^{242}Pu of sufficient radiochemical purity to be used as a tracer in radiochemical analysis, including environmental and personnel monitoring. Such environmental and personnel monitoring is required by law for nuclear installations to remain in operation. The Lawrence Livermore National Laboratory of the U.S. Department of Energy (DOE) has now mass separated and chemically purified several milligrams of ultra-pure ^{242}Pu.

In the past, the Isotope Sales Division at the Oak Ridge National Laboratory of the DOE handled the sale and distribution of such materials. Due to a change in DOE policy, this is no longer possible. NIST will now handle the sale and distribution of this ultra-pure ^{242}Pu in the form of special sources at higher activity levels and in the form of a standard reference material, SRM 4334D, at a lower activity level (approximately 25 Bq g^{-1}).

The ^{242}Pu special sources and SRM 4334D are now available from NIST. U.S. government facilities have first priority for the special sources. It appears that enough material is available to provide standards for several years.